ABSTRACT BOOK

SMRA 2021

33rd Annual International Conference

Communication & Collaboration through Connection

All oral and poster abstracts are included in this Abstract Book.
Find the abstracts you are interested in by searching **Abstract ID**.

Abstract ID: 1

A Cardiac MRI investigation of the correlation between left ventricular function and myocardial strain in hypertrophic cardiomyopathic patients

Shaotong Feng, Yifan Wang, Li Zhu*

Department of Radiology, General Hospital of Ningxia Medical University, Ningxia, China

Purpose: To further study the changes in early cardiac function and myocardial strain in patients with non-obstructive HCM.

Methods: A cohort of 39 patients with non-obstructive HCM (as the experimental group) were enrolled in this study. The patient's baseline characteristics, ventricular function and strain parameters were measured by the CVI42 software, the control group used the relevant parameters in the published literature. In addition, according to the AHA 17-segment left ventricular model standard, the 624 myocardial segments of HCM group were divided into hypertrophic segments and non-hypertrophic segments. LV global and segmental myocardial strains were analyzed by tissue tracking by two experienced observers.

Results: In the early stage of HCM patients (LVEF > 50%), their left ventricular mass was significantly higher than that of the control group, their left ventricular end-systolic volume was lower than that of the control group, and the global strain of their left ventricle was significantly lower than control group. In HCM group, left ventricular LVESV was positively correlated with GCS and GLS (GCS:r=0.66, GLS:r=0.45). PRS, pCS, pRSSR, pCSSR, pRDSR, pCDSR and LPD in hypertrophic myocardial segments were significantly lower than those in non-hypertrophic myocardial segments.

Conclusion: For non-obstructive HCM patients with cardiac function retention, myocardial deformation can more accurately reflect impaired myocardial function. The global or segmental left ventricular deformation was significantly decreased. There was also a significant correlation between LV strain or strain rate parameters with Left ventricular function.

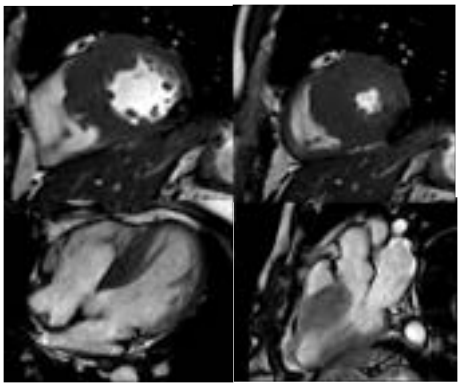

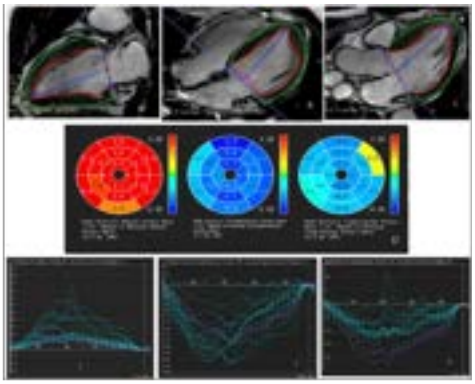

Figure 1. Patient, male, 49 years old; due to his chest tightness, his ECG showed abnormal ST-T segment. He was later confirmed to have non-obstructive HCM after CMR examination. Patients with no other related history of hypertension.

Figure 2. A,B,C. Left ventricular long axis two-chamber heart, four-chamber heart and inflow and outflow channel plane; D. Radial, longitudinal and circumferential strain bull's eye diagram; E,F,G Trend of myocardial segment RS.LS.CS in a cardiac cycle.

Acknowledgment: This study was supported by First-class discipline construction founded project of Ningxia medical university and the school of clinical medicine (NXYLXK2017A05).

Abstract ID: 2

Joint Learning of Group-wise Diffeomorphic Registration and Reconstruction of Cardiac Cine MRI

Haikun Qi
School of Biomedical Engineering, ShanghaiTech University, Shanghai, China

Introduction

Cardiac cine MRI is usually acquired under multiple breath-holds to minimize respiratory motion, and its acceleration is clinically warranted to shorten breath-hold duration. Accelerated dynamic MRI reconstruction has been extensively investigated by exploiting temporal correlation (1-3). Among these methods, some have incorporated cardiac motion into reconstruction to increase the sparsity and improve reconstruction (3), which however, require time-consuming alternative optimization of registration and reconstruction. Deep learning-based dynamic reconstruction methods have reduced the reconstruction time significantly (4), but most of them neglect motion in the reconstruction. In this study, we aim to propose an unrolled deep learning framework with each iteration consisting of a group-wise diffeomorphic registration network (GW-Net) to predict the implicit template and backward and forward motion fields, and a dealiasing network to perform motion-augmented reconstruction.

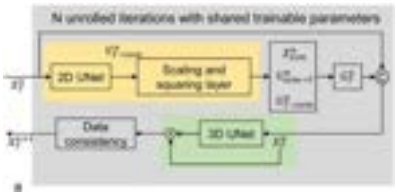

Fig. 1 The architecture of the proposed GW-Recon-Net with one of the unrolled iterations shown. The yellow block shows the GW-Net and green block is the dealiasing network.

Methods

Group-wise Diffeomorphic Registration: As shown in **Fig. 1**, the GW-Net based on a 2D UNet (5), takes input of the dynamic images (X_T^n, T is the number of dynamics) of the previous iteration which are stacked as different channels and outputs the implicit template (X_{tem}^n) and the invertible non-rigid motion fields ($U_{T\to tem}^n$ and $U_{tem\to T}^n$) between the template and the dynamic images. The template is the average of the warped dynamic images. Then, by warping the template image with the forward motion fields ($U_{tem\to T}^n$), a new dynamic sequence (G_T^n) is generated. The information of the full dynamics is fused into the template and then the generated cine images, which can be used to enhance the reconstruction performance.

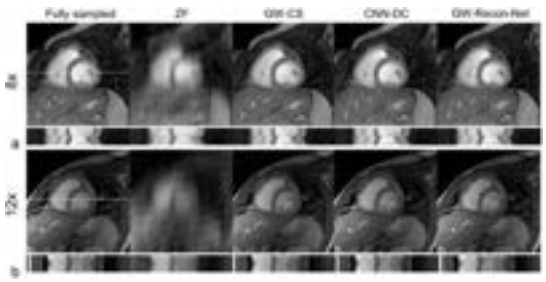

Fig. 2 Example cardiac cine images for 8x (a) and 12x (b) accelerations, including the fully sampled and ZF images, and the reconstructions obtained with GW-CS, CNN-DC and the proposed GW-Recon-Net. The temporal profile with the slice location shown by the white line in the fully sampled image is provided for each dynamic sequence.

Motion-augmented Reconstruction: Following the GW-Net is the reconstruction network. To take advantage of the motion-augmented cine images, G_T^n and X_T^n are stacked along the channel dimension to be inputted to the dealiasing network (green block in Fig. 1), which is a residual 3D UNet. After the data consistency (DC) layer (4), the dynamic images (X_T^{n+1}) are outputted as inputs of the next iteration. The whole framework is termed as GW-Recon-Net.

Network Training: For GW-Net, the registration loss (L_{reg}^n) is designed to measure the dissimilarity between the warped dynamic images and the template, and the dissimilarity between the motion-augmented and original dynamic images, as well as the smoothness of the velocity field ($V_{T\to tem}^n$): $L_{reg}^n = \sum_{t=1}^{T}\left\|X_{tem}^{gt} - warp(X_t^{gt}, U_{t\to tem}^n)\right\|_2^2 + \left\|X_t^{gt} - G_t^{gt}\right\|_2^2 + \alpha TV(V_{t\to tem}^n)$, where X^{gt} means fully sampled ground truth image, TV means total variation, and α is the weight of the smoothness term. The mean-squared-error between the reconstruction output and the ground truth is used to calculate the reconstruction loss (L_{recon}^n). The final loss for end-to-end training is the weighted combination of L_{reg}^n and L_{recon}^n: $L_{total} = \sum_{n=1}^{N} w_n(L_{recon}^n + \lambda L_{reg}^n)$, where λ controlling the contribution of the registration loss and $w_n = exp(n-N)$ is the weight of each unrolled iteration.

Dataset and Evaluation: The publicly available breath-hold cardiac cine datasets from (6) are used, which includes data of 33 subjects. Each subject's cardiac cine consists of 20 frames and 8-13 short-axis slices. We have used 25 subjects for training with data augmentation, 2 subjects for validation and 6 subjects for testing. The data was retrospectively undersampled for 8x and 12x acceleration factors with the sampling density conforming to a zero-mean Gaussian distribution. To evaluate the performance of GW-Recon-Net, it was compared with GW-CS (3) which performed GW registration during reconstruction, and the deep unrolled reconstruction framework (CNN-DC) without considering motion (4). The network was trained for 100 epochs with initial learning rate of 1e-4, which was decreased by a half every 20 epochs.

Table 1. PSNR, SSIM and reconstruction time (per slice) for the three reconstruction methods.

Method	PSNR (8x)	SSIM (8x)	PSNR (12x)	SSIM (12x)	Time (s)
GW-CS	33.43 ± 3.51	0.93 ± 0.02	30.51 ± 3.96	0.89 ± 0.03	266.5
CNN-DC	35.86 ± 3.74	0.95 ± 0.02	32.36 ± 3.77	0.91 ± 0.03	0.4
GW-Recon-Net	36.60 ± 4.09	0.96 ± 0.02	34.10 ± 3.90	0.94 ± 0.02	0.8

Results

For each cardiac cine dataset, 7-8 central slices were selected, resulting in a total of 46 slices to evaluate the reconstruction performance. **Fig. 2** shows the example reconstructions for 8x and 12x accelerations with GW-CS, CNN-DC and the proposed GW-Recon-Net, as well as the corresponding fully sampled and zero-filling reconstructed (ZF) images. The PSNR, SSIM and reconstruction time of the 3 reconstruction methods are summarized in **Table 1**. The proposed method had the highest PSNR and SSIM among the tested methods. The improved performance of GW-Recon-Net compared with CNN-DC highlighted the benefit of incorporating group-wise registration into deep learning reconstruction.

Discussion & Conclusions

We have proposed a method of joint learning of group-wise diffeomorphic registration and reconstruction of cardiac cine MRI. The GW-Net predicted both backward and forward motion between all dynamics and an implicit template. The backward motion was used to fuse the information of all dynamics into the template and the forward motion was used to transform the template to a dynamic sequence to augment the reconstruction. Furthermore, the group-wise registration exploits information of the full dynamics more efficiently than the pairwise registration. With aggressive acceleration, such as 12x, the cardiac cine MRI could be completed in a single breath-hold. Therefore, the highly accelerated cardiac cine acquisition together with GW-Recon-Net reconstruction may greatly simplify the cardiac cine MRI.

References: 1. Lingala, S.G, et al. IEEE TMI 2011. 2. Otazo, R, et al. MRM 2015. 3. Royuela-del-Val, J, et al. MRM 2016. 4. Schlemper, J, et al. IEEE TMI 2018. 5. Ronneberger, O, et al. MICCAI 2015. 6. Andreopoulos, A, et al. MIA 2008.

Abstract ID: 3

Modeling cerebral small vessels from 7T TOF-MRA images using neural network and random forest

Zhixin Li[1,2,3] , Yue Wu[1,2,3] , Dongbiao Sun[1,2,3] , Jing An[4] , Qingle Kong[5] , Rong Xue[1,2,3], Yan Zhuo[1,2,3] , and Zihao Zhang[1,2,3]
[1]State Key Laboratory of Brain and Cognitive Science, Institute of Biophysics, Chinese Academy of Sciences, Beijing, China, [2]The Innovation Center of Excellence on Brain Science, Chinese Academy of Sciences, Beijing, China, [3]University of Chinese Academy of Sciences, Beijing, China, [4]Siemens Shenzhen Magnetic Resonance Ltd., Shenzhen, China, MR Collaboration, Siemens Healthcare Ltd, Beijing, China

Introduction: Time-of-flight MR angiography (TOF-MRA) at 7T has been proved to be a valuable technique for noninvasive imaging of cerebral small vessels, especially for lenticulostriate artery (LSA)[1] . However, the accurate segmentation and modeling of cerebral small vessels remains challenging, due to the limited signal-to-noise ratio and artifact of the images[2]. To solve the problem, we used convolutional neural network (CNN) and random forest algorithm for the automated 3D modeling and analysis of LSA vasculature.

Methods: Six healthy controls and three patients with cerebral small vessel disease (CSVD) were included in our study. The images (N=7) were acquired on a 7T research MRI system (Siemens, Erlangen, Germany). The parameters of TOF-MRA were: resolution = 0.23×0.23×0.34mm^3, matrix = 576×768×144, TR = 15ms, TE = 3.57ms, FA = 20°. ***Segmentation stage:*** Large arteries (such as middle cerebral arteries) were segmented by intensity thresholding. The CNN was trained for the segmentation of small vessels. There were 1600 positive patches and 12000 negative patches were used as the training unit for high robustness. After the vessel mask was generated, mean filter was appllied to remove the scattered false positive voxels and smooth the edge of the vessels. The cluster algorithm was used to overcome the interruption of blood vessels and remove tubular motion artifact. ***Tracing stage***: The most appropriate cylinder vertex position was determined by the random forest method, which had the following features: ***a***. Blood vessel points number in the cylinder. ***b***. Distance bias to the center of the blood vessel. ***c***. The vector deflection angle. ***d***. Blood vessel points number around the target point. ***e***. The eigenvalues of Hessian matrix.

Results: The vascular models of a healthy volunteer and a patient were represented in Fig. 1, along with their MIP images. The mean radius (mm) of different levels of vascular branches were listed in Tab. 1. Compared with U-NET, our method achieved higher dice similarity coefficient (DSC) and lower Hausdorff Distance. Especially, in the area of small vessels, our method achieved higher performance on segmentation, as shown in Tab. 2.

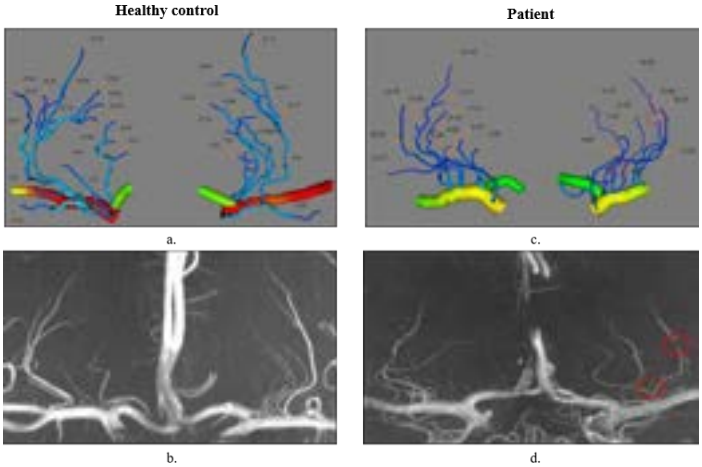

Figure 1. 3D vasculature and MIP image of a healthy volunteer and a CSVD patient, with the radius(mm) of vascular branches noted on the images. The red circles indicate the discontinuous flow signal, which was well characterized in the vascular model.

Table 1. The mean radius (mm) of different levels of vascular branches

	L1	L2	L3
S01	0.214	0.160	0.124
S02	0.204	0.170	0.117
S03	0.214	0.185	N/A
S04	0.207	0.160	N/A
S05	0.216	0.189	N/A
S06	0.191	0.142	0.112
P01	0.143	0.079	N/A
P02	0.140	0.086	N/A
P03	0.153	0.099	0.085

Table 2. Comparison between our approach and U-NET for segmenting small vessels.

	Method	DSC(%)	Hausdorff Distance (mm)
subject1	U-NET	85.299	7.246
	Our Method	90.696	6.397
subject2	U-NET	84.946	11.095
	Our Method	92.755	9.375
subject3	U-NET	87.372	6.387
	Our Method	92.358	4.043
subject4	U-NET	82.879	8.307
	Our Method	92.44	4.886
subject5	U-NET	85.206	6.061
	Our Method	93.289	5.011
AVE	U-NET	85.140±1.426	7.819±1.813
	Our Method	**92.308±0.870**	**5.942±1.875**

Discussion: In this work, we realized the automated modeling of LSA from 7T TOF-MRA images by CNN and random forest method. Quantitative features of LSA was successfully obtained.

Acknowledgement: This work was supported by the National Natural Science Foundation of China (82001804, 8191101305), the Natural Science Foundation of Beijing Municipality (7191003), the National Key Research and Development of China (2017YFC1307904), and the Strategic Priority Research Program of Chinese Academy of Science (XDB32010300).

References: [1] Cho ZH et al., *Stroke*. 2008;39(5):1604-6. [2] Liao W et al., *IEEE T Image Process*. 2015;25(1):400-13. [3] Livne M et al. *Front Neurosci*. 2019 Feb 28;13:97.

Abstract ID: 4

Simultaneous T1, T2 and T2* Mapping of the Carotid Plaque Using Combined Single- and Multi-echo Three dimensional Golden Angle Radial Acquisition

Yajie Wang[1], Yishi Wang[2], Haikun Qi[3], Rui Guo[4], Huiyu Qiao[1], Dongyue Si[1], Huijun Chen[1]

1. Center for Biomedical Imaging Research, Department of Biomedical Engineering, School of Medicine, Tsinghua University, Beijing, China. 2. Philips Healthcare, Beijing, China. 3. School of Biomedical Engineering, ShanghaiTech University, Shanghai, China. 4. Department of Medicine, Beth Israel Deaconess Medical Center and Harvard Medical School, Boston, Massachusetts, USA

Purpose: Quantitative techniques of the carotid atherosclerotic plaque have been drawing more and more attention[1-6], while most techniques depended on multiple scans which may lead to misregistration and increase the total scan time. Recently, GOAL-SNAP[5] and SIMPLE[7] sequences have been proposed to quantify T1 mapping or T1, T2 mapping of the carotid plaque in a single scan. In addition, the iron deposition, which can be quantified by T2* mapping, has also been reported to play an important role in plaque progression[4,8]. Thus, we aim to develop a new sequence to quantify carotid plaque T1, T2 and T2* mapping simultaneously in a single scan.

Methods: Sequence design: The proposed sequence extended the SIMPLE[7] sequence (Figure 1). 3D golden angle radial single-echoes were acquired continuously after T2IR preparation and used for T1 and T2 quantification. Only after the IR without T2 preparation, golden angle radial multi-echoes were obtained after the single-echo acquisition and used for T2* quantification. Radial spokes acquired at the same inversion time (TI), same T2 preparation and same echo time (TE) were designed to satisfy the golden angle strategy[9]. Image Reconstruction and T1, T2, T2* fitting: Sliding window reconstruction with a temporal width of 25 (262.5 ms/frame) was applied for the single-echo module, while for the multi-echo module, k-space data acquired from the same TE were combined. Low-rank and sparsity constraint (LRS) reconstruction[10] was performed to improve the image quality. T1 and T2 were estimated from the single-echo module by combining two extra 3D radial SPGR images using Bloch equation[7]. A mono-exponential decay curve was fitted to estimate T2* from the multi-echo module. Phantom and in-vivo study: All scans were performed on a 3.0 T MR scanner (Ingenia CX, Philips Healthcare). Phantom study was performed on 10 tubes with different T1, T2 and T2* values. The T1, T2 and T2* quantification using the proposed sequence were compared with traditional 2D IR-SE, ME-SE and ME-GRE sequences using Pearson correlation. After institutional review board approval and obtaining informed consent, 1 patient with carotid plaque were scanned by the proposed sequence and the conventional multi-contrast sequences, including TOF, black-blood T1-TSE and T2-TSE[11], SNAP[12], ME-GRE[4] using a dedicated 8-channel carotid coil.

Results: The mean T1, T2 and T2* values within each tube estimated by the proposed sequence showed good agreements with IR-SE (Figure 2, r = 0.996, p<0.001), ME-SE (r = 0.993, p<0.001) and ME-GRE (r = 0.989, p<0.001). In patient, the lipid rich necrotic core region showed comparable or slighted higher T1, obviously lower T2 and obviously lower T2* values estimated from the proposed sequence, which were coincide with the signal intensity characteristic on multi-contrast images (Figure 3).

Discussion and Conclusion: Quantitative T1, T2 and T2* measurements were achieved within one scan using the proposed sequence which combined the single- and multi-echo 3D golden angle radial acquisition. In the future, more in-vivo studies on patients with carotid atherosclerotic plaque are needed.

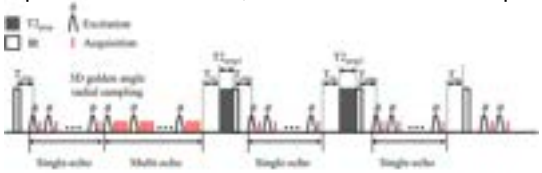

Figure 1. Sequence diagram.

Table 1. Scan parameters of the proposed sequence.

FOV	Voxel size	$T2_{prep}$	Flip angle	T_{gap}	T_{rf}	Scan duration
100 mm³	0.8 mm iso	[0 25 50] ms	8°	9 ms	13 ms	10 min
Single-echo module			**Multi-echo module**			
TR	**TE**	**Number of pulses**	**TR**	**First TE**	**Delta TE**	**Number of echoes**	**Number of pulses**
10.5 ms	4.3 ms	175	33 ms	4.3 ms	5.6 ms	5	95

References: [1] Coolen BF, et al. ISMRM. 2013. [2] Chai JT, et al. JACC. 2017. [3] Coolen BF, et al. MRM. 2016. [4] Raman SV, et al. JACC. 2008. [5] Qi H, et al. Radiology. 2018. [6] G. Mihai SG, et al. ISMRM. 2011. [7] Qi H, et al. MRM. 2018. [8] Winner MW, et al. J. Vasc. Surg. 2015. [9] Chan RW, et al. MRM. 2009. [10] Qi H, et al. ISMRM. 2018. [11] Cai J-M, et al. Circulation. 2002. [12] Wang J, et al. MRM. 2013.

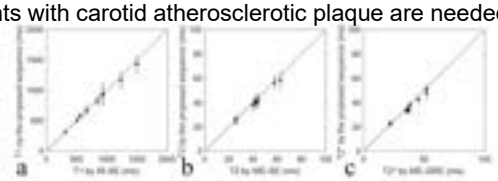

Figure 2. Quantitative comparison of the T1 (a), T2 (b) and T2* (c) mapping results of the phantom.

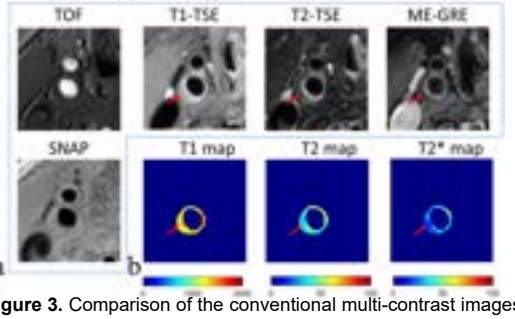

Figure 3. Comparison of the conventional multi-contrast images (a) and T1, T2, T2* maps estimated by the proposed sequence in patients with a lipid rich necrotic core (red arrow) .

Abstract ID: 5

QISS-MRA and other flow related MRA-sequences at 3T in comparison to CE-MRA/-MRI for evaluation and quantification of the thoracic aorta after therapy – preliminary results

Tamara Sand, cand med[1,2], Ingeborg Keeling, MD[2], Martin Hasenhüttl[1], Manuela Aschauer, MD[1]

[1]Department of neuro-, vascular and interventional radiology, Medical University of Graz, Austria
[2]Department of cardiac surgery, Medical University of Graz, Austria

Purpose:
After treatment of aortic diseases, a CE-MRA/-MRI is one of the diagnostic standard methods for further treatment decisions. The purpose of the study was to compare the image quality and diagnostic accuracy of the flow related MRA-sequences: QISS-, 4D-flow- and SPACE-MRA, with the standard CE-MRA/-MRI.

Methods:
Seven patients (57±19 years, 2 men) were selected for the prospective study. In March 2021, these patients were examined with 4D-flow-, SPACE- and sometimes QISS-MRA in addition to the CE-MRA/-MRI (mostly with SIEMENS® PRISMA fit E11, CE-MRA/-MRI with the use of Gd-based cyclic contrast agent). The thoracic aorta, sometimes the abdominal aorta too and the supra-aortic, mesenteric and renal vessels were evaluated. One reader took the 4D-flow-measurements with the software cvi42. Three readers evaluated the image quality and the diagnostic accuracy of the QISS-, 4D-flow- and SPACE-MRA.

Results:
None of these flow related MRA-sequences can replace the CE-MRA-/-MRI-sequences in total. If there is no contraindication of contrast agent application, the CE-MRA is the first sequence that should be aquired. If a short-term follow-up is requested, the flow-related MRA-sequences add useful information.
The QISS-sequence had unacceptable inhomogeneities and signal loss, also the acquisition time took too long in our patient cohort.
4D-flow offers information about the aortic segments with higher wall shear stress, compared with other aortic segments. This may be useful information in addition to the diameter to decide for another invasive diagnosis or treatment. No complications occurred in the first three months of follow-up.

Discussion:
Although we had no possibility to use the free-breathing fast low-angle shot quiescent-interval slice-selective MR-Angiography[4], the SPACE-MRA[6] sequence seems to be the first sequence to choose, if the use of contrast agent is not recommended.
The 4D-flow sequence[3,5] can be used to get additional hemodynamic information without invasive diagnostic tools, i.e. catheter pressure measurement.

Chronic aortic dissection, male, 68 years:

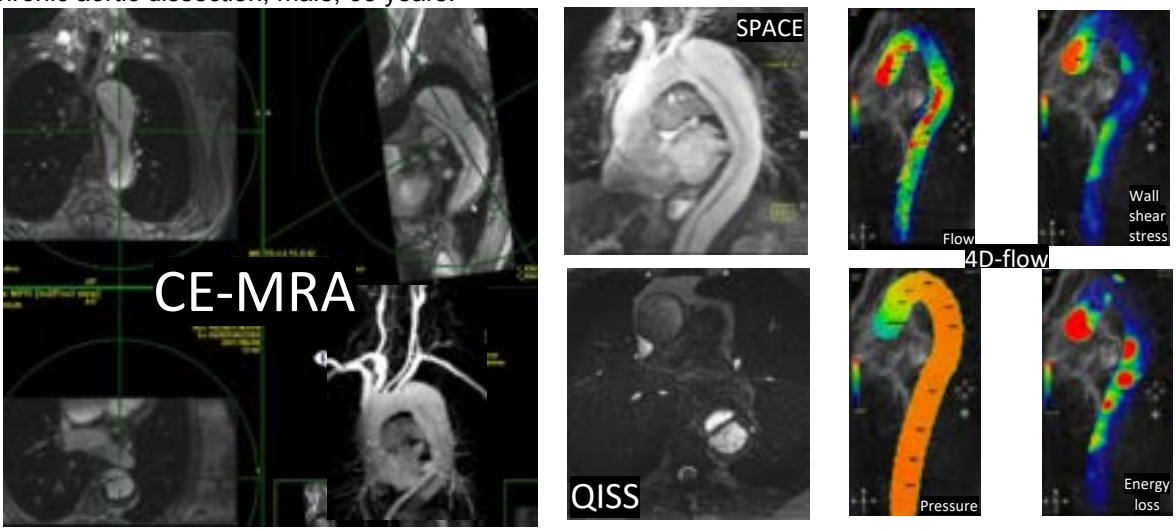

References: [3]Schnell et al, Altered aortic shape in bicuspid aortic valve relatives influences blood flow patterns, European Heart Journal – Cardiovascular Imaging 17, 1239–1247, 2016
[4]Akos Varga-Szemes, MD, PhD et al, Free-Breathing Fast Low-Angle Shot Quiescent-Interval Slice-Selective MR Angiography for improved Detection of Vascular Stenoses in the Pelvis and Abdomen, Abstract SMRA 2019
[5]Michael Markl PhD et al, 4D flow MRI, JOURNAL OF MAGNETIC RESONANCE IMAGING 36:1015–1036, 2012
[6]Ashkan A. Malayeri et al, Utility of a High-Resolution 3D MRI Sequence (3D-SPACE) for Evaluation of Congenital Heart Disease, Pediatr Cardiol (2015) 36:1510–1514, 2015

Abstract ID: 6

Analysis of the value of High Resolution-Vessel Wall Imaging in the etiology of single small subcortical infarction

Yutian Li[1,2] Tong Han[2]

1-Tianjin Medical University, Tianjin, China; 2-Department of Radiology, Tianjin Huanhu Hospital, Tianjin, China

Purpose: The etiology of small subcortical infarct (SSI) located in the region supplied by the perforating artery is still controversial. For SSI without atherosclerotic plaque in the carrier artery, the currently recognized pathogenesis is perforating artery fibrosis or hyalinosis[1]; however, for SSI patients with atherosclerotic plaque found in the carrier artery[2], it's still unclear whether the same pathogenesis exists. In the work, taken atherosclerotic lesions as reference, high resolution-vessel wall imaging (HR-VWI) was used to study biological indicators of SSI such as the total CSVD score, the lenticulostriate artery (LSA) and responsible plaques, so as to further provide imaging indicators for clinical diagnosis.

Methods: 92 patients with acute isolated subcortical cerebral infarction were collected (30 LAA, 28 SUD and 19 SAD patients). MRA/ CTA showed horizontal segment of the middle cerebral artery (MCA)'stenosis rate was less than 50%. Imaging data include infarct information, total cerebral small vessel disease (CSVD) score. The number of LSA trunks, branches, and total length of the patient were measured, and laterality index (LI) of LSA trunks, branches, and total length were calculated. the differences between the LAA group, SUD group and SAD group were compared. Remodeling index (RI) and other plaque characteristics were calculated. The differences between the LAA group and SUD group were compared.

Results: The total CSVD score of the SUD group and the LAA group were lower than that of the SAD group (P=0.017; P=0.001). The lowest cumulative level of the LAA group is lower than that of the SAD group (P=0.004); The incidence of proximal lesions in the LAA group was higher than that in the SAD group (P=0.001). The number and total length of LSA branches in the LAA group and SUD group were shorter than those in the SAD group; the total length LI of LSA in the LAA group and SUD group was greater than that in the SAD group. WA index of the SUD group was higher than that of the LAA group (P=0.037). Wall normalization index (P=0.026), plaque enhancement ratio (P=0.037), and stenosis rate (P=0.006) of the SUD group were lower than those of the LAA group. RI of the SUD group was significantly higher than that of the LAA group (P=0.002) in which positive remodeling were dominant in SUD (60.7%) while LAA was mainly non-positive remodeling (83.3%).

Conclusion: HR-VWI can provide quantitative imaging information of atherosclerotic plaques and perforating arteries and can provide imaging evidence for the diagnosis of the cause of SSI patients. SSI patients with atherosclerotic plaques may also have a coexisting atherosclerotic mechanisms, which are manifested by a lower total CVSD score and a shorter total length of the LSA. The carrier vessel of plaque LSI is mainly non-positive remodeling, while the carrier vessel of plaque SSI is mostly positive remodeling. The microemboli produced by the positively reconstructed unstable plaques may be the pathological mechanism of the appearance of small infarcts.

References:[1] Moran C, Phan TG, et al. International Journal of Stroke, 2011,7(1):36-46.[2] Liao S, Deng Z, Wang Y, et al. Frontiers in Neurology, 2018,9.

Abstract ID: 7

Risk factors of new ipsilateral ischemic lesions after carotid artery stenting: A MRI and clinical study based on high-resolution carotid plaque images

Ranying Zhang[1], Jiang Lin[1]

[1] Department of Radiology, Zhongshan Hospital, Fudan University, and Shanghai Institute of Medical Imaging, Shanghai, China

Background and purpose: Carotid artery stenting (CAS) is an established treatment for carotid stenosis. The most common complication is the new ipsilateral ischemic lesions in the brain after CAS, which may increase the risk of recurrent cerebrovascular events and postoperative cognitive dysfunction[1, 2]. High resolution magnetic resonance imaging (HR-MRI) can provide reliable and non-invasive images of vessel wall and carotid plaque. The current research mainly focuses on the relationship between the clinical-related factors and the new cerebral infarction after CAS[3, 4]. We aimed to investigate the risk factors associated with the new ipsilateral cerebral ischemic lesions within 72 hours after CAS by comprehensively analyzing the clinical information of patients and the morphological characteristics from carotid plaque HR-MRI images.

Materials and Methods: This study retrospectively collected 147 patients who had undergone CAS. The degree of carotid stenosis of all patients was moderate-to-severe (NASCET criteria [5]). Inclusion criteria were: HR-MRI examination of carotid plaque and routine brain MRI within 4 days before CAS, re-examination of brain MRI within 3 days after CAS. Exclusion criteria were: incomplete clinical data, cardiogenic embolism, intracranial vascular disease, restenosis after vascular intervention, new ischemic lesions outside the territory of the treated vasculature and poor-quality MR images. MRI examination was performed on a 3-Tesla scanner (Verio, Siemens, Erlangen, Germany) with an 8-channel carotid coil. Using following sequences to scan the carotid artery around the bifurcation level and obtain the cross-sectional images: 3D time of flight (TOF)、3D T1- / T2-weighted turbo spin-echo (T1W/T2W TSE), and 5-minute delayed post-contrast T1W TSE. Patients were divided into two groups (DWI-positive and DWI-negative) according to whether new ipsilateral high-signal lesions (new cerebral ischemic lesions) appeared in the postoperative DWI images. Clinical information of the patients was collected, including gender, age, history of heart disease, smoking, hypertension, diabetes, hyperlipidemia, symptomatic events and surgery-related information (embolization protective device type, pre-/ post-dilation, and carotid stent type). Morphological features included aortic arch type, aortic arch atherosclerosis, aortic arch ulcer, degree of stenosis, minimal lumen area, plaque burden, remodeling index, contrast enhancement ratio, presence of intraplaque hemorrhage, lipid-necrotic core, and lumen surface irregularity. Univariate analysis (t test, Mann-Whitney U test, or Chi-square test) was used for all variables to assess whether there were differences between two groups. Variables with $P < 0.05$ after univariate analysis were retained for multivariate logistic regression analysis to screen out the independent risk factors of new cerebral ischemic lesions.

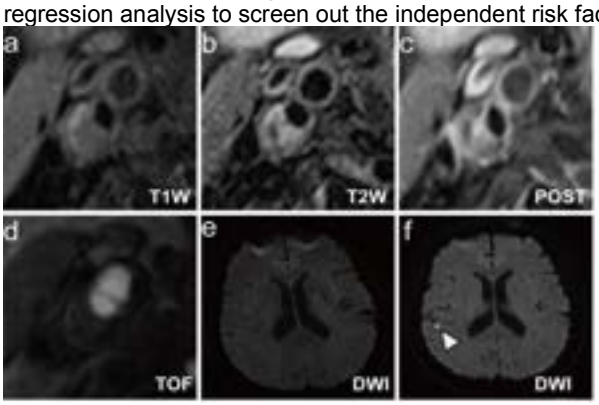

Figure 1: A 66-year-old man with carotid stenosis treated by carotid artery stenting (CAS).
a-d A carotid plaque on T1W, T2W, delayed post-contrast T1W and TOF images.
e DWI of the brain before CAS shows normal findings.
f DWI of the brain after CAS at the same level as e shows new ipsilateral ischemic lesion in the right temporal lobe (white arrowhead).

Results: Among all the enrolled patients (134 male, 13 female; mean age, 67 years), 64 patients were DWI-positive and 83 patients were DWI-negative after CAS within 72 hours. Univariate analysis showed that intraplaque hemorrhage (P=0.007), symptomatic events (P=0.030), post-dilation (P=0.035) and degree of stenosis (P=0.041) existed significant differences between two groups. Multivariate analysis demonstrated that intraplaque hemorrhage (P=0.005; OR = 4.00; 95% CI =1.54-11.23), symptomatic events (P=0.040; OR = 2.53; 95% CI=1.98-6.54) and post-dilation (P=0.007; OR = 3.80; 95%CI =1.44-10.03) were independent risk factors of new cerebral ischemic lesions after CAS.

Conclusion: This study comprehensively analyzed the clinical and morphological factors associated with new ipsilateral ischemic lesions in patients who underwent CAS. It was concluded that intraplaque hemorrhage, symptomatic events and post-dilation were independent risk factors. This report will better help identify patients who are suitable for CAS, especially for those who are also eligible for carotid endarterectomy.

Key Words: Magnetic resonance imaging. Machine learning. Carotid Stenosis. Ischemic stroke.

Reference:[1] Ghogawala Z, et al. [J]. Neurosurgery, 2008, 62(2): 385-395. [2] Gensicke H, et al. [J]. J Am Coll Cardiol, 2015, 65(6): 521-529. [3] Zhou W, et al. [J]. The International journal of angiology, 2011, 20(1): 25-32. [4] Leal I, et al. [J]. J Vasc Surg, 2012, 56(6): 1585-1590. [5] Barnett HJM, et al. [J]. N Engl J Med, 1991, 325(7): 445-53.

Abstract ID: 8

Saturated Multi-delay Arterial Spin Labeling (SAMURAI) Technique for Multiparametric Kidney MRI

Zihan Ning[1], Shuo Chen[1], Zhensen Chen[1], Hualu Han[1], Huiyu Qiao[1], and Xihai Zhao[1]

[1] Center for Biomedical Imaging Research, Tsinghua University, Beijing, China

Purpose: As one of the major global health burden, chronic kidney disease (CKD) can cause a series of complications and may be even life-threatening. Recent years, several studies attempted to evaluate kidney comprehensively by combing multiple MR parameters for early detection of CKD, including renal blood flow (RBF), arterial bolus arrival time (aBAT) tissue BAT (tBAT) and T1-map reflecting function and structure characteristics respectively [1-3]. However, acquiring above multiparametric information usually needs repeated scans for multi-TI ASL or T1-mapping, which prolongs scan time and reduces clinical practicality. **In this study, we proposed a Saturated Multi-delay Arterial Spin Labeling (SAMURAI) technique with a correspondingly modified kinetic model to achieve simultaneous acquisition of RBF, aBAT, tBAT and T1 map in kidney with a single scan.**

Methods: ***Sequence*** The SAMURAI sequence consists of a pre-saturation pulse at imaging slice followed by a nonselective (ns) or slice-selective (ss) inversion pulse for ASL acquisition and Look-Locker SPGR readout (Fig 1). Nine TIs of the Look-Locker SPGR sampling series were set as 0.3:0.3:2.7s. QUIPSS II pulses were performed at bolus duration τ=1.2s. Other imaging parameters include: TE/TR 1.96/3.9ms, TFE factor 30, flip angle 6°, slice thickness 6mm, 40 averages, and CS-SENSE factor 3.2. ***Kinetic Model*** A stepwise kinetic model was proposed based on the classic Buxton model [4], with influence on ASL signal due to Look-Locker sampling scheme corrected [Eq.1a&b]. ***Phantom Experiment*** Phantom experiment was performed on a 3T MR scanner (Ingenia, Philips Healthcare, Best, The Netherlands) with a 32-channel head coil. The SAMURAI sequence (FOV 135×71mm^2, in-plane resolution 1.6×1.6 mm^2, slice thickness 6mm) and a series of standard IR-SE sequences (14 TIs: 0.1:0.1:1/1.5/2/2.5/3s, TE/TR 9.3/10000ms, FOV and resolution were same) were performed for T1-mapping validation. ***In-vivo Experiments*** Nine healthy subjects (3 males, 25.7±2.2 years old) and one patients with renal calculus (male, 23 years old) were recruited for MRI experiments with informed consent. The experiments were conducted on the same MR scanner with a 16-channel torso coil and a 12-channel posterior coil. The SAMURAI sequence was acquired twice (FOV 288×288mm^2, in-plane resolution 3×3 mm^2, slice thickness 6mm, scan time 4'6''). A series of multi-TI FAIR sequences [5] with the same parameters as SAMURAI except for utilization of the Look-Locker strategy (45' for 9 TIs) were performed for validation of T1 and ASL quantification. ***Image Analysis*** All analyses were performed on MATLAB (MathWorks, Natick). T1-map of SAMURAI was obtained by MR fingerprinting-like (MRF-like) methods, with the dictionary generated by Bloch simulation (T1 100:5:3500 ms) and minimum Euclidean distance for the best matching. RBF(f), aBAT(t_A) and tBAT(t_T) were obtained by fitting Eq.1.

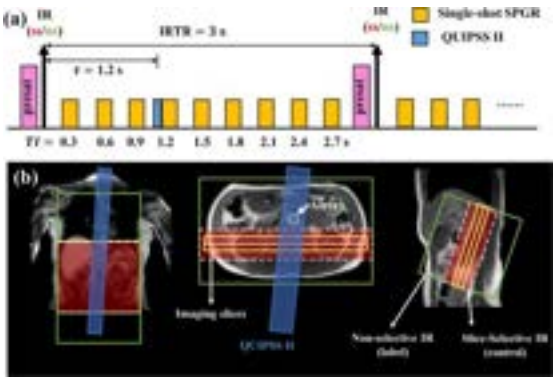

Fig 1. Sequence (a) and positioning (b) diagram of SAMURAI.

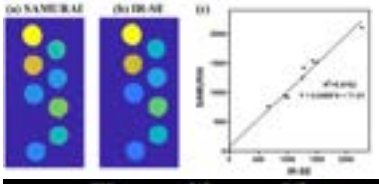

Fig 2. T1 map of SAMURAI (a) and IR-SE (b) and correlation analyses results (c) between them.

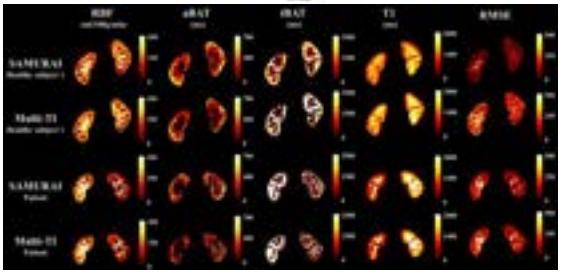

Fig 3. ASL and T1 quantification results of SAMURAI and multi-TI FAIR of a healthy subject (row1&2) and a patient (row3&4).

Table1. Repeatability between scan and rescan and correlation between SAMURAI's and multi-TI FAIR's quantification results measured by ICC and p-value (n=10)

	RBF (ml/100g/min)	aBAT (ms)	tBAT (ms)	T1 (ms)
SAMURAI vs multi-TI FAIR				
p-value	0.943	0.074	0.182	0.999
ICC	0.938	0.734	0.758	0.921
Scan-rescan				
p-value	0.468	0.772	0.788	0.397
ICC	0.964	0.929	0.925	0.925

Results: The proposed SAMURAI technique provided T1 map (Fig 2a) with excellent correlation (R^2=0.976) compared with IR-SE (Fig 2b). Compared with multi-TI FAIR, the SAMURAI technique provided equally reliable ASL and T1 quantification results (ICC:0.734-0.938,p>0.05), with excellent scan-rescan repeatability (ICC:0.925-0.964,p>0.05) (Table 1, Fig 3) and significantly reduced scan time (4'6'' vs 45' for 9 TIs).

$$\Delta M(t) = 2M_{0a}f\int_0^t c(t')\cdot r(t-t')\cdot m(t-t')dt' \quad \text{[Eq.1a]}$$

$$\begin{cases} c(t) = \begin{cases} 0, & 0 < t < t_A \\ \alpha e^{-t/T_{1a}}, & t_A < t < t_A + \tau \\ \alpha e^{-\tau/T_{1a}}(1-e^{-(t-\tau)/T}), & t_T < t \end{cases} \\ r(t,t') = e^{-(t-t')(\frac{1}{T_{1t}}-\frac{1}{T})}, \; t_T < t \\ m(t,t') = e^{-(t-t')(R_2-\ln(\cos\alpha)/TR)} \end{cases} \quad \text{[Eq.1b]}$$

Discussion and Conclusion: This study proposed the SAMURAI technique for simultaneous acquisition of RBF, aBAT, tBAT and T1 map in kidney with reliable ASL and T1 quantification results, excellent repeatability and significantly reduced scan time.

References: [1] Cox EF, et al. Front Physiol 2017;8:696. [2] Shirvani S, et al. Eur Radiol 2019;29:232-40. [3] de Boer A, et al. J Magn Reson Imaging 2020;53:859-73. [4] Buxton RB, et al. Magn Reson Med 1998;40:383-96. [5] Kim SG, et al. Magn Reson Med 1995;34:293-301.

Abstract ID: 9

Comparison of MRI, MRA, and Vessel Wall Imaging features of Cerebral Amyloid Angiopathy and Cerebral Amyloid Angiopathy-Related Inflammation

[a]Vance Lehman MD, [a]John Benson MD, [b]Matthew Koster MD; [c]Tina Gunderson MS, [d]Erika Weil MD, [b]Ashima Makol MBBS, [e]Johnny Sandhu MD, [d]Jonathan Graff-Radford MD

[a]Department of Radiology, Mayo Clinic, Rochester MN [b]Department of Rheumatology Mayo Clinic, Rochester MN [c]Department of Quantitative Health Sciences, Mayo Clinic, Rochester MN [d]Department of Neurology Surgery, Mayo Clinic, Rochester MN [e]Department of Radiology, Mayo Clinic, Jacksonville FL

Purpose. To compare MRI, MRA, and vessel wall imaging (VWI) features of CAA to CAA-ri.

Methods. Imaging of consecutive patients with either CAA or CAA-ri was scored.

Results. 53 patients were identified; 27 with CAA-ri, 26 with CAA. Prevalence of cortical vessel wall enhancement (VWE) did not differ between patients with CAA (10/26, 38%) and patients with CAA-ri (15/27, 56%) (p=0.29); further, neither the co-localization of VWE to other imaging findings nor the extent of VWE differed. Leptomeningeal enhancement was more common in CAA-ri (19/27, 70%) than CAA (13/26, 50%) (p = 0.008), while the number of chronic microbleeds, siderosis, MRA findings, T2 hyperintense lesions, and parenchymal enhancement did not differ. All 7 (100%) patients with extensive leptomeningeal enhancement (> 20 sulci) had CAA-ri.

Conclusions. Findings suggest that extensive leptomeningeal enhancement is a feature of CAA-ri. CAA and CAA-ri were not differentiated by presence, extent, or anatomic pattern of VWE.

Abstract ID: 10

Velocity-based cardiac self-gating in free-running radial 4D Flow MRI

M. Sigovan[1], N. Duchateau[1], P. Douek[1,2], C. Prieto[3], L. Boussel [1,2]

[1] Univ Lyon, Université Claude Bernard Lyon 1, INSA-Lyon, CNRS, Inserm, CREATIS UMR 5220, U1294, F-69621, LYON, France
[2] Department of Interventional Radiology and Cardio-vascular and Thoracic Diagnostic Imaging, HCL, Lyon, France
[3] School of Biomedical Engineering and Imaging Sciences, King's College London, London, UK

Introduction: Free-running whole-heart acquisitions with the capability of deriving cardiac self-gating (SG) signals present clear interest, particularly at 3T, where the ECG signal suffers from the magnetohydrodynamic effect and acquisition related noise. Our goal was to develop a novel velocity-based cardiac SG strategy for free-running radial 4D Flow imaging and to investigate the impact of cardiac SG on the velocity quantification in the thoracic aorta.

Methods: We implemented a free-running interleaved (8 spokes/interleaf) 3D radial velocity mapping sequence on a 1.5T Philips Ingenia (Philips, Best, The Netherlands), based on a spiral phyllotaxis pattern [1]. Imaging was performed on the thorax of 5 healthy subjects as follows: TE/TR 2.5/6 ms, FA=6◦, VENC=180-240 cm/s, 2.5 mm isotropic voxel, acquisition time: 8–12 minutes. First, a sliding-window reconstruction using 64 consecutive spokes and a step of 8 spokes yielded high temporal and low spatial resolution velocity resolved volumes. The average speed in the aorta was obtained for each volume, using a mask drawn on the fully sampled reconstruction. Then, to obtain the cardiac SG signal, the temporal evolution of the aorta average speed was filtered in the frequency domain and interpolated using multiscale kernel ridge regression [2].

Finally, the cardiac SG signal and the ECG were used to bin the data in the same number of cardiac phases (N=12-18). Cardiac and velocity resolved images were then reconstructed offline using a compressed sensing algorithm implemented in Matlab (The Mathworks, Inc, Natick, MA). Velocity measurements in the thoracic aorta were then compared between SG and ECG based gating.

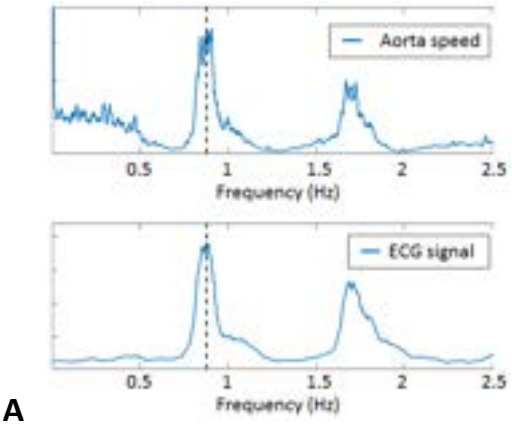

A

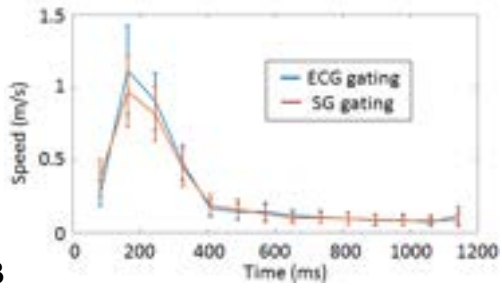

B

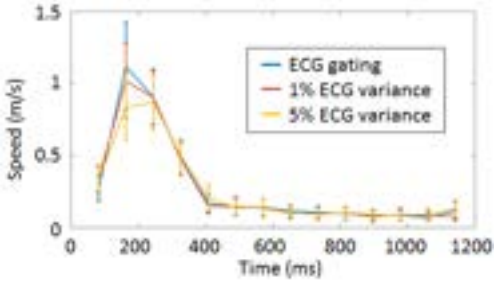

C

Results: A comparison of the frequency analysis of the temporal evolution of the aorta speed and the ECG signal is presented in Figure A for a representative case. The frequency peak corresponding to the heart rate and the first harmonic can be observed at the same location. Despite similar average RR intervals between SG and ECG, the R-peak detection precision for SG was 50ms on average.

Velocity quantification showed underestimation of peak systolic values for SG compared to ECG (Figure B). In order to confirm that the underestimation is due to the R-peak detection precision, we simulated 1% and 5% variability in the R-peak location in the ECG signal by random sampling according to a uniform distribution and used this simulated signal for cardiac binning. Similar to SG, an underestimation can be observed for the same case in the average speed (Figure C).

Discussion: We present here a novel approach to cardiac SG specifically dedicated to 4D Flow MRI. Our results are in agreement with previously reported results using a navigator spoke based method for cardiac SG in 3D radial [3]. While this precision does not affect the resulting anatomical images, we have shown an impact on the velocity quantification, particularly an underestimation of the peak systolic values. This underestimation was described previously for 3D radial 4D Flow [1], however its source was not completely identified. Improvement of the precision in the R-peak detection is expected with the use of more advanced methods in the sliding window reconstruction. In addition, a respiratory SG signal can be obtained in absolute values and enable respiratory motion correction (not shown). This is an advantage of our method, compared to other previous fully self-gated strategies.

Funding: ANR-18-CE19-0025-01

References:

1. Ma LE, Yerly J, Piccini D, et al (2020) Radiol Cardiothorac Imaging 2:e200219
2. Duchateau N, De Craene M, Sitges M, Caselles V (2013) SEE International Conference on Geometric Science of Information (GSI 2013). Paris, France, pp 578–586;
3. Sopra LD, Piccini D, Coppo S, et al (2019) Magn Reson Med 82:2118–2132.

Abstract ID: 11

Non-contrast enhanced 3D Cartesian MRA of the thoracic aorta in 3 min: preliminary clinical evaluation

A Fotaki[1], C Munoz[1], Y Emmanuel[1], A Hua[1], K Kunze[1,2], R Neji[1,2],PG Masci[1], RM Botnar PhD[1] and C Prieto PhD[1]

[1]School of Biomedical Engineering and Imaging Sciences, King's College London, [2]Siemens Healthineers

Purpose: Cardiovascular magnetic resonance angiography (MRA) has been established for serial monitoring of thoracic aortic disease. Conventional 3D bSSFP MRA techniques use diaphragmatic respiratory gating (dNAV) to minimize the effects of respiratory motion in the images, leading to unpredictable and excessively long acquisition times along with the risk of incomplete or aborted scans because of respiratory drift. Additionally, the aortic arch experiences a wide range of displacements during the respiratory cycle[1], that cannot be accurately corrected solely with the clinical dNAV approach. Here we propose to apply and evaluate the performance of a previously introduced non-rigid respiratory motion compensated Cartesian coronary MRA[2] framework, for the visualization of the thoracic aorta in a short and predictable 3 min scan with inline reconstruction.

Methods: An ECG-triggered free-breathing 3D T2prep bSFFP sequence (Fig. 1) acquired with a 3-fold undersampled variable-density Cartesian trajectory[3] and 2D image navigators (iNAVs)[4], reconstructed with non-rigid motion correction[5] inline *(FOV: 400x300x128-154 mm^3, spatial resolution 1.6×1.6×1.6 mm, flip angle = 90°, T2-prep duration = 40ms, TE/TR = 1.72/3.44 ms, coronal orientation*) was evaluated against the clinical 3D T2prep bSSFP with dNAV gating sequence (*FOV 400x300x155-165mm^3, spatial resolution 1.6×1.6×1.6 mm, T2-prep duration = 40 ms, GRAPPA parallel imaging 2x undersampled, flip angle = 90˚, sagittal orientation)* for the visualization of the thoracic aorta. Fifteen patients were scanned with 1.5T MRI scanner (MAGNETOM Aera, Siemens Healthcare, Erlangen, Germany). Two experts blinded to the technique used, recorded their diagnostic confidence (from 1: poor diagnostic confidence to 4: full diagnostic confidence). Co-axial aortic dimensions in three landmarks were measured by one reader with both sequences and twice with the proposed apporach and intra-observer variability was assessed.

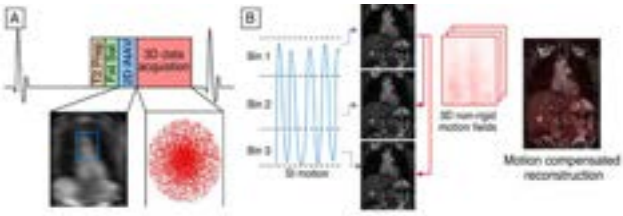

Fig. 1: Acquisition (A) and non-rigid motion corrected reconstruction (B) framework for the aortic iNAV T2 prep bSSFP.

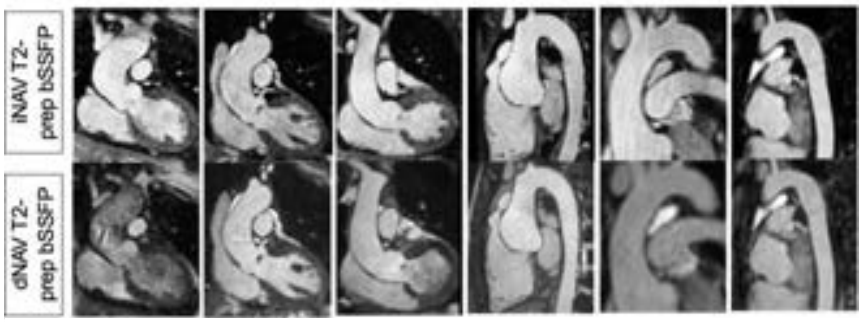

Fig. 2: Images of the thoracic aorta for six representative patients. Proposed (iNAV) and conventional (dNAV) non-CE MRA are showed in the first and second row respectively.

Results: Good quality depiction of all thoracic aortic segments (Fig. 2) in short scan time was achieved with the iNAV-based approach [3.1±1.1min (iNAV) versus 11.5 min±3.4 (dNAV), P<0.0001]. The reconstruction time for the proposed sequence was 3±0.3 min inline on the scanner. Diagnostic confidence was high and similar to the proposed and the clinical sequence for both reviewers (Reviewer 1: 3.80±0.41 vs 3.86±0.35,P=1; Reviewer 2: 3.86±0.35 vs 3.93±0.26,P=0.6). Bland Altman analysis showed very good agreement in the co-axial aortic measurements of the aortic root, sinotubular junction and mid-ascending aorta between the two datasets, with a small mean difference of <0.03 cm across these landmarks (Fig.3). Intraclass Correlation Coefficient showed excellent intra-observer reproducibility at the corresponding anatomic segments [aortic root (0.9; 95% CI: 0.82, 0.95), sinotubular junction (0.89; 95% CI: 0.79, 0.93), mid-ascending aorta (0.9; 95% CI: 0.81, 0.95)].

Discussion: Thoracic aortic iNAV-based MRA with fast acquisition (3 min) and inline reconstruction (3 min) provided

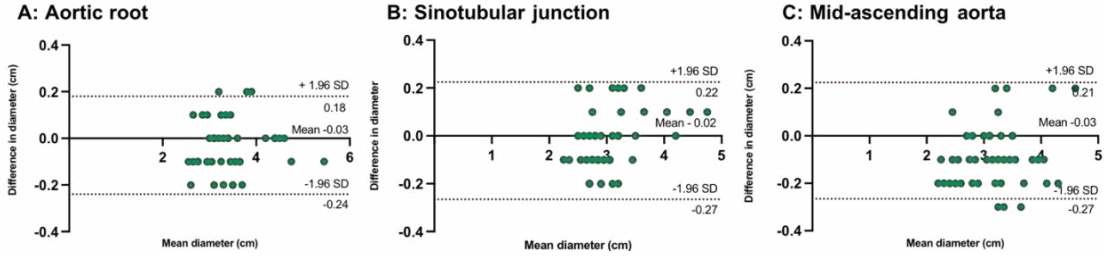

Fig. 3: Bland-Altman plots for co-axial diameter measurements of the aortic root (A), sinotubular junction (B) and mid ascending aorta (C) between the dNAV and the iNAV T2prep-bSSFP sequence for one reviewer.

high-quality visualisation of the thoracic aorta in a cohort of patients with thoracic aortic disease. High diagnostic confidence and reproducible aortic measurements are promising for imminent clinical integration.

References: 1. Sailer AM et al. Journal of Endovascular Therapy. 2015;22(6):905-911. 2. Cruz G et al. Magn Reson Med. 2017;77(5):1894. 3.Prieto C. et al. J Magn Reson Imaging 41:738–746. 4. Henningsson M et al. Magn Reson Med. 2012;67:437- 445. 5. Bustin A. et al, J Cardiovasc Magn Reson. 2020;22(1).

Abstract ID: 12

Automatic time-resolved cardiovascular segmentation of 4D Flow MRI using Deep Learning

Mariana Bustamante[1,2], Jan Engvall[1,3], Carl-Johan Carlhäll[1,2,3] and Tino Ebbers[1,2]

[1]Division of Diagnostics and Specialist Medicine; Dept. of Health, Medicine and Caring Sciences; Linköping University, Sweden
[2]Center for Medical Image Science and Visualization (CMIV), Linköping University, Sweden
[3]Dept. of Clinical Physiology in Linköping, Dept. of Health, Medicine and Caring Sciences; Linköping University, Sweden

Purpose: Segmenting the whole heart over the cardiac cycle is a challenging and time-consuming process, as there is considerable motion and limited contrast between blood and tissue. The aim of this study was to develop and evaluate a deep learning based segmentation method to automatically segment the cardiac chambers and great thoracic vessels from 4D Flow MRI over the cardiac cycle. The resulting segmentations should be suitable for visualization and analysis of hemodynamic parameters of 4D Flow MRI in large cohort research studies and clinical workflow.

Methods: A deep learning model based on the 3D U-net architecture [1] was trained and evaluated on a set of 205 4D Flow MRI acquisitions [2], including 40 healthy volunteers and 165 patients with a variety of medical diseases. These datasets were segmented using a previously reported atlas-based approach [3], followed by manual correction were appropriate. To train the neural network, the group was randomly divided into 144 of 205 for training, 20 of 205 for validation, and 41 of 205 for testing. Each MR acquisition was reconstructed to cover the entire cardiac cycle in 40 timeframes; accordingly, the CNN was trained using each timeframe as an independent segmentation. This resulted in 5760 3D volumes for training, 800 3D volumes for validation, and 1640 3D volumes for testing.

Results: Mean Dice score for all 4 cardiac chambers, aorta and pulmonary artery was 0.908 ± 0.023 (mean ± SD), with the highest scores in the aorta, left ventricle, and left atrium, and slightly lower scores in the right ventricle and right atrium. This was confirmed by Hausdorff distance and average surface distance (Fig. 1). The median result in the test set according to Dice scores is shown in Fig. 2.

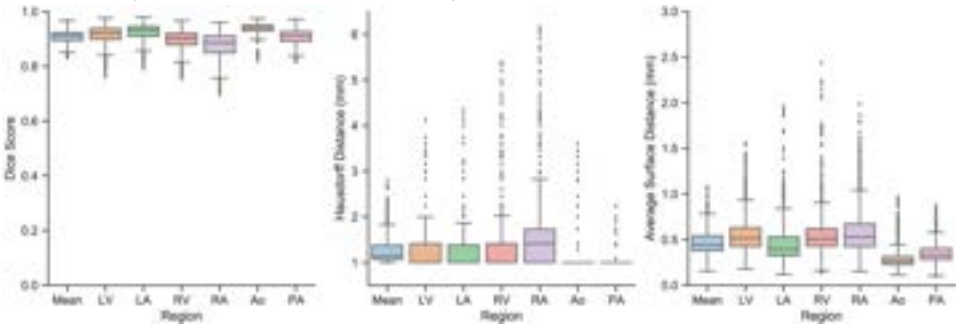

Figure 1: : Metric results on the test dataset for each region included in the segmentations. Left: Dice Score, center: Hausdorff Distance (mm), right: Average Surface Distance (mm).

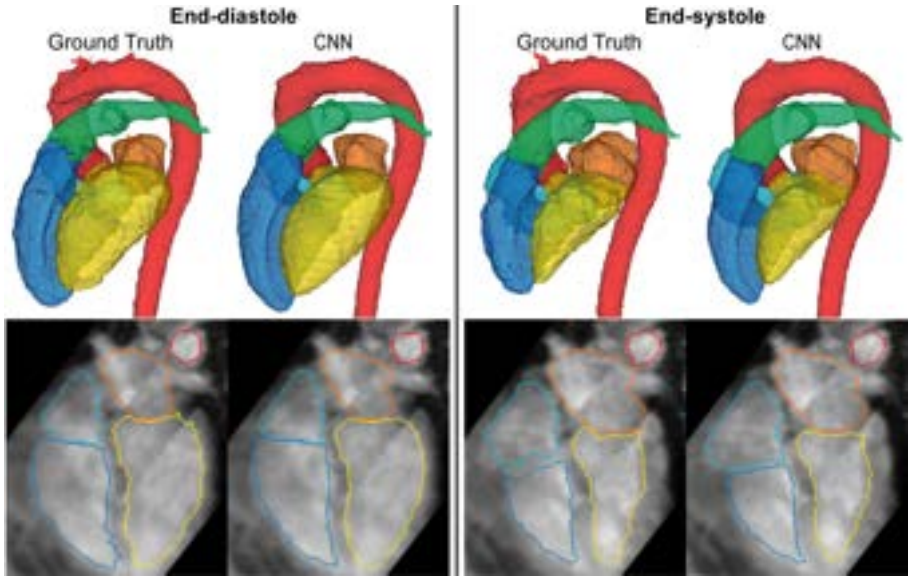

Figure 2: Median result in the test set according to Dice scores visualized as isosurface renderings (top) and superimposed over a four-chamber image of the heart (bottom). Each row includes a comparison between the ground truth segmentations and those generated by the proposed method (CNN) at end-diastole and end-systole.

Discussion: The proposed method reduces the time required to generate a full four-dimensional segmentation when compared to the previously published atlas-based technique from 25 minutes to approximately 6 seconds per acquisition, which represents a significant runtime improvement. The segmentations include all the regions of interest within the acquisition and can be used to perform a comprehensive assessment of the blood-flow hemodynamics. Addition of this technique to the 4D Flow MRI assessment pipeline would expedite and significantly improve the utility of this type of acquisition in the clinical setting.

References: **[1]** O. Cicek et al. 3D U-Net: Learning Dense Volumetric Segmentation from Sparse Annotation. *MICCAI*, 2016. **[2]** M. Markl et al. Comprehensive 4D velocity mapping of the heart and great vessels by cardiovascular magnetic resonance. *Journal of Cardiovascular Magn. Res.* 13(1):7, 2011. **[3]** M. Bustamante et al. Automated multi-atlas segmentation of cardiac 4D flow MRI. *Medical Image Analysis*, 49:128-140, 2018.

Abstract ID: 13

Vascular Mapping of the Human Hippocampus *in vivo* Using MICRO Imaging

Sagar Buch[1], Yongsheng Chen[2], Pavan Jella[1], Yulin Ge[3] and E. Mark Haacke[1,2*]

[1] *Department of Radiology, Wayne State University, Detroit, MI, USA*

[2] *Department of Neurology, Wayne State University, Detroit, MI, USA*

[3] *Center for Biomedical Imaging, Department of Radiology, New York University School of Medicine, New York, NY, USA*

***Purpose*:** The hippocampus is a complex grey matter structure that plays an important role in spatial and episodic memory. It can be affected by a wide range of pathologies including vascular abnormalities. We recently introduced the concept of MICRO (*Microvascular In-vivo Contrast Revealed Origins*) protocol to image cerebral vessels ≤100μm in diameter [1]. MICRO uses Ferumoxytol, an ultra-small superparamagnetic iron oxides (USPIO) agent, to induce susceptibility in the arteries and veins. In this work, we use MICRO imaging to map the hippocampal microvasculature, evaluate the change in fractional vascular density (FVD) in each of its subfields and estimate the subfield volume as a function of age.

Methods: A total of 35 healthy volunteers (aged 35.2±14.6 years, from 18 to 81 years old, women=20) were scanned on a 3T Siemens VERIO scanner with a high-resolution SWI sequence at four time points during a gradual increase in Ferumoxytol dose. The imaging parameters were: TE1/TE2/TR=7.5/15/27ms, bandwidth=180Hz/pixel; with a voxel size = $0.22\times0.44\times1mm^3$ (interpolated to $0.22\times0.22\times1mm^3$). Dynamically acquired SWI data were co-registered and adaptively combined to reduce the blooming artifacts from large vessels, preserving the small-vessel contrast [1]. Frangi vesselness filter was used on the resultant SWI data to segment the microvasculature and the FVD of the subfields was measured [2].

Results: The presence of Ferumoxytol helped to enhance the hippocampal microvasculature, something that has previously only been demonstrated in cadaver brain studies (Figure 1). The hippocampal fissure, along with the fimbria, granular cell layer of the dentate gyrus and cornu ammonis layers (except for CA1), showed higher microvascular FVD than other parts of the hippocampus. On the other hand, the FVD of major arteries and major veins was higher in the hippocampal fissure and CA2/3 composite regions, suggesting a stronger probability that these regions serve as the entry/exit area for the penetrating arteries and draining veins. There was also a reduction in FVD, especially for the parasubiculum, presubiculum, subiculum, CA1 and CA2/3 subfields as a function of age. The CA1 region exhibited a significant correlation with age ($R = -0.37$, $p < 0.05$), as shown in Figure 1. In addition, the total hippocampal FVD showed a negative correlation with age, demonstrating an overall loss of hippocampal vascularity in the normal aging process. However, the volume changes showed a weakly negative or lack of correlation as a function of age.

Discussion: By administering Ferumoxytol, the small vessels in the brain can be enhanced. The hippocampus exhibited a reduction in FVD as a function of age, suggesting that the hippocampus becomes more vulnerable to further reductions in flow due to normal aging, especially in the CA1 territory. This vascular density reduction was more prominent than the volume reduction of the subfield, which could indicate that vascular atrophy is a precursor to the tissue volume reduction due to the reduction of oxygen supply and, hence, the reduction of tissue metabolism.

***References*:** [1] Buch, S. *et al. NeuroImage* 220, 117106 (2020). [2] Frangi A et al. in Medical Image Computing and Computer Assisted Intervention vol. 1496 of Lecture Notes in Computer Science 130–137 (1998).

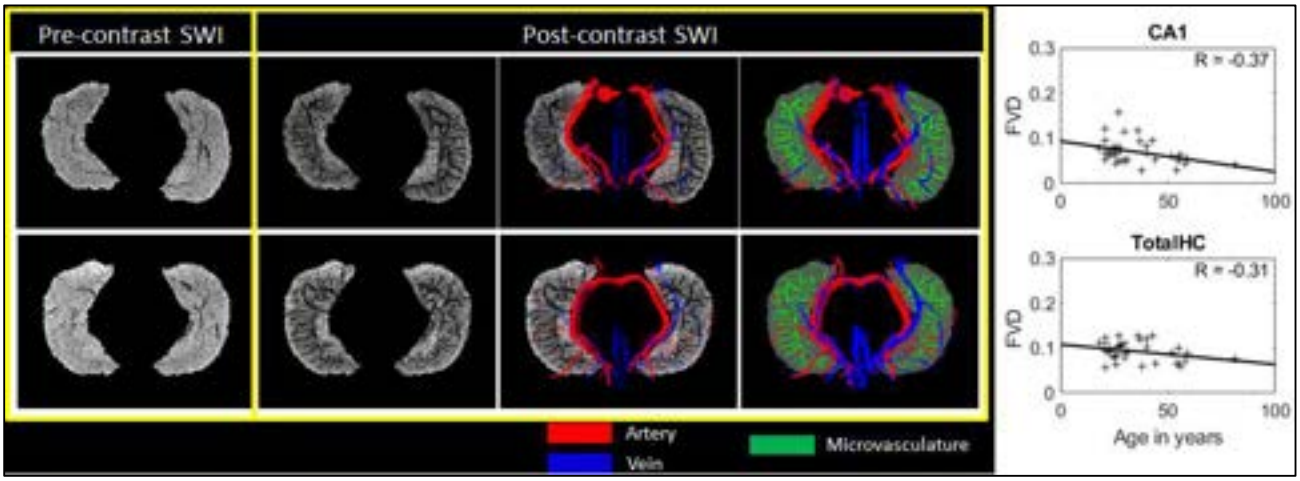

Figure 1. Revealing the microvasculature of the hippocampus using USPIO. Pre- and post-contrast SWI data, for two healthy subjects (each in one row), are displayed with the overlays of major arteries (red), major veins (blue) and intra-hippocampal microvasculature (green). Although the pre-contrast SWI was able to highlight the presence of major veins due to the presence of deoxyhemoglobin, the vascular contrast from both arteries and veins was improved significantly on the post-contrast SWI data. The plots represent the age-dependent changes in the FVD for the CA1 subfield and for the entire hippocampus (TotalHC). Pearson correlation coefficients (R) are indicated in the top-right corner of the plots.

Abstract ID: 14

Quantification of cerebral oxygen extraction fraction of the medial temporal lobe

Dengrong Jiang[1], Peiying Liu[1], Zixuan Lin[1], Abhay Moghekar[2], Jay J. Pillai[1], Hanzhang Lu[1]
[1]Department of Radiology, Johns Hopkins University, [2]Department of Neurology, Johns Hopkins University

Purpose: The medial temporal lobe (MTL), including the hippocampus, is a key area implicated in many brain diseases such as Alzheimer's disease (AD), schizophrenia, and epilepsy.[1] To date, we still lack non-invasive techniques to measure its oxygen extraction fraction (OEF), which is a quantitative indicator of neural function. In this work, we aimed to develop a novel technique to measure OEF in the basal veins of Rosenthal (BVs), which are major draining veins of the MTL.

Methods: *Pulse sequence:* The proposed sequence is based on accelerated-T_2-relaxation-under-phase-contrast (aTRUPC) MRI.[2] aTRUPC uses phase-contrast complex subtraction to isolate pure blood signals in the vessels. Venous T_2 is quantified by using T_2-preparation (T_2-prep) with varying effective TEs (eTEs) and then converted to venous oxygenation (Y_v).[2] To suppress the posterior cerebral arteries (PCAs) adjacent to BVs, we added arterial suppression modules to aTRUPC. Fig. 1 shows the sequence diagram.

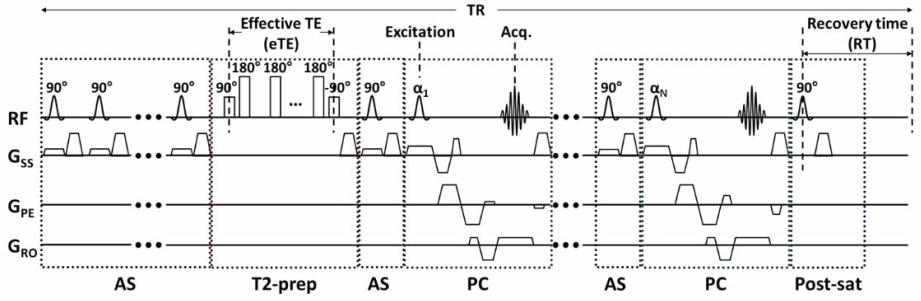

Fig 1. Sequence diagram, consisting of arterial suppression (black boxes), T_2-prep (red box), phase-contrast acquisition (green boxes) and post-saturation (blue box). TOF MRV shows the position of imaging slice

MRI experiments: 12 healthy subjects (7M5F, age 38±12) were scanned. To visualize the BVs, a TOF MRV was first performed. Maximum-intensity-projection images were obtained, and the aTRUPC slice was placed to align with the trajectory of BV along the anterior to posterior direction (Fig 1). aTRUPC used: single slice, voxel-size = 0.8×0.8×10mm^3; 3 eTEs: 0, 40 and 80ms; 4 averages; scan time = 4.8min. Arterial suppression used 20 pulses before T_2-prep and a gap of 10mm between the arterial suppression slab (40mm thick) and the imaging slice (Fig 1). On each subject, Y_v was quantified in 4 regions of interest (ROIs): ROI1&2 on BVs, ROI3 on great vein (GV) and ROI4 on superior sagittal sinus (SSS) (Fig 2). OEF was calculated as: OEF = $(Y_a-Y_v)/Y_a\times100\%$, where arterial oxygenation Y_a is assumed to be 98%. To evaluate the sensitivity of our technique to OEF changes, we conducted a caffeine challenge on two of the subjects (1M1F, age 28±2). Each subject first underwent one baseline aTRUPC scan, then took one 200mg caffeine tablet and underwent another 8 aTRUPC scans.

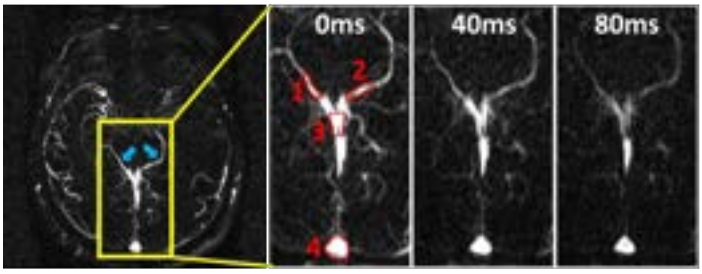

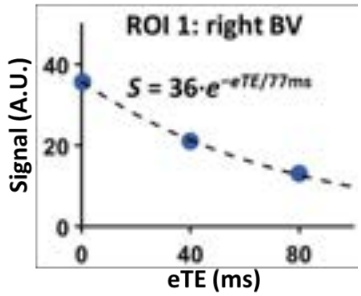

Fig 2. aTRUPC images of a representative subject. Zoom-in views of 3 eTEs are shown. Red contours represent the ROIs for OEF quantification. The scatter plot displays venous signal intensities as a function of eTEs for ROI1.

Results and Discussion: Fig 2 shows aTRUPC data of a representative subject. Left and right BVs are indicated by blue arrows. Across the subjects, the OEF were 25.3±4.8, 26.3±3.1, and 35.6±4.1% for BV, GV and SSS, respectively. As shown in Fig 3, OEF in BV and GV had no significant difference (P=0.25), but both were lower than OEF in SSS (P<0.0001). Fig 4 plots OEF changes in caffeine challenge, averaged across the 2 subjects. After caffeine ingestion, OEF increased in all veins, which agreed with literature[3] and demonstrated the sensitivity of our technique to OEF changes.

Conclusion: We developed a novel technique to measure OEF in MTL, which facilitates future studies of brain diseases such as AD.

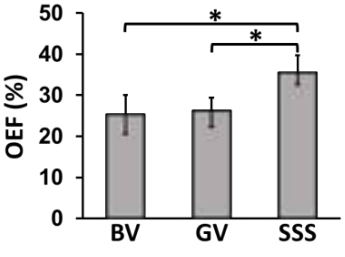

Fig 3. OEF in BV, GV and SSS across subjects.

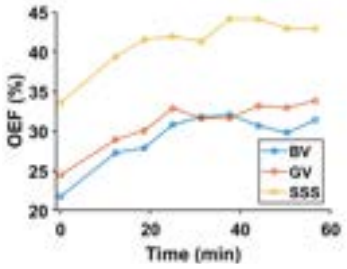

Fig 4. OEF at baseline (Time=0) and after caffeine ingestion.

References: [1] Jack et al. Neurology 1997;49:786-794; [2] Jiang et al. MRM 2019;82:1129-1139; [3] Xu et al. NeuroImage 2015;110:39-47.

Abstract ID: 15

Predicting Delayed In-Stent Stenosis following Flow Diversion of Unruptured Aneurysms using Vessel Wall MRI

Costello J, Alexander MD, McNally JS, de Havenon AH, Parker DL, Grandhi R
[1]Walter Reed Medical Center Department of Radiology, Washington, D.C., USA, [2]Department of Radiology and Imaging Sciences, University of Utah, Salt Lake City, USA, [3]Department of Neurosurgery, University of Utah, Salt Lake City, USA, [4]Department of Neurology, University of Utah, Salt Lake City, USA

Domain Conflicts: utah.edu; Medtronic.com; Cerenovus.com; siemens.com; aha.org

Purpose
Delayed stenosis is a known complication following flow diversion for cerebral aneurysms. While typically well tolerated, accurate detection is important to ensure correct management. Vessel wall MRI (vwMRI) studies using black blood (BB) sequences can improve evaluation of intracranial vascular pathologies, including aneurysms. vwMRI studies obtained after FD treatment of unruptured intracranial aneurysms were assessed for ability to predict stenosis on subsequent digital subtraction angiography (DSA).

Methods
According to an IRB-approved protocol, a prospectively maintained database of patients was queried to identify patients undergoing FD placement for unruptured aneurysms without adjunctive coiling. According to clinical protocols, patients treated with a FD undergo vwMRI at three months and DSA at six months. Individuals with confirmed narrowing on six-month DSA were identified, and control cases were then selected, matching for age, biological sex, vessel segment, and aneurysm type. The three-month follow up vwMRI studies were then evaluated by two radiologists with certificate of added qualification in neuroradiology blinded to DSA findings during assessment of vwMRI. Luminal measurements and apparent stenosis were measured on 3D time of flight (3DTOF) and post-contrast MRA, as well as pre- and post-contrast black blood (BB) images. Stenosis was calculated using the WASID criteria. Flow limitation on MRA, visualization of soft tissue in the lumen on BB, or intimal enhancement within the stent were also noted. Fisher's exact tests were performed to assess similarities of the two study groups and identify vwMRI features associated with stenosis on subsequent DSA. A multivariable exact logistic regression model was then constructed including variables with $p \leq 0.200$.

Results
Data were analyzed from 15 patients, with no difference between groups for age (p=0.267), biological sex (p=0.706), aneurysm location (p=0.706) or morphology (p=0.706), or imaging timing (p=0.524). Stenosis on BB was associated with stenosis on subsequent DSA (p=0.035), while there was no such association found for 3DTOF (p=0.264) or postcontrast (p=0.210) MRA. Downstream flow limitation on 3DTOF (p=0.004) and postcontrast (p-0.001) MRA, as well as visualization of enhancing intima within the FD (p=0.001), were associated with stenosis on subsequent DSA. Suspected soft tissue visualized in the lumen on BB was not associated with stenosis on subsequent DSA (p=0.231). Multivariable analysis found retained significance for stenosis and intimal enhancement on BB (p=0.001).

Conclusions
Stenosis and intimal enhancement within the FD on BB vwMRI sequences are associated with presence of stenosis in the FD on subsequent DSA. Apparent stenosis on 3DTOF or post-contrast MRA correlates poorly with DSA findings. Flow limitation from suspected stenosis on these sequences is associated with stenosis on DSA, although these are less predictive than the BB findings.

References
1. Mossa-Basha M, Alexander M, Gaddikeri S, Yuan C, Gandhi D. Vessel wall imaging for intracranial vascular disease evaluation. J Neurointerv Surg. 2016 Nov;8(11):1154–9.

2. Mühl-Benninghaus R, Haußmann A, Simgen A, Tomori T, Reith W, Yilmaz U. Transient in-stent stenosis: a common finding after flow diverter implantation. J Neurointerv Surg. 2019 Feb;11(2):196–9.

Abstract ID: 16

Simultaneous non-contrast enhanced 3D coronary MRA and plaque imaging in patients with acute coronary syndrome

R Hajhosseiny[1,2], A Hartley[2], G Cole[2], A Sethi[2], R Al-Lamee[2], D Gopalan[2], R Kaprielian[2], R Neji[1], K Kunze[1], C Prieto[1], R Khamis[2*], RM Botnar[1*]

[1]School of Biomedical Engineering and Imaging Sciences, King's College London, St. Thomas' Hospital, London, UK
[2]National Heart and Lung Institute, Imperial College London, Hammersmith Hospital, London, UK
[*]Joint senior authors

Introduction: Rupture of an atherosclerotic plaque is the main trigger of myocardial infarction, the leading cause of mortality worldwide. Coronary vulnerable plaque identified on cardiovascular magnetic resonance (CMR) is significantly associated with future coronary events, independent of coronary lumen stenosis[1]. However, CMR plaque imaging is clinically limited by low spatial resolution, misregistration artefacts, respiratory motion related image quality degradation and unpredictable acquisition times. We have recently developed a novel 3D free-breathing non-contrast CMR sequence (BOOST) that allows for simultaneous high-resolution visualisation of the coronary arteries and vulnerable plaque on co-registered bright and black blood images[2,3]. Here, we investigate the feasibility of this technique in patients with acute coronary syndrome (ACS) and validate it against the gold standard imaging modalities of invasive X-ray coronary angiography and optical coherence tomography (OCT)/intravascular ultrasound (IVUS).

Methods: The proposed 3D sequence interleaves the acquisition of a T2prep-IR prepared bright-blood dataset with a T1 weighted (T1w) dataset without magnetization preparation[3]. The bright-blood T2prep-IR dataset enables visualisation of the coronary lumen. Subtraction of the T2prep-IR dataset from the T1w dataset results in a coregistered black-blood dataset that enables visualisation of the coronary vessel wall, thrombus and intraplaque haemorrhage. 2D image-based navigation and respiratory binning enables 2D translational motion correction and 3D non-rigid motion estimation. The final image is obtained using a 3D non-rigid motion compensated iterative sense reconstruction for each contrast before subtraction. Reconstruction is implemented inline on the scanner. The proposed approach enables 100% scan efficiency and predictable scan times. The acquired spatial resolution is 1.2x1.2x1.2 mm^3 with 3-fold undersampling and an acquisition time of <15 minutes. The proposed sequence was compared against invasive X-ray angiography and intravascular imaging (OCT or IVUS) in a cohort of 10 patients who presented to our unit with ACS. For visualisation purposes only, a second black-blood image was obtained with phase-sensitive inversion recovery (PSIR)-like reconstruction of the T2prep-IR and T1w datasets which was used for image fusion with the vessel wall (subtraction-based black-blood as described above) dataset.

Results and Conclusion: Figure 1 demonstrates the images of a 54-year-old male patient with type 2 diabetes mellitus, hypertension and 35-year smoking history. He presented to our Heart Assessment Centre with 48 hours of worsening chest pain. Peak high-sensitivity troponin was elevated at 2218ng/L. His electrocardiogram was normal. Images A-E show a critical stenosis in the proximal right coronary artery (RCA) with corresponding acute intracoronary thrombus. Images F-J show diffuse severe stenosis in the proximal to mid left anterior descending artery (LAD). In summary, the proposed BOOST framework has the potential to simultaneously visualise coronary artery stenosis as well as coronary thrombus/plaque in patients with ACS.

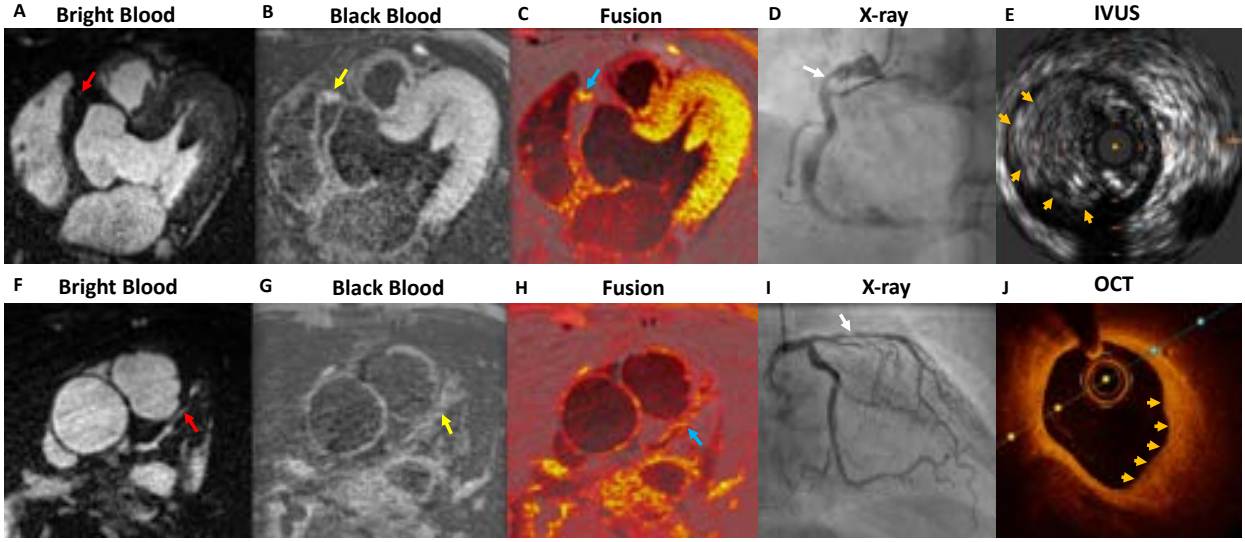

Figure 1: A- Bright blood coronary MR angiography showing a critical proximal RCA stenosis (red arrow). **B-** Acute intracoronary thrombus of the proximal RCA on black blood vessel wall images (yellow arrow). **C-** Fusion of the black blood vessel wall images with the black blood PSIR dataset for anatomical correlation (blue arrow). **D-** Critical proximal RCA stenosis on X-ray angiography (white arrow). **E-** Acute intracoronary thrombus on intravascular ultrasound (IVUS) (orange arrows). **F-** Bright blood coronary MR angiography showing severe proximal to mid LAD stenosis (red arrow). **G-** Diffuse atherosclerosis on black blood vessel wall images (yellow arrow). **H-** Fusion of the black blood vessel wall images with the PSIR dataset for anatomical correlation (blue arrow). **I-** Diffuse severe proximal to mid LAD stenosis on X-ray angiography (white arrow). **J-** Diffuse high signal fibrotic atherosclerosis on optical coherence tomography (OCT) (orange arrows).

References: 1. Noguchi et al, JACC 2014; 2. Ginami et al, MRM 2018. 3. Milotta et a. MRM 2019.

Abstract ID: 17

Deep-Learning based Reconstruction of Highly Accelerated 4D Flow MRI

Haben Berhane[1], Ashitha Pathrose[1], Michael Scott[1], Patrick McCarthy[2], Chris Malaisrie[2], James Carr[1], Ryan Avery[1], Michael Markl[1]
[1]Radiology, [2]Cardiac Surgery, Northwestern University, Chicago, IL

Purpose: 4D flow MRI provides spatiotemporally-resolved information on blood flow dynamics enabling comprehensive hemodynamic evaluation. Currently, the clinical use of 4D flow MRI is hindered by long scan times. Recently, multiple studies demonstrated the feasibility of a Compressed Sensing (CS)-accelerated 4D flow MRI of the thoracic aorta in under 2 min [1,2]. However, various hemodynamic measurements were underestimated by CS-accelerated 4D flow MRI when compared to conventional, GRAPPA accelerated 4D flow [1,2]. Deep learning based MRI reconstruction has shown to be highly effective in reconstructing highly accelerated MRI data, including real-time 2D phase contrast MRI and 4D flow MRI [3,4]. We seek to expand on these advancements by developing a 3D Dense U-Net for reconstruction of highly accelerated 4D flow MRI to improve hemodynamic quantifications compared to CS reconstruction.

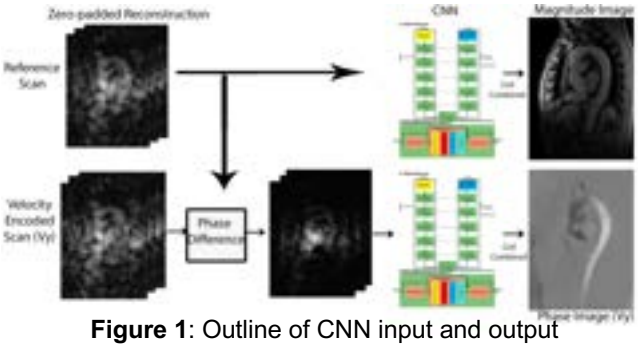

Figure 1: Outline of CNN input and output

Methods: For this study, 18 subjects with aortic disease were included (10 for training and 8 for testing; 58 ± 15 y old; 14 M). Each subject underwent four 4D flow MRI scans: (1) GRAPPA, R=2, (2) CS, R=5.7, (3) CS, R=7.7, (4) CS, R=10.2. All scans were acquired using a 1.5T scanner (Aera, Siemens) with identical field-of-view (2.4-4.2 mm^3). These subjects were included in a prior study [2]. The CNN used was a hybrid 3D DenseNet/U-Net as previously described [5]. Figure 1 provides an outline for the CNN-based reconstruction. The input to the CNN were zero-padded reconstructed CS-accelerated R=10.2 datasets, while the ground-truth was the GRAPPA-accelerated 4D flow MRI (R=2). Only image-space of the data was used in the CNN. The real and imaginary elements separated and concatenated together for an input size (2,X,Y,slices,coils) and recombined (as real + j*imaginary) in the output. Each time frame is fed separately to the CNN. The coils were combined after going through the CNN using root-sum-squares. For the magnitude images, the reference scan was used as an input to the CNN, while for the phase images, the phase difference data, between the velocity-encoded and reference scan, were used. The loss function consisted of a structural similarity index (SSIM) loss function + mean squared error. Peak velocity, net flow, and peak flow were obtained for the ascending aorta (AAo), aortic arch, and descending aorta (DAo) and compared using Bland-Altman analysis, with the bias and limits of agreement (LOA), as the percent different from the mean, reported. For the magnitude images, SSIM values were calculated with $\sigma_{SSIM} = 1.5$.

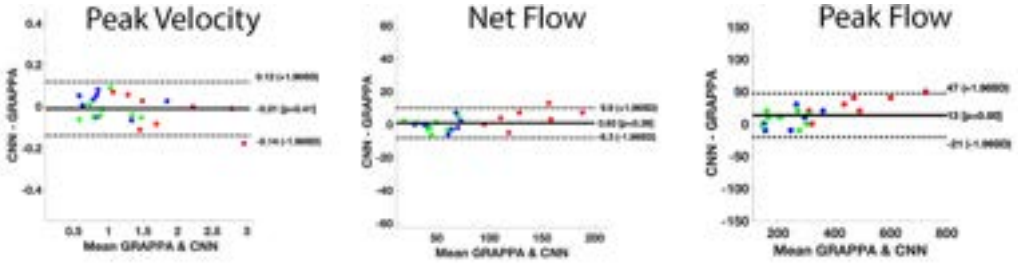

Figure 2: *Bland-Altman plots for peak velocity, net flow, and peak flow between GRAPPA (R=2) and CNN, red=AAo, green=arch, blue=DAo*

Results: The reconstruction time for the CNNs was 212 ± 8 seconds, compared to ~240-360 seconds for CS reconstruction. The median SSIM index for the magnitude images was 0.87 [0.85 – 0.90]. Figure 2 highlights the Bland-Altman comparisons between the CNN reconstructed CS, R=10.2 data and GRAPPA, R=2 data across all regions. The Bland-Altman comparisons between the GRAPPA, R=2 and CNN-based, CS R=10.2 showed moderate to excellent agreement for peak velocity (AAo: bias=0.3m/s, LOA= 9.02% mean difference; arch: bias=0.02 m/s, LOA=10.7% mean difference; DAo: bias=0.2m/s, LOA=10.2% mean difference), net flow (AAo: bias=3.4mL, LOA=7.4% mean difference; arch: bias=-.25mL, LOA=13.4% mean difference; DAo: bias=-0.63mL, LOA=15.1% mean difference), and peak flow (AAo: bias=28mL/s, LOA=7.1% mean difference; arch: bias=3.8mL/s, LOA=12.4% mean difference; DAo: bias=7.5 mL/s, LOA=9.9% mean difference). The CNN showed better agreement with GRAPPA, R=2 data than the CS, R=5.7 data (across all regions, peak velocity: bias=-0.13-0.06 m/s, LOA=16-29% mean difference; net flow: bias=0.69-3.4mL, LOA=16%-23% mean difference; peak flow: bias=-15-19 mL/s, LOA: 14-23% mean difference); CS, R=7.7 data (across all regions, peak velocity: bias= -0.18- -0.01 m/s, LOA=10-28% mean difference; net flow: bias=0.07-4.2mL, LOA=28%-34% mean difference; peak flow: bias=-21-0.18mL/s, LOA=14-18% mean difference); and CS, R=10.2 data (across all regions, peak velocity: bias=-0.2-0.04 m/s, LOA=14-44% mean difference; net flow: bias=-3.3-4.8mL, LOA=18%-24% mean difference; peak flow: bias=-4.4- -22mL/s, LOA=16-24% mean difference).

Discussion: The CNN-based reconstruction of CS, R=10.2 4D flow MRI showed excellent agreement with conventional GRAPPA, R=2 4D flow MRI. Future direction of this study is to explore CNN reconstruction on higher acceleration factors.

References: [1] MA, L. et al. *MRM*. 2019. [2] Pathrose, A. et al. *MRM*. 2020. [3] Valizadeh, HH. et al. *MRM* 2021. [4] Vishnevskiy V. et al. *Nature Machine Intell*. 2020. [5] Berhane, H. et al. *MRM*. 2020

Abstract ID: 18

Respiratory Resolved Flow in the Fontan Circulation: A 5D Flow MRI Case Study

Elizabeth Weiss[1,2], Liliana Ma[1,2], Cynthia Rigsby[2,3], Joshua Robinson[3], Michael Markl[1,2]

[1]Northwestern Biomedical Engineering, [2]Northwestern Radiology, [3]Lurie Children's Hospital of Chicago

Purpose: Previous studies have demonstrated the potential of 4D flow MRI for the detailed assessment of cardiovascular flow dynamics in complex congenital heart disease, such as single ventricle physiology.[1] However, 4D flow MRI is limited by its long, unpredictable scan times, need for external signals for cardiac and respiratory gating, and single respiration state acquisition. This narrows its utility especially in pediatric patients with complex congenital heart disease. To address these limitations, we have developed a 5D flow[2] sequence: a free-breathing, radially sampled 3D velocity encoded acquisition with compressed-sensing reconstruction and retrospective cardiac and respiratory self-gating. We acquired 5D flow MRI in two pediatric cases with extracardiac total cavopulmonary connection (Fontan connection). Given the low-pressure environment of the connection, we expected respiratory driven flow to be prevalent and 4D flow's single respiratory state acquisition to be insufficient. The goal of this case study was to demonstrate the feasibility of 5D flow MRI to capture comparable measurements to 4D flow MRI and elucidate important respiratory driven flow changes in the Fontan circulation.

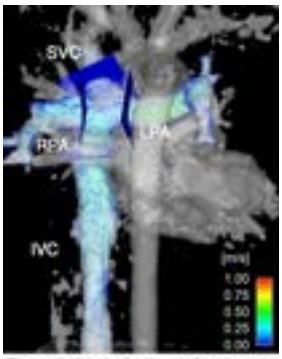

Figure 1. Analysis planes for case 1.

Methods: 5D flow was acquired in under 9 minutes in 2 patients with extracardiac Fontan connection (13yr male with ferumoxytol contrast and 12yr female with gadolinium contrast). A superior-inferior readout was used for cardiac and respiratory gating. The number of respiratory bins was manually set to 4 where the first respiratory state (RS1) represents end expiration and the last (RS4) represents end inspiration. 4D flow MRI with navigator gating at the end-expiration phase was also collected and used as the clinical reference standard. 4D flow was directly compared with RS1 due to their similar respiratory state. The Fontan connection was manually segmented for each respiratory state and for the 4D flow data sets. 2D analysis planes placed (fig 1) near the Fontan connection for each of the following: inferior and superior caval veins (IVC and SVC) and right and left pulmonary arteries (RPA and LPA). Net flow, flow conservation, and flow distribution to the LPA and RPA were measured for all 4 acquired 5D flow MRI respiratory states.

Results: In case 1, there was excellent agreement between 4D flow and 5D flow measurements (table 1) in the pulmonary arteries (<5% difference) and comparable net flow in the caval veins (22% difference in IVC and 38% difference in SVC). Flow conservation was within 10% of total inward flow for all respiratory states. There was a 11% increase in LPA flow and compensatory 10% decrease in RPA flow in end-inspiration compared to end-expiration which is most comparable to the 4D flow respiratory acquisition. Case 2 had significant aortopulmonary collaterals that caused blood to flow from the LPA to the RPA. Yet, with the exception of end inspiration, flow was well conserved (within 0.5% total inward flow) and net flow was comparable to 4D flow quantifications (table 2). The LPA, RPA and SVC had net flow within 6.5% of 4D flow measurements and the IVC had a -27% difference. Substantial changes were seen in particular in the caval veins in case 2. In the IVC, reverse flow nearly compensated for all forward flow in end inspiration.

Discussion: These two cases demonstrate that 5D flow measurements in pediatric patients are comparable to 4D flow measurements. The deviation in the IVC in both cases may be due to respiratory state definition differences or due to acquisition and reconstruction method differences between 5D and 4D flow. Additionally, there was excellent conservation of flow across all respiratory states. While the flow conservation appears to deviate in RS4 of case 2, this is likely due to increased veinous collateral flow beyond the Fontan connection. In spite of the cases having dramatically different flow patterns, changes in flow due to respiratory state were seen in both. In case 1, respiration drove the distribution of flow to the LPA and RPA toward an even 50/50 in end inspiration. In case 2, flow changed more substantially with respiration. In particular, 4D flow and RS1 5D flow found >10mL/cycle exiting the IVC into the Fontan connection while RS4 5D flow found less than 1mL/cycle net flow. This suggests respiration played a significant role in hemodynamics in this patient. We demonstrate rapidly accelerated 5D flow MRI captured respiration driven flow changes in pediatric Fontan patients and that respiratory resolved flow may be more important in some cases, such as case 2, than others.

Net Flow (mL/cycle)	4D Flow	RS1	RS2	RS3	RS4
IVC	24	29.4	24.9	27.5	28.9
SVC	12	7.5	8.2	7.9	6.1
RPA	18	18.5	18.3	16.6	16.7
LPA	15	15.5	15.7	16.2	17.3
RPA/LPA %	55/45	54/45	54/46	50/50	49/51
IN - OUT	3	2.87	-0.9	2.55	1.01

Table 1. Net flow quantifications for case 1.
RS1 – end expiration, RS4 – end inspiration.

Net Flow (mL/cycle)	4D Flow	RS1	RS2	RS3	RS4
IVC	14.0	10.2	12.4	7.1	0.8
SVC	17.6	16.7	12.3	13.1	9.3
RPA	56.1	55.9	53.9	49.0	43.8
LPA	-25.0	-26.6	-27.1	-30.5	-25.8
IN - OUT	0.5	-2.4	-2.1	1.7	-7.9

Table 2. Net flow quantifications for case 2.
RS1 – end expiration, RS4 – end inspiration.

References: 1. Jarvis et al. (2016). *Pediatric radiology*. 2. Ma et al. (2020). *Radiology: Cardiothoracic Imaging*.

Abstract ID: 19

Simultaneous Multi-contrast MRI for Carotid Plaque Assessment in One Sequence

Jiaqi Dou[1], Yajie Wang[1], Huiyu Qiao[1], Zhensen Chen[1], Yuze Li[1], Haikun Qi[2], Jie Sun[3], Dongxiang Xu[3], Xihai Zhao[1], Huijun Chen[1]

[1]Center for Biomedical Imaging Research, School of Medicine, Tsinghua University, Beijing, China, [2]School of Biomedical Engineering and Imaging Sciences, King's College London, United Kingdom, [3]Department of Radiology, University of Washington, Seattle WA, United States

Purpose: A technique named SIMPLE was proposed to achieve simultaneous T1 and T2 mapping of carotid plaque[1] with large coverage and 3D isotropic resolution in one scan. This study aimed to generate a set of co-registered 3D high-resolution T1w, T2w, and PDw images, and MR angiogram (MRA) based on SIMPLE. The performance of the generated images for carotid plaque assessment was compared with the conventional multi-contrast sequences.

Methods: Four different image contrasts were reconstructed using low-rank modeling and sparsity constraints (LRS)[2] reconstruction method with a time window width (TW) of 25. Real-value representation of images was adopted to enhance the contrast between blood and other tissues. **MRA:** Similar to SNAP[3], an optimal inversion time (TI) of 390 ms, at which the luminal signal was negative while the background tissues were positive, was applied to maximize the contrast between vessel wall and blood. MRA was generated by using spokes with T2-prep of 25 ms and taking absolute values of the negative signals. **T1w:** With T2-prep of 0, T1w images were generated at a chosen TI = 640 ms around the zero-crossing point of blood signal. **T2w:** Numerical simulation showed that short TI leads to fewer T1 relaxation effects, so this study adopted the minimum available TI of 140 ms. Spokes within the temporal window centered at the minimum TI and acquired with T2-prep of 50 ms were used for T2w images reconstruction. **PDw:** Assuming that the chosen TI is long enough for near-complete T1 relaxation, spokes at the end of the shots without T2-prep pulses were used to obtain PDw reconstruction. Then the blood signal was suppressed by subtracting the phase of the black-blood T1W image from the PDw image.

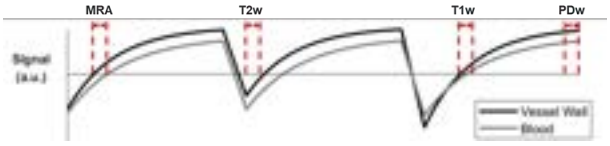

Fig 1. View sharing reconstruction of multi-contrast images

Results: Multi-contrast images were successfully generated from SIMPLE on all 5 subjects. Figure 2 demonstrated a carotid plaque with IPH, in which both SIMPLE-T1w and T1w-TSE images showed hyperintensity. Maximum intensity projection (MIP) of SIMPLE-MRA demonstrated clear depictions of bilateral carotid arteries. For LRNC, the SIMPLE dataset showed iso-intensity T1W and hypointensity T2W and agreed with conventional multi-contrast images (Figure 2). A calcified plaque (Figure 2) presented hypointensity on all contrasts except SIMPLE-T2w, which might due to the negative blood signal on the real SIMPLE-T2w image. SIMPLE-T1w images provided a clearer visualization of CA than T1w-TSE.

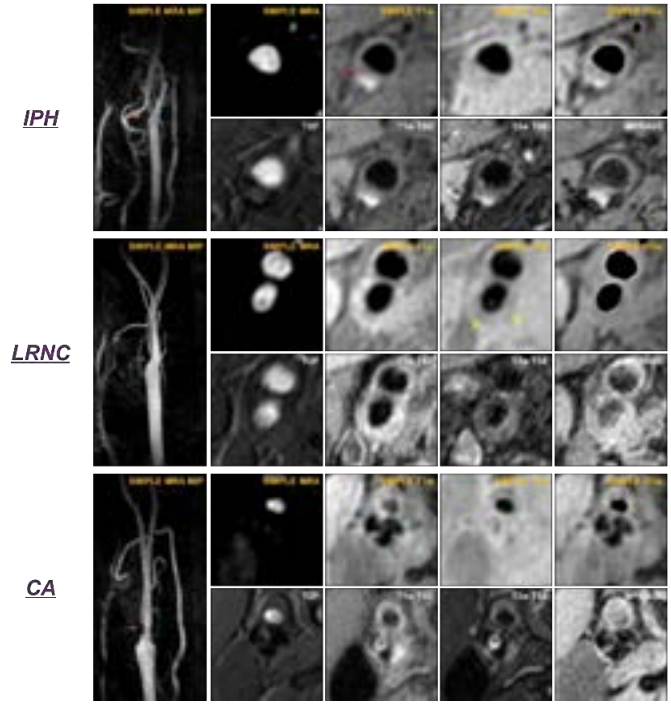

Fig 2. Multi-contrast reconstruction for carotid plaque assessment

Discussion: A set of naturally registered multi-contrast images, including MRA, T1w, T2w, and PDw images, were generated based on a single SIMPLE sequence, and the acquisition time was less than conventional protocol (8 min vs 16 min). The preliminary experiment showed a good agreement between the SIMPLE-generated images with the conventional ones for both lumen and vessel wall delineation and plaque components identification.

References

[1] Qi, H., et al. MRM, 2018. 80(6): p2598-2608. [2] Qi, H., et al. ISMRM, 2018. 248. [3] Wang, J., et al. MRM, 2013. 69(2): p337-345.

Abstract ID: 20

In-vivo Magnetic Resonance Histology of Peripheral Arterial Chronic Total Occlusions in Chronic Limb Threatening Ischemia Patients

Kavya Sinha[1], Christof Karmonik[2], Alan Lumsden[1], Trisha Roy[1]

[1]DeBakey Heart & Vascular Center, Houston Methodist Hospital, Houston Tx; [2]Translational Imaging Center, Houston Methodist Hospital, Houston Tx

Objectives

An “endovascular-first” strategy has been widely adopted for the treatment of peripheral artery disease (PAD) but is associated with high failure rates. Not all lesions are amenable to endovascular treatment, and it is currently not possible to predict this in advance with current imaging methods. While traditional MRI is not able to visualize calcium, Ultrashort echo time (UTE) sequences can not only image calcium but are also capable of characterizing the morphology, composition, and mechanical properties of plaques ex-vivo[1]. Our goal is to demonstrate the feasibility of using clinical 3 Tesla MRI scanners for histologic level PAD plaque characterization in-vivo, to aid endovascular patient selection and treatment planning.

Methods

Eleven patients with popliteal artery chronic total occlusions (CTOs) were scanned with a clinical contrast-enhanced CT angiogram (CTA). Patients were also imaged with “MR-histology (MRH)” using a 3T MRI scanner with non-contrast, flow independent sequences (Steady State Free Precession (SSFP) and Ultrashort Echo Time (UTE)) at high resolution (0.5 mm x 0.5 mm x 0.5 mm) for histologic level plaque characterization. Patients were imaged with an 18-channel knee coil and UTE images were acquired at an echo time (TE) of 70 microseconds. UTE and SSFP sequences have unique imaging signatures for various plaque components that were validated with ex-vivo histology and microCT.[1] Images were reviewed by a vascular surgeon and plaque components were identified on MR-histology images and CTA.

Results

MR-histology identified six distinct plaque components in-vivo: concentric calcium (6/9 patients – Fig 1), eccentric calcium (8/9), speckled calcium within dense collagen matrix (3/9), fibrotic dense collagen with minimal calcium (3/9 - Fig 2), thrombus (1/9 – Fig 1), and soft lesion components (4/9). CTA could not differentiate thrombus from dense collagen (Fig 1 and 2) and could not differentiate solid calcium nodules from speckled calcium in collagen matrix due to beam hardening artifacts.

Conclusions

MR-histology can be used to characterize peripheral artery plaque composition and morphology in-vivo. This imaging technique can guide endovascular patient selection and tailored wire and device selection according to plaque composition in the future.

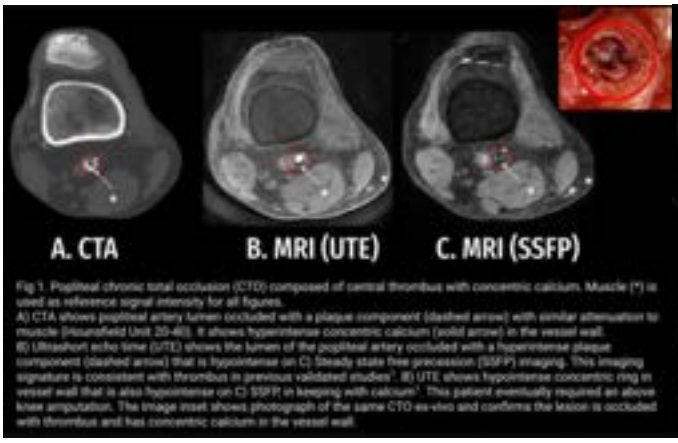

Figure 1

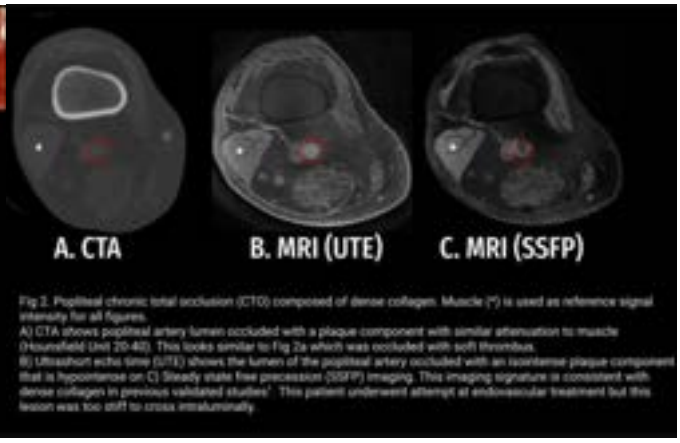

Figure 2

Reference

[1] Roy T, Liu G, Shaikh N, Dueck AD, Wright GA. Puncturing Plaques. J Endovasc Ther. 2017 Feb;24(1):35-46.doi: 10.1177/1526602816671135. Epub 2016 Sep 25.

Abstract ID: 21

Time-Average Wall Shear Stress in Normal subjects, Subjects with Atherosclerotic Lesions and Subjects with Carotid Webs

Retta El Sayed[1,2], Alireza Sharifi[2], Charlie C. Park[2], Diogo C., Haussen[3], Jason W. Allen[1,2], John N. Oshinski[1,2]

[1]*Department of Biomedical Engineering, Georgia Institute of Technology & Emory University, Atlanta, GA, USA*

[2]*Department of Radiology & Imaging Sciences Emory University, Atlanta, GA, USA.*

[3]*Department of Neurology, Emory University, Atlanta, GA*

Purpose: Carotid atherosclerosis is a leading cause of ischemic stroke and is characterized by inflammation, wall thickening, plaque build-up, stenosis, and thrombus formation. However, atherosclerosis is not the only cause of strokes as carotid webs (CaW) account for up to one-third of cryptogenic strokes in younger patients without vascular risk factors.[1] CaWs are intraluminal shelf-like projections in the ICA bulb, which cause local lumen narrowing of 20-50%, and can cause significant hemodynamic disturbance resulting in flow separation, recirculation, stagnation, and ultimately thrombus formation.[2,3] Understanding the hemodynamic alterations caused by CaWs is essential for determining the associated stroke risk. The purpose of this work is to compare time average wall shear stress (TAWSS) in a healthy subject, a subject with mild atherosclerosis, and a subject with CaW using MRI and computational fluid mechanics (CFD). *We hypothesized that CaWs will have a larger region of low time-averaged wall shear stress (TAWSS) than a healthy carotid or atherosclerotic carotid with a similar degree of luminal narrowing, indicating a larger recirculation/stagnation zone in the CaW.*

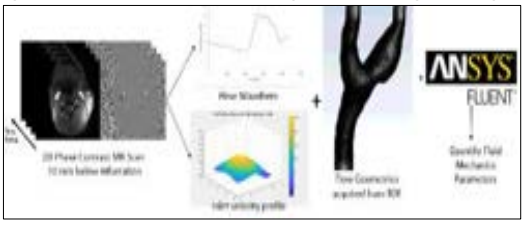

Figure 1. *Velocity waveform and profile from PC-MR data and Patient-specific geometry from TOF images were an input for Fluent CFD Simulation.*

Methods: Eight patients with 11 CaWs (6 female, age 50.9±10.4) with history of stroke or TIA were imaged on a 3T system (MAGNETOM Prismafit, Siemens Healthcare) as part of an IRB-approved study. Images from healthy volunteers and patients with mild atherosclerosis were acquired from another ongoing study. Multi-Slab, transverse, 3D time of flight (TOF) Images were acquired to cover the bifurcation (pixel=0.5x0.5x0.5mm^3, TR=23ms, TE=3.1ms). 2D, ECG-gated, cine phase contrast (PCMR) images were acquired 10mm below and 10mm above the bifurcation (pixel size=1x1x5mm^3, VENC=80cm/sec, TR=43.6, TE=7). CFD simulations were conducted in three cases based on TOF and PCMR images; one healthy subject, and one subject with mild atherosclerosis (24.5% stenosis) one subject with CaW (23.4% luminal narrowing)[1]. Mimics (Materialise, 2019) was used to segment the TOF images and create the smoothed 3D geometry. Fluent (ANSYS, 2021 R1) was used to mesh the geometry and conduct transient flow simulations based on 2D PCMR at the inlet and constant pressure at the outlet with the assumption of rigid wall and the no-slip condition. Outlet PCMR data was used for validation of our CFD method ***(Figure 1)***. TAWSS over the cardiac cycle was determined for each case. The vessel wall area where TAWSS values are two standard deviations below the mean were considered *low TAWSS regions* that indicated stagnation/ recirculation.

Results and conclusion: The total area of low TAWSS was calculated in the three cases and is presented graphically ***(Figure 2).*** In the healthy carotid bulb, low TAWSS was present in 5% of the model surface area, while it was present in 15% of the surface area in the atherosclerosis model, and 26% in the CaW model. These results show that the region of low TAWSS was 57.7% larger in the CaW than in the atherosclerotic model, indicating a larger regions of flow disturbance caused by CaW. *In conclusion*, CaW caused greater degree of flow disturbance characterized by low TAWSS compared to an atherosclerotic lesion with similar degree of luminal narrowing.

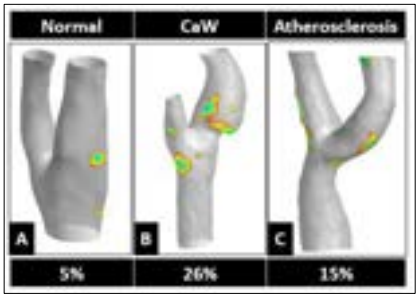

Figure 2. *Time average Wall Shear Stress results where A) healthy, B) CaW, C) Mild atherosclerosis.*

References: 1.Haussen DC, et al. *Stroke.* 2017;48(11):3134-3137. 2.Compagne KCJ, et al. *AJNR Am J Neuroradiol.* 2019;40(4):703-708. 3.Park CC, et al. The 59th Annual Meeting of the American Society of Neuroradiology. 2021.

Abstract ID: 22

Hemodynamic Difference between Borderzone Infarct and non-Borderzone Infarct in Patients with Middle Cerebral Artery Atherosclerosis

Wenwen Chen[1], Xiaowei Song[2], Shuo Chen[1], Zhensen Chen[1], Mingzhu Fu[1], Hanyu Wei[1], Jian Wu[2], Rui Li[1]

[1]Center for Biomedical Imaging Research, Department of Biomedical Engineering, School of Medicine, Tsinghua University, Beijing, China,

[2]Department of Neurology, Tsinghua Changgung Hospital, Beijing, China

Purpose: Borderzone infarct (BZI) tends to result in bad clinical course and poor diagnosis[1][2]. And the low flow hypothesis guessed that hemodynamic compromise was the possible pathogenic mechanism of BZI and many researches had verified this in severe stenosis[3]. However, the concrete hemodynamic difference between BZI and other infarct patterns still remains unclear. So this study aims to investigate whether there remains a significant hemodynamic difference between BZI and non-BZI in patients with middle cerebral artery atherosclerosis.

Methods: Patients with unilateral infarction in the MCA territory due to MCA atherosclerosis within two weeks of ischemic stroke onset were recruited. Patients were divided into BZI and non-BZI groups based on DWI. 4D flow imaging was performed. Bilaterally $Flow_{avg}$ of MCA-M1 segment were quantified. $Flow_{avg}$ between the infarct and contralateral sides were compared using paired sample t-test to verify hemodynamic lateralization. Demographic and clinical risk factors were compared between two groups using chi-square test. Intra-observer reproducibility was test using Bland-Altman plot. All statistical analysis was conducted in Medcalc software. Significant p value <0.05.

Results: The demographic and clinical risk factors were not significantly different between two groups. Intra-observer reproducibility is shown in Figure 1. In BZI, $Flow_{avg}$ is significantly lower than contralateral side as shown in Table 1.

Discussion: Border zone regions are supplied by distal end branches of non-anastomosing arteries, which are vulnerable to hemodynamic changes. BZI is more likely to have significant hemodynamic lateralization than non-BZI.

Table 1. Hemodynamic lateralization of the BZI (n=22) and non-BZI (n=15) groups.

$Flow_{avg}$ (ml/s)	Infarct side	Contralateral side	*P*
BZI	1.50±1.47	3.16±1.38	< 0.00010 *
non-BZI	2.08±1.35	2.52±0.98	0.12

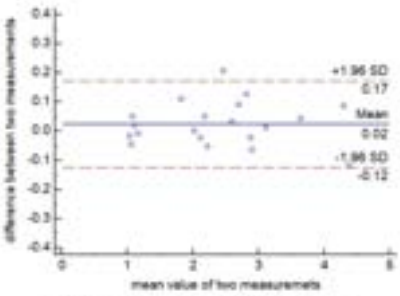

Figure 1. Bland-Altman plot for $Flow_{avg}$ measurements showing good reproducibility.

References

[1]. Yaghi, S., et al. Infarct Pattern, Perfusion Mismatch Thresholds, and Recurrent Cerebrovascular Events in Symptomatic Intracranial Stenosis. J Neuroimaging. 2019; 29(5): 640-644.

[2]. Raghuram, K., et al. Relationship between stroke recurrence, infarct pattern, and vascular distribution in patients with symptomatic intracranial stenosis. J Neurointerv Surg. 2018;10(12): 1161-1163.

[3]. Mangla, R., Kolar, B., Almast, J. & Ekholm, S. E. Border zone infarcts: pathophysiologic and imaging characteristics. Radiogr. 2011;31: 1201–1214.

Abstract ID: 23

Clinical and morphological characteristics predicting recurrent ischemic stroke after intensive medical management: A prospective analysis of intracranial atherosclerosis using high-resolution magnetic resonance imaging

Zhang Shi[1,2], Qi Liu[2], Jianping Lu[2]
[1] Department of Radiology, Zhongshan Hospital, Fudan University, Shanghai, China
[2] Department of Radiology, Changhai Hospital, Naval Medical University, Shanghai, China

Purpose: We aims to investigate the change of the clinical and imaging features during the intensive medical management and further evaluate the independent high-risk factors in predicting the recurrent cerebrovascular ischemic events in both short and long time of following up using high-resolution magnetic resonance imaging (hrMRI).
Methods: The patients with acute ischemic stroke were prospectively analyzed and imaged using 3D joint intra- and extracranial vessel wall imaging. And all of the patients underwent hrMRI after intensive medical management at 3 month intervals. The clinical characteristics including physical activity, the clinical symptom and blood testing associated with intracranial atherosclerotic disease (ICAD) were also followed. The evaluation on the recurrence of ischemic stroke was performed by telephone interview before March 1, 2021. Univariate and multivariate Cox regression analysis were used to calculate the hazard ratio (HR) and corresponding 95% confidence interval (95%CI) of the plaque features in discriminating between patients with and without recurrent events.
Results: Eighty patients (age, 59.64±12.03 years) were recruited in the final study. The mean time interval of short time follow-up was 92.4±15.9 days while the time interval of the long time follow-up were 583.4±130.8 days. After the intensive medical management, both the clinical features associated with ICAD (NIHSS, Total cholesterol, Triglyceride, LDL cholesterol and C-reactive protein) and the plaque activity (plaque with enhancement) had a significant decreasing (P<0.001). But the ratio of recurrence was still high (8.75% in 3 month intervals and 10% in 12 month interval). Univariable Cox regression was shown in Figure 1. Multivariable Cox regression indicated that plaque like gibbous moon (HR, 7.137; 95%CI，1.531-33.277；P =0.047) was a significant high-risk predictor for recurrent ischemic events in short time follow-up and the presence of physical activity or not (HR=0.104；95%CI，0.018-0.591；P =0.010) was significantly associated with recurrence during the long time follow-up.
Discussion: It is demonstrated in our previous study that hrMRI may predict the risk of recurrent stroke due to ICAD.[1] However, the 2D&non-whole brain scan and the lack of the clinical management on the patients' follow-up and the outcome evaluation were the significant limitation. We improved these limitations and our finding showed that hrMRI could provide visualization of the change on plaque features during the intensive medical management, and may help predicting the patients with ICAD at risk of recurrent stroke. Furthermore, the previous study[2] found that physical inactivity should be aggressively treated in patients with ICAD to prevent future vascular events, which was similar to our findings. It indicated that physical activity was a strong predictor of stroke recurrence in long time follow-up.

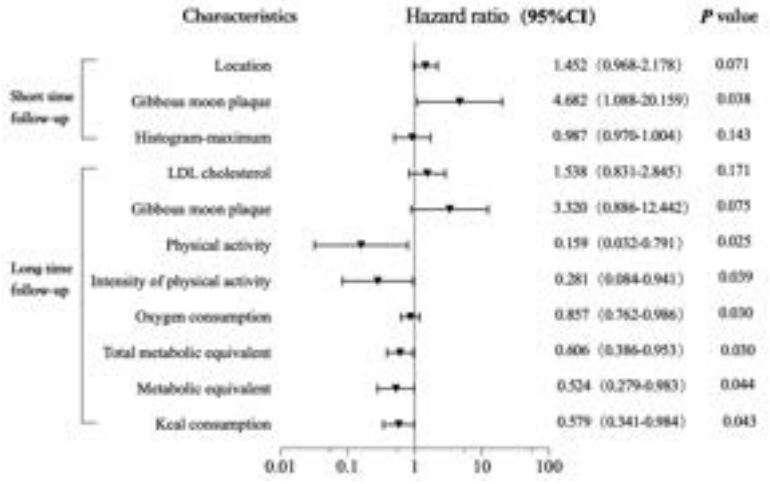

Figure 1 Univariable Cox regression of recurrent stroke in short time and long time follow-up with hazard ratio and 95% confidence interval.

References:

[1] Shi Z, et al. Progression of Plaque Burden of Intracranial Atherosclerotic Plaque Predicts Recurrent Stroke/Transient Ischemic Attack: A Pilot Follow-Up Study Using Higher-Resolution MRI. J Magn Reson Imaging. 2021 Feb 18.
[2] Turan TN, et al. Relationship between risk factor control and vascular events in the SAMMPRIS trial. Neurology. 2017 Jan 24;88(4):379-385.

Abstract ID: 24

Visualization of lenticulostriate arteries on intracranial VW-MRI: relationship between MCA atherosclerotic plaque and infarction types

Li Qian, Zhongda Hospital Affiliated to Southeast University

Objective Using vessel wall magnetic resonance imaging (VW-MRI) technique to investigate the relationship between the middle cerebral artery (MCA) plaque volume and the number and length of the lenticulostriate artery (LSA) in patients with different types of infarction. Methods Retrospective inclusion as performed on 58 patients with suspected cerebrovascular diseases had received head MRI examination, and all patients were definitively diagnosed by VW-MRI examination. Among them, 39 patients with unilateral acute cerebral infarction in basal ganglia region [28 males and 11 females, range 45-75 years old, average 60.92±12.21years], and 19 patients without unilateral MCA plaque and acute cerebral infarction were used as control group [8 males and 11 females, range 42-81 years old, average 63.84±12.05 years]. Clinical data of the 3 groups were collected by 2 radiologists and the length and number of the lenticulostriate arteries were measured. The plaque volume of MCA M1-2 segments in the LSI group and the SLI group were measured with plaque software. Comparison between 2 groups was conducted with Student's test, and comparison the 3 groups was conducted with One-way ANOVA or chi-square est. Multivariate logistic regression analysis was used to analyze the influencing factors of different types of infarction. Intraclass correlation coefficient (ICC) was used to check the repeatability of measurements between two radiologists. Results There were no statistical difference in the clinical data among the 3 groups(all P>0.05).The average branch length and number of LSA in LSI, LSI, and control group were 13.48±2.99 mm,15.8±2.71 mm,and16.4±2.69 mm, and 2.00±0.77,2.78±0.94, and 3.11±1.15, respectively, the differences were statistically significant(all P<0.05).The branch length and number were smallest in the LSI group(P<0.05),and they did not significantly differ between the SLI and control group(P>0.05).The plaque volume was higher in the LSI group than that in the SLI group (87.5±17.7) mm3、(75.5±9.4) mm3,t=2.579, P=0.014]. The shorter the length and the fewer number of LSA significantly increased the risk of SLI [OR=0.665, 95% confidence interval(CI): 0.497-0.890,P<0.05;OR =0.253,95% CI: 0.106-0.604,P <0.05,respectively).Plaque volume and length were consistent, with ICC values of 0.78 and 0.84.Conclusion VW-MRI imaging of MCA and LSA is helpful to reveal the mechanism of deep perforation infarction, and the plaque volume of MCA and the length and number of LSA are the key factors affecting the types of cerebral infarction.

Abstract ID: 25

Deep Learning Performs Flow Quantification of Cardiovascular 2D Phase Contrast MRI at Human Level

M Pradella[1], M B Scott[1], M Omer[2], L Lockhart[2], C Jensen[2], X Yi[2], A Amir-Khalili[2], A Sojoudi[2], B D Allen[1], R Avery[1], M Markl[1]

[1] Department of Radiology, Northwestern University, Chicago, USA
[2] Circle, Cardiovascular Imaging, Calgary, Canada

Purpose: 2D Phase Contrast (2D-PC) MRI allows for analysis of blood flow in many cardiovascular (CV) abnormities [1,2]. However, because of close anatomical relations between aorta, pulmonary artery (PA) and other vascular structures, accurate delineation of vessel contours is required [3,4]. In this study, we evaluated the performance of a Deep Learning (DL) application for fully automated contour delineation and flow quantification compared to manual analysis by a CV radiologist.

Methods: We included 97 consecutive patients (pts) who underwent 2D-PC imaging in November 2020. All pts received 2D-PC flow measurements at the sinotubular junction (STJ). In a subgroup (n=28), 2D-PC data was also collected for the main PA. All exams were performed on 1.5T MRI systems (Siemens, Germany).

A CV radiologist with 3 years of experience performed the manual analysis. The outer vessel contour was delineated on the first time point of the magnitude image, forwarded and adjusted for each time point (Fig 1, red contours). The DL application (Circle Cardiovascular Imaging, Canada) autonomously identified the scan location (STJ or PA) and performed automated vessel contour detection across all cardiac time points (Fig 1, yellow contours). STJ and PA net flow was calculated for both DL and manual analysis. Manual and DL contours were compared using mean dice scores (DSC). Spearman correlation and Bland Altman plots were generated to compare DL with manual performance. A measurement difference of <10% between DL and manually measured net flow was considered as excellent agreement.

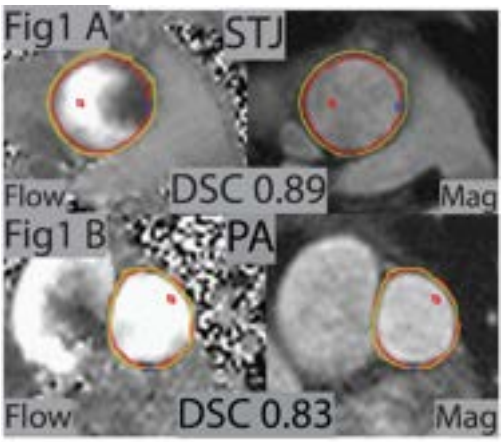

Results: In total, 125 manual 2D-PC MRI measurements (STJ: 97, PA: 28) were performed with a median of 20 cardiac time points (range: 20-30). Mean manual measurement times were 3:00±0:52min at STJ and 2:47±0:42min at PA.

DL performed 121/125 measurements (overall accuracy 97%; STJ: 95/97 (recall 98%, precision 99%), PA: 26/28 (recall 93%, precision 100%)). Mean DL analysis time was 1s/case.

Mean DL vs human DSC at STJ was 0.91 (interquartile range (IQR): 0.03), and 0.83 (IQR: 0.08) at PA (Fig 1). In one case, DL did not correctly contour the STJ in all time points causing an outlier (Fig 2A, B). However, Spearman correlation was still high with 0.98 for both STJ ($p<0.001$) and PA ($p<0.001$) (Fig 2A, 3A). Bland Altman plots showed DL vs human mean differences for net flow of 0.89ml (limits of agreement (LoA): -13.23 – 15.02ml) for STJ and 1.8ml (LoA: -7.21 – 10.8ml) for PA (Fig 2B, 3B). Overall, in 104/121 processed series the measurement difference for net flow was < 10% (86%).

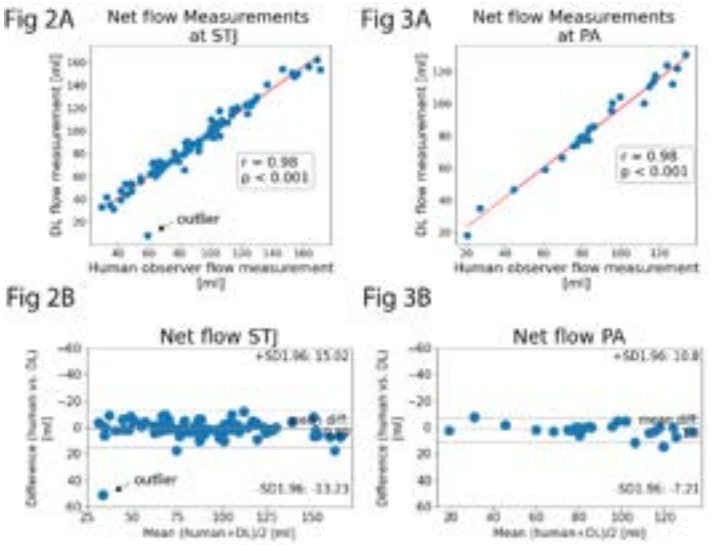

Conclusion: The evaluated, fully automated DL application provided equivalent flow quantification at STJ and PA compared to an experienced human observer in 86% of analyzed series while analysis times were significantly reduced. This represents excellent agreement and suggests that the DL application can be utilized as a useful tool in daily radiology practice.

References: [1] Wymer *Radiographics* 2020, [2] Markl *Clin Radiol*. 2016, [3] van der Geest *Int J Cardiovasc Imaging* 1997, [4] Nayak J Cardio Mag Res 2015

Abstract ID: 26

Plaque location distribution in patients with intracranial atherosclerotic plaques with fetal posterior cerebral artery

Dingqi Liu [1]，Cheng Li [2]

[1,2]Department of Radiology, Zhongda Hospital, Medical School of Southeast University，Nanjing，China

Purpose: To investigate the distribution characteristics of intracranial atherosclerotic plaque in patients with FTP.

Methods: We retrospectively analyzed the imaging and clinical data of 42 patients with Intracranial atherosclerotic plaque. On high-resolution MRI, plaques were found in the ACAs，MCAs，PCAs and VBAs.The relationship between FTP and plaque distribution was analyzed.

Results:A total of 42 plaques (15 observation group and 26 control group) on 194 image slices were studied. Overall, of the 42 slices with identified plaques, plaques were more frequently located at the MCAs (38.1%)and PCAs (42.9%) as compared with the ACAs(7.14%) and the VBAs (7.14％). Observation group had more MCA plaques (P=0.011) and less PCA plaques (P=0.024) than control group. Plaques in the ACAs and the VBAs had no statistical significance due to the small sample size.

Discussion: Patients with intracranial atherosclerotic plaques with FTP are more likely to have MCA plaques than those without FTP.

Variate	ACA	MCA	PCA	VBA
observation group	2（4.76%）	10（23.8%）	3（7.14%）	1（2.38%）
control group	1（2.38%）	6（14.3%）	15（35.7%）	2（4.76%）
P	/	0.011	0.024	/

References:

[1] De Silva K R D, Silva T R N, Gunasekera W S L, et al. Variation in the origin of the posterior cerebral artery in adult Sri Lankans.[J]. Neurology India, 2009,57(1).

[2] Hashemi S M, Mahmoodi R, Amirjamshidi A. Variations in the Anatomy of the Willis' circle: A 3-year cross-sectional study from Iran (2006-2009). Are the distributions of variations of circle of Willis different in different populations? Result of an anatomical study and review of literature[J]. Surg Neurol Int, 2013,4:65.

[3] Saeki N, Rhoton A L. Microsurgical anatomy of the upper basilar artery and the posterior circle of Willis.[J]. Journal of neurosurgery, 1977,46(5).

[4] van Raamt A F, Mali W P T M, van Laar P J, et al. The Fetal Variant of the Circle of Willis and Its Influence on the Cerebral Collateral Circulation[J]. Cerebrovascular Diseases, 2006,22(4).

Abstract ID: 27

Myocardial T1 Mapping using Semi-supervised Deep Learning Motion Correction Method

Chunyan Wu[1], Yuze Li[1], Haiyan Ding[1], Huijun Chen[1]

[1]Center for Biomedical Imaging Research, Department of Biomedical Engineering, School of Medicine, Tsinghua University, Beijing, China

Purpose: Recently, myocardial T1 mapping has been widely concerned for its potential in the clinical diagnosis of various cardiomyopathies [1]. However, for T1 mapping, the unregistered of different image frames caused by heart and respiratory movement will reduce the accuracy of T1 quantization [2]. In this study, we have proposed a semi-supervised deep learning motion correction method for myocardial T1 mapping on STONE [3] sequence.

Method: Figure 1 demonstrates the registration framework. The proposed method applied UNET to estimate the dense registration field *u*, which is modeled as $u = g_\theta(f, m)$. The network g_θ takes the fixed image *f* (last frame of T1 weighted images), moving image *m* (other frames of T1 weight images) as well as myocardial mask of fixed image and moving image as input, and then outputted the estimated registration field *u*. Then, *u* was applied on the moving image using the spatial transformation [4] to generate the registered image and made loss. After the network was trained, each moving image was registered and then the pixel-wise T1 fitting was performed to generate the myocardial T1 map. Because the training of the network did not require the ground-truth of the registered image but required the segmentation as the auxiliary information, the method can be regarded as semi-supervised. The loss function is: $\mathcal{L}_{semi}(f, m, u) = \mathcal{L}_{sim}(f, m') + \mathcal{L}_{smooth}(u) - DSC(M_f, M_{m'})$. where the first term denotes the similarity of fixed image and registered image, the second term denotes the smooth constraint on the registration field [ref], and the third term denotes the segmentation loss. The proposed method was compared with a conventional method FFD [5], self-supervised method (no segmentation loss) with different similarity matrix (Cross Correlation, CC) and MI (Mutual information, MI). The training and testing was performed on a public dataset [6].

Figure 1

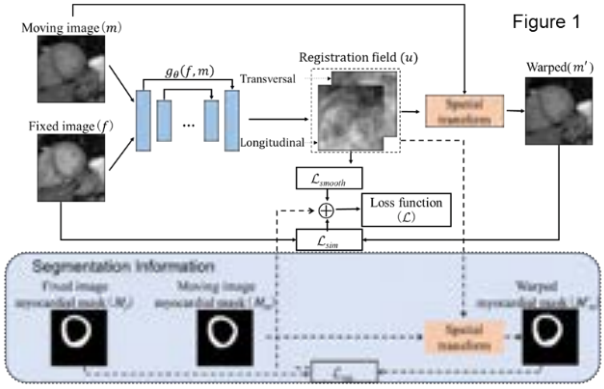

Table 1. Quantitative Results on Different Methods

	DSC	MBE(mm)	Myo_SD(mm)
Original	0.662±0.136	2.270±1.465	112.68±37.54
FFD	0.790±0.047	0.727±0.257	77.91±21.53
Self-supvised_CC	0.797±0.037	0.677±0.227	71.30±19.10
Self-supvised_MI	0.795±0.041	0.730±0.287	72.62±19.87
Semi-supvised_CC	**0.843±0.037**	0.567±0.140	**67.67±16.51**
Semi-supvised_MI	0.832±0.030	**0.564±0.184**	68.20±18.27

DSC: Dice Similarity Coefficient; MBE: Mean Boundary Error; Myo_SD: Myocardial T1 Mapping Standard Deviation. Bold and underline indicates the best results.

Results: Table 1 shows the quantitative results and Figure 2 shows the T1 mapping results. The semi-supervised method using CC can achieve the best DSC and Myo_SD results while the method using MI can achieve the best MBE result. The semi-supervised method behaved better than FFD and self-supervised method.

Discussion: The results show the proposed can obtain more accurate registration performance on T1-weighted images, and reduce the error of T1 quantification, which proves the feasibility and effectiveness of the proposed algorithm.

Figure 2

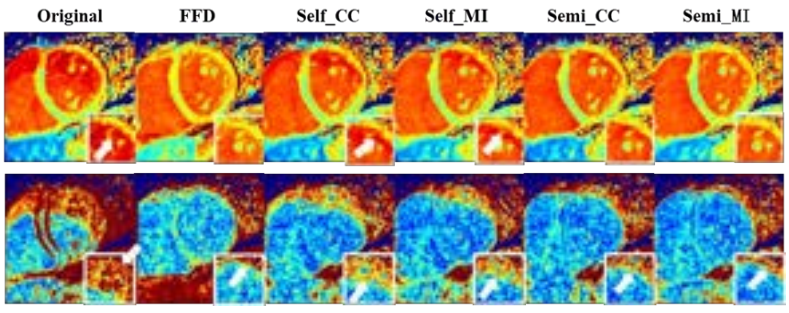

1.Sechtem, et al. AJR. 1987.
2.Messroghli, et al. MRM. 2004.
3.Sebastian, et al. MRM. 2014.
4.Balakrishnan, et al. TMI. 2019.
5.Rueckert, et al. TMI. 1999.
6.Rewaidy, et al. MRM. 2018.

Abstract ID: 28

Free-breathing 3D whole-heart joint T1/T2 quantification with isotropic resolution: preliminary clinical evaluation

C. Velasco[1], A. Hua[1], G. Milotta[1], K. P. Kunze[1,2], R. Neji[1,2], T.F. Ismail[1], C. Prieto[1], R. M. Botnar[1].
[1]School of Biomedical Engineering and Imaging Sciences, King's College London, London, UK
[2]MR Research Collaborations, Siemens Healthcare Limited, Frimley, UK

Purpose: Myocardial tissue characterization via T_1 and T_2 mapping plays an important role in the evaluation of many myocardial diseases[1]. T_1 and T_2 maps are typically acquired sequentially in 2D under several breath-holds[2]. However, they achieve limited spatial resolution and coverage. To overcome these limitations, a free-breathing high resolution, motion compensated joint T_1/T_2 water/fat prototype sequence has been recently proposed and validated in phantom and healthy subjects[3]. Here, we demonstrate the potential of the proposed approach to obtain whole-heart, motion-compensated, simultaneous, and co-registered T_1, T_2 maps and water and fat images in ~9 min in patients with cardiovascular disease.

Methods: The joint T_1/T_2 framework[3] consists of four interleaved, ECG-triggered spoiled gradient-echo volumes with 2-point bipolar Dixon encoding acquired with a 4x undersampled Variable Density Cartesian trajectory[4]. The first and fourth volume were preceded by an inversion recovery (TI = 120ms) pulse and a T_2 preparation pulse (T_2pTE = 50ms) respectively, whereas no magnetization preparation pulses were applied prior to the second and third volume. Nonrigid motion corrected reconstruction was applied to each in- and out-of-phase volume, employing multi-contrast patch-based higher-order low-rank regularization[5]. A water-fat separation algorithm[6] was then applied, and water image signal evolution across the four volumes was obtained voxel-wise. A patient specific dictionary of pre-calculated T_1/T_2 combinations was simulated using EPG[7] and matched against the measured water image signal evolution.

Ten patients with suspected cardiovascular disease (5 females, 53 ± 13 years) were scanned on a 1.5T scanner (MAGNETOM Aera, Siemens Healthcare, Erlangen Germany). Acquisition parameters included FA=8°, 2 mm^3 isotropic resolution, subject specific mid-diastolic trigger-delay and acquisition window of ~100ms, TR = 6.67ms, TE_1/TE_2=2.38/4.76ms, total scan time=~9min. Multi-slice pre- and post-contrast T_1-MOLLI and T_2-bSSFP maps, as well as Late Gadolinium Enhanced (LGE) images were acquired in a short axis (SA) orientation at the apical, mid-cavity and basal levels for comparison and as part of the clinical routine.

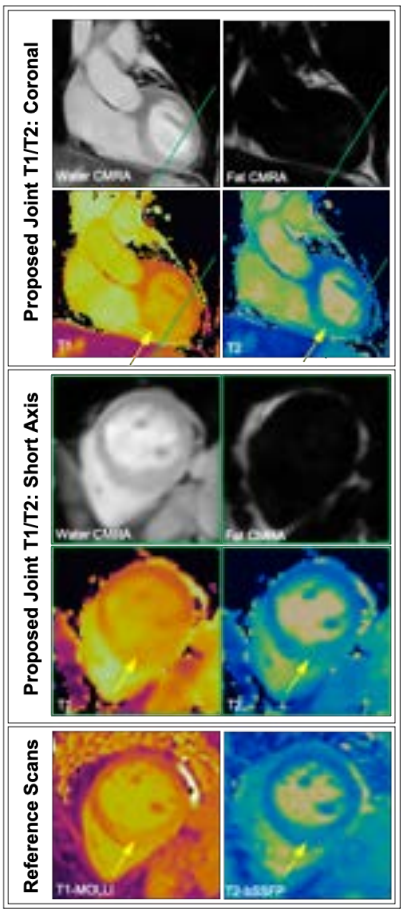

Fig 1. *Proposed joint 3D T_1, T_2, water CMRA and fat maps in coronal (top) and SA (middle) orientations for a representative patient with myocarditis. Bottom row shows reference scans. Yellow arrows point to a region of abnormally elevated T1 and T2.*

Results: 3D volumes of joint T_1/T_2 maps, as well as water and fat CMRA volumes were obtained for each subject and image quality of T_1 and T_2 maps was compared against multi-slice reference maps. Fig. 1 shows a representative slice from one subject (P02) with an inflammatory disorder in coronal and SA orientations, as well as the corresponding clinical reference scans. Fig. 2 shows a quantitative comparison of T_1 and T_2 values measured within an ROI manually drawn inside the septum of each subject. Further quantitative analyses were performed on a multi-slice level and compared against the clinical reference maps.

Discussion: We demonstrate the feasibility of the proposed free-breathing, accelerated motion corrected 3D joint T_1/T_2 prototype sequence, that allows the acquisition of isotropic resolution T_1 and T_2 maps and complementary co-registered water and fat volumes in a total scan time of ~9 min enabling assessment of regional abnormalities in T_1 and T_2 maps in patients with cardiovascular disease.

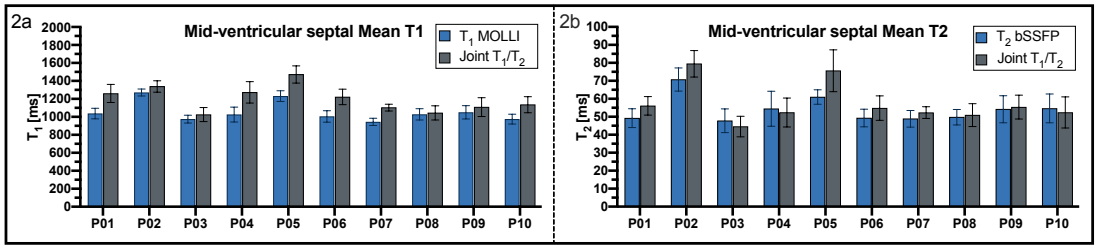

Fig 2. *Subject-by-subject quantification of proposed joint T_1/T_2 sequence compared to their respective clinical reference scans. Average T_1 (2a) and T_2 (2b) values obtained from proposed sequence (grey bars) are compared against its clinical reference (T_1-MOLLI and T_2-bSSFP respectively). Error bars show SD of each individual measurement. ROIs were drawn inside one SA slice at septal mid-ventricular level.*

References: [1]Kim, P.K. et al., Korean J. Radiol. 2017. [2]Messroghli, D.R. et al., JCMR 2017. [3]Milotta, G. et al., MRM 2020. [4]Prieto C. et al., JMRI 2015. [5]Bustin A. et al., MRM 2019. [6]Liu J. et al., MRM 2016. [7]Weigel M., JMRI 2015.

Abstract ID: 29

Low Rank Motion Correction for free-breathing first pass MR myocardial perfusion imaging

G. Cruz, A. Hua, C. Munoz, T.F. Ismail, R. M. Botnar, C. Prieto
[1]School of Biomedical Engineering and Imaging Sciences, King's College London, London, United Kingdom

PURPOSE: Magnetic resonance myocardial perfusion imaging is a challenging application ideally requiring free-breathing acquisitions, with both high spatial and temporal resolution. A novel Low Rank Motion Corrected (LRMC) reconstruction is proposed to enable highly accelerated motion corrected free-breathing MR myocardial perfusion imaging with superior image quality relative to iterative SENSE and Low Rank plus Sparse (L+S) reconstructions.

INTRODUCTION: MR first pass myocardial perfusion imaging has a challenging acquisition process, often requiring free-breathing and high acceleration factors. Approaches like k-t SLR[1], MASTeR[2] and L+S[3] have been developed to cope with the high undersampling factors by leveraging the temporally redundant information (via low rank and/or sparse terms) or by incorporating knowledge of the motion into regularization. Here we combine ideas from subspace constrained[4,5,6] with motion corrected[7,8,9] reconstructions to develop Low Rank Motion Correction (LRMC), a generalized (non-rigid) motion correction reconstruction operating in the perfusion signal subspace, enabling both respiratory motion correction and reduction of aliasing artefacts.

METHODS: The proposed LRMC reconstruction requires knowledge of signal subspace and respiratory motion. To this end, an auxiliary iterative SENSE (itSENSE)[10] reconstruction is performed initially; from these images the signal subspace can be derived via Singular Value decomposition of the corresponding Casorati matrix, whereas the motion can be derived via image registration (Fig.1). Thereafter, LRMC is performed by solving the following problem:

$$\hat{\boldsymbol{y}}, \hat{\boldsymbol{\mathcal{T}}}_{\boldsymbol{b}} = \underset{\boldsymbol{y}, \boldsymbol{\mathcal{T}}_{\boldsymbol{b}}}{\boldsymbol{argmin}} \ \frac{1}{2}\|\sum_{\boldsymbol{n}} \boldsymbol{A_n F C M_n U_r y} - \boldsymbol{k}\|_2^2 + \boldsymbol{\lambda} \sum_{\boldsymbol{b}} \|\boldsymbol{\mathcal{T}_b}\|_*$$

where $\boldsymbol{A_n}$ is the corresponding sampling trajectory for the *n-th* temporal frame, **F** is the Fourier transform, **C** are coil sensitivities, $\boldsymbol{M_n}$ are the motion fields, $\boldsymbol{y}$ are singular value images, $\boldsymbol{U_r}$ is the low rank compression (obtained by truncation of the left singular vectors to rank *r*), $\boldsymbol{k}$ is the acquired k-space data and $\boldsymbol{T_b}$ is a high dimensionality patch-based regularizer, HD-PROST.[11] Five patients referred for a clinical cardiac MR scan were scanned on a 3T scanner (Philips Achieva), using FOV = 256x256 mm^2; 10 mm slice thickness; in-plane resolution = 2x2 mm^2; TE/TR = 1.6/3.5 ms; radial golden angle; 3 slices (in 3 cardiac phases); flip angle 15º; WET saturation pulse; 100 ms saturation delay; nominal scan time ~60s. Data was reconstructed with itSENSE, L+S and with the proposed LRMC.

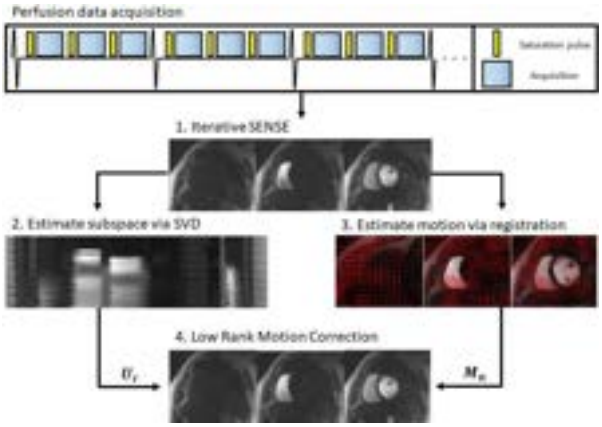

Fig.1 Diagram of the proposed LRMC approach, that requires motion and signal subspace estimation from auxiliary itSENSE images.

RESULTS: Perfusion frames from a representative patient demonstrate considerably improved image quality with the proposed LRMC approach compared to itSENSE and L+S (Fig.2). Substantial streaking artefacts, blurring and noise amplification is present with conventional itSENSE in addition to blurring from respiratory motion. This is also observed with L+S. Inspecting the dashed lines in Fig.2 it can be seen that with LRMC all frames are motion corrected to a common motion state, unlike itSENSE and L+S.

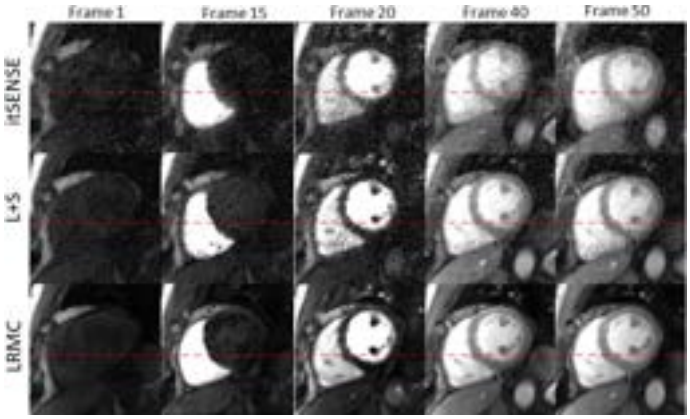

Fig.2 Myocardial perfusion in one representative patient for itSENSE, L+S and the proposed LRMC.

DISCUSSION: LRMC enables highly accelerated, free-breathing MR myocardial perfusion imaging with superior image quality compared with conventional techniques. This approach should improve perfusion quantification which requires motion compensation to facilitate accurate segmentation. Clinical utility will be evaluated in future larger patient cohorts.

REFERENCES:[1]Lingala et al. IEEE TMI 2011; [2]Asif et al. MRM 2013; [3]Otazo et al. MRM 2015; [4]McGivney et al. IEEE TMI 2014; [5]Zhao et al. MRM 2018; [6]Asslander et al. MRM 2018; [7]Batchelor et al. MRM 2005; [8]Odille et al. MRM 2008; [9]Cruz et al. MRM 2017; [10]Pruessman et al, MRM 2001; [11]Bustin et al. MRM 2019.

Abstract ID: 30

Associations between carotid plaque characteristics and perioperative cerebral blood flow determined by arterial spin labeling imaging in patients with moderate-to-severe stenosis undergoing carotid endarterectomy

Ran Huo[1], Ying Liu[1], Huimin Xu[1], Zheng Wang[1], Guangjin Zhou[1], Tao Wang[2], Huishu Yuan[1], Xihai Zhao[3]

1. Department of Radiology, Peking University Third Hospital, Beijing, China; 2. Department of Neurosurgery, Peking University Third Hospital, Beijing, China; 3. Department of Biomedical Engineering, Tsinghua University, Beijing, China

Purpose: Cerebral blood flow (CBF), one of the major physiological parameters of cerebral perfusion, usually changes before clinical symptoms [1]. Arterial spin labeling (ASL) MR imaging permits noninvasive quantification of blood flow by using the protons of arterial blood water molecules as endogenous diffusible tracers [2]. The aim of the present study was **to examine the associations between carotid plaque characteristics and perioperative CBF by ASL imaging**.

Methods: Patients with unilateral carotid moderate-to-severe stenosis referred for carotid endarterectomy (CEA) were recruited and underwent carotid vessel wall and brain ASL magnetic resonance imaging. The relative CBF (rCBF = $CBF_{index\text{-}hemisphere}/CBF_{contralateral\text{-}hemisphere}$) in middle cerebral artery territory were measured. Presence of carotid lipid-rich necrotic core, intraplaque hemorrhage (IPH), calcification, ulcer and fibrous-cap-rupture were identified. The volume and maximum area percentage of plaque components were measured. Plaque burden including area for lumen, wall, and vessel, maximum wall thickness, normalized wall index and vessel stenosis were measured. The associations between plaque characteristics and perioperative CBF were analyzed.

Results: Sixty-one patients (66.6 ± 7.8 years old; 55 males) were included. Univariate linear regression showed that $rCBF_{pre\text{-}CEA}$ was associated with stenosis (β -0.462; 95% CI -0.797 to -0.126; $P = 0.008$) and presence of calcification (β 0.103; 95% CI 0.005 to 0.201; $P = 0.040$), and $rCBF_{post\text{-}CEA}$ was associated with volume (β -0.060; 95%CI -0.107 to -0.014; $P = 0.013$) and maximum area percentage (β -0.127; 95% CI -0.223 to -0.030; $P = 0.012$) of IPH, respectively. After adjusting for confounding factors, most of above associations remained statistically significant (calcification vs. $rCBF_{pre\text{-}CEA}$: β 0.099; 95%CI 0.004 to -0.194; $P = 0.042$; IPH volume vs. $rCBF_{post\text{-}CEA}$: β -0.060; 95% CI -0.109 to -0.011; $P = 0.020$), while the association between maximum area percentage of IPH and $rCBF_{pre\text{-}CEA}$ was attenuated (β -0.089; 95% CI -0.188 to 0.011; $P = 0.080$).

Discussion and conclusions: Compositional characteristics of carotid atherosclerotic plaques are associated with perioperative CBF in patients with unilateral carotid moderate-to-severe stenosis undergoing CEA.

Table 1 Multivariate linear regression analysis between plaque characteristics and CBF (n = 61)

	*$rCBF_{pre\text{-}CEA}$			**$rCBF_{post\text{-}CEA}$		
	β	95% CI	*P*	β	95% CI	*P*
Morphology						
Mean lumen area, mm^2	-0.001	-0.005, 0.003	0.548	-0.002	-0.005, 0.001	0.300
Mean wall area, mm^2	-0.0004	-0.003, 0.002	0.725	-0.0009	-0.003, 0.001	0.311
Mean total vessel area, mm^2	-0.0004	-0.002, 0.001	0.607	-0.0008	-0.002, 0.001	0.236
Max WT, mm	-0.003	-0.024, 0.018	0.797	-0.011	-0.028, 0.006	0.193
Mean NWI, %	0.002	-0.003, 0.007	0.373	0.002	-0.003, 0.006	0.415
Presence of plaque components						
LRNC	0.008	-0.111, 0.128	0.888	0.022	-0.077, 0.121	0.659
IPH	-0.022	-0.109, 0.064	0.606	0.051	-0.020, 0.121	0.154
Calcification	0.099	0.004, 0.194	0.042	-0.055	-0.139, 0.030	0.200
Ulcer	0.054	-0.017, 0.146	0.238	-0.012	-0.089, 0.065	0.740
FCR	0.016	-0.065, 0.098	0.689	0.033	-0.034, 0.100	0.327
Volume of plaque components†‡						
LRNC, mm^3	-0.026	-0.070, 0.019	0.260	-0.024	-0.060, 0.011	0.174
IPH, mm^3	-0.038	-0.099, 0.023	0.213	-0.060	-0.109, -0.011	0.020
Calcification, mm^3	0.022	-0.019, 0.062	0.285	-0.007	-0.037, 0.022	0.618
Maximum area percentage of plaque components†‡						
LRNC, %	-0.017	-0.076, 0.042	0.559	0.002	-0.044, 0.048	0.933
IPH, %	-0.089	-0.188, 0.011	0.080	0.040	-0.130, 0.051	0.371
Calcification, %	0.026	-0.018, 0.071	0.233	0.011	-0.021, 0.043	0.497

*: adjusted for age, gender, index-stenosis and DBP; **: adjusted for age, gender, index-stenosis and TG; †Only patients with the corresponding component present were included in the comparison. ‡The increment of these continuous variables was 1 standard deviation. Max WT: maximum wall thickness; NWI: normalized wall index; LRNC: lipid-rich necrotic core; IPH: intraplaque hemorrhage; and FCR: fibrous cap rupture

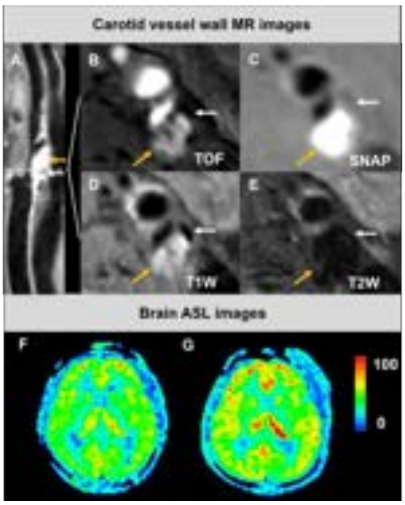

Fig. 1 The images from a 85 years old male patients who had carotid atherosclerotic plaque with IPH and calcification in the left side and changed CBF undergoing CEA.

References:

[1] Straka M, *et al*. J Magn Reson Imaging 2010; 32(5): 1024-37.

[2] Alsop DC, *et al*. Magn. Reson. Med. 73 (1) (2015) 102-16.

Abstract ID: 31

Magnetic Resonance Imaging of Aortitis

Shivam Kaushik, BS; Arzu Canan, MD; Liisa L. Bergmann, MD, MBA

Purpose: Aortitis is inflammation of the aortic wall, most often the media. It presents with nonspecific clinical symptoms with resultant challenges in diagnosis.[1,2] Aortitis is typically noninfectious in etiology, e.g. Takayasu's arteritis, however multiple infectious causes are also known.[2] Although biopsy remains the diagnostic gold standard, imaging is crucial in diagnosis, monitoring and treatment guidance, while eliminating the risks of bleeding and infection associated with tissue sampling.[1] Magnetic resonance imaging (MRI) and angiography (MRA) provides visualization of aortic wall and lumen without ionizing radiation exposure.[1] We discuss relevant MRI sequences and findings in patients with aortitis in the context of a clinical case.

Case: A 43-year-old female presented with chest pain. Past medical history was significant for positive reactive plasma reagin (RPR). Coronary computed tomographic angiography (CCTA) showed no intraluminal plaque however there was periaortic soft tissue and wall thickening of the ascending aorta resulting in extrinsic compression of the left main coronary artery. Subsequent MRA showed diffuse increased signal intensity within the aortic wall and periaortic soft tissue on fat suppressed T2-weighted imaging (T2WI). Additionally, focal mild narrowing at the origin of the left subclavian artery was detected. Concern for tertiary syphilis with aortitis prompted lumbar puncture however cerebrospinal fluid analysis was negative for neurosyphilis. Takayasu's arteritis was presumptively diagnosed given the patient's age, gender, and involvement of both the ascending aorta and left subclavian artery. Steroid treatment was initiated.

Findings: MRI findings suggestive of aortic inflammation include thickening and enhancement of the aortic wall, stenosis, mural wall thrombi, periaortic fluid or soft tissue accumulation and pericardial effusion.[1,2] High signal intensity in T2WI is consistent with mural edema, so long as the signal intensity is maintained even with fat saturation.[2] Black blood and bright blood imaging may also be considered. If left untreated, aneurysmal dilation of the aorta, pseudoaneurysms or aortic valve disease can develop.[2] MRA (without and with IV contrast) or 4-D flow can provide hemodynamic evaluation of the aorta.[3]

Conclusion: Clinical presentation of aortitis is nonspecific and diagnosis can be challenging. MRI is the method of choice for evaluation of aortitis due to excellent soft tissue contrast. T2WI with or without fat saturation is crucial in diagnosing acute mural inflammation. MRA with or without intravenous contrast reveals luminal narrowing or other intraluminal processes.[4] Future considerations include MRA with ferumoxytol intravenous contrast, known to be safe in patients who are pregnant or who have chronic renal disease; 4D flow to show turbulent blood flow path lines and wall shear stress; and PET-MRI to show avidity for FDG or other more specific radiolabels, yet to be developed.

References

1. Litmanovich DE, Yildirim A, Bankier AA. Insights into imaging of aortitis. *Insights Imaging*. 2012;3:545-560.
2. Restrepo CS, Ocazionez D, Suri R, Vargas D. Aortitis: Imaging Spectrum of the Infectious and Inflammatory Conditions of the Aorta. *RadioGraphics*. 2011;31(2):435-451.
3. American College of Radiology. ACR Appropriateness Criteria: Nontraumatic Aortic Disease. Revised 2020.
4. François CJ, Tuite D, Deshpande V, Jerecic R, Weale P, Carr JC. Unenhanced MR Angiography of the Thoracic Aorta: Initial Clinical Evaluation. *Am J Roentgenol*. 2008;190(4):902-906.

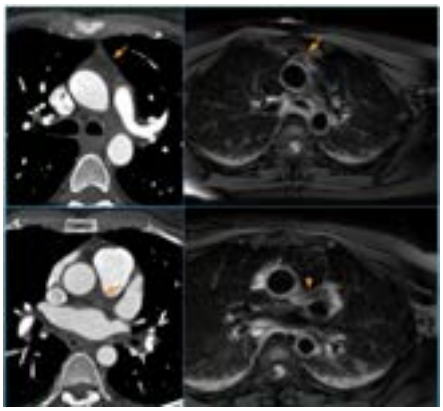

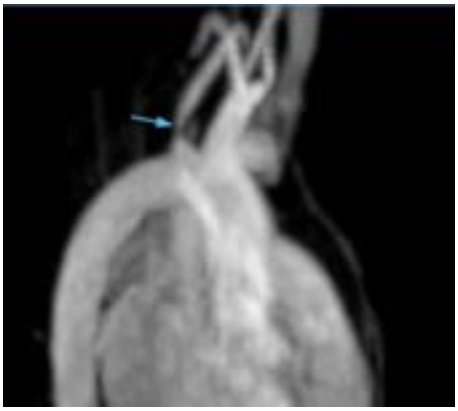

Abstract ID: 32

Non-ECG, free-breathing cine T1/T2/T2*/fat-fraction mapping for comprehensive myocardial tissue characterization with MR multitasking

Tianle Cao[1,2], Nan Wang[1], Hsu-Lei Lee[1], Xianglun Mao[1], Yibin Xie[1], Pei Han[1,2], Anthony G. Christodoulou[1,2], Debiao Li[1,2]

[1]Biomedical Imaging Research Institute, Cedars-Sinai Medical Center, Los Angeles, CA, USA
[2]Department of Bioengineering, University of California, Los Angeles, CA, USA

Purpose: Parametric mapping of myocardial T1, T2, and T2* can identify fibrosis, edema, and iron overload[1-3]; fat fraction (FF) is associated with heart failure[4] and nonischemic cardiomyopathies; and cine imaging is the gold standard for assessing cardiac function. A protocol combing all five assessments is clinically desirable but typically requires multiple breath-holds, resulting in long scan time, potential image misregistration, and patient fatigue. Recently we introduced MR multitasking for non-ECG, free-breathing, simultaneous T1/T2 mapping[5], yet it hasn't incorporated T2* and FF mapping. In this work, we extend MR multitasking for more comprehensive myocardium tissue characterization (T1, T2, T2*, FF) and cine imaging. In addition, the technique can quantify water specific T1 (T1w), which has enhanced sensitivity for detecting fibrosis[6,7].

Methods: Sequence design: Different from previous MR Multitasking work for T2* quantification[8,9] in the brain and liver, we use a variable TR approach (VTR) to collect training data with minimal impact on temporal resolution and imaging efficiency. As shown in Fig. 1, hybrid T2IR preparation modules with different preparation times are followed by radial multi-echo FLASH readout modules. Acquisition alternates between a short-TR, single-echo training data readout and a longer-TR, multi-echo imaging data readout module. The imaging data are incremented by the golden angle, and navigator data are acquired at the 0° spoke.

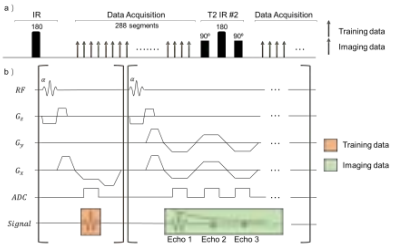

Figure 1. Sequence diagram

Imaging framework: Based on the MR Multitasking framework, we model the underlying image series as a 6D low-rank tensor with one combined voxel location dimension and 5 temporal dimensions encoding cardiac time index, respiratory time index, T2 prep time, inversion time, and echo time. The temporal-spatial correlation allows us to efficiently factor the tensor as the product of a spatial factor $\boldsymbol{U}$ and temporal basis Φ. The Φ is extracted from the high-temporal-resolution training data, and the spatial coefficients in $\boldsymbol{U}$ are determined by fitting Φ to the corresponding imaging data.

Data Collection: Three healthy volunteers were imaged on a 3T scanner (MAGNETOM Vida, Siemens Healthcare, Erlangen, Germany). Multitasking parameters include FA=5°, FOV=270x270mm^2, slice thickness=8mm, spatial resolution=1.7x1.7mm^2, TR/TE$_1$/ΔTE=16.6ms/1.6ms/1.3ms for imaging data (11 echoes), TR/TE=3.6ms/1.6ms for training data, 5 different T2 preparation times ranging from 0 to 60ms, 1 mid short-axis slice, scan time=2.5min, 20 cardiac bins, 6 respiratory bins. 2D reference Cine images were acquired at end-expiration breath-hold and with retrospective ECG gating. Reference 2D T1 maps with MOLLI, T2 maps with T2-prep FLASH, T2* maps with multi-echo GRE, and fat fraction maps with multi-echo Dixon GRE were acquired at diastole with ECG triggering and end-expiration breath-hold.

Results: The reference maps, reference cine images, multitasking maps, and multitasking cine images from one subject are shown in Fig. 2. The white arrows in the water T1 map indicate where the myocardial wall is better represented in water-fat partial volume regions. The multitasking maps have longer septum T1 (1348 ± 90 ms) than those of the reference (1237 ± 43 ms), which is known to underestimate T1[10]. Multitasking also has lower septum fat fraction (2.5 ± 0.5%) than the reference (6.3 ± 0.3%), potentially due to the presence of T1 bias in the reference method[11]. The fat fraction from Multitasking are closer to previous literature range (~1.9 %)[12]. The septum T2 and T2* values of Multitasking (T2: 40.6 ± 1.7 ms; T2*: 28.0 ± 8.4 ms) are similar to those of the references (T2: 41.8 ± 3.3 ms; T2*: 25.2 ± 7.2 ms). The ejection fraction from Multitasking (54.3 ± 15.4 %) are lower than that from reference cine (61.0 ± 11.7%), which may be a result of different image contrast.

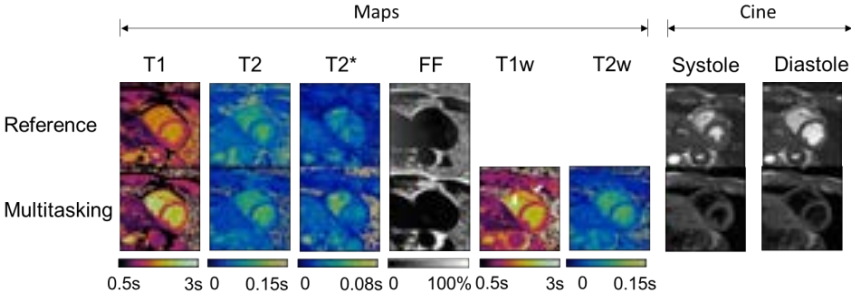

Figure 2. Reference maps, multitasking maps, and cine images in a healthy volunteer. The white arrows in the water T1 map indicate where the myocardial wall is better represented in water-fat partial volume regions.

Conclusion: With a single 2.5-min acquisition, our proposed technique can generate co-registered T1, T2, T2*, fat fraction, and water T1 maps as well as cine images without the need for breath-holding and ECG triggering. Further analysis in a larger cohort is warranted, followed by clinical validation in patients.

References: [1] Bull S, et al. Heart 2013; [2] Ugander M, et al. Jacc-Cardiovasc Imag 2012; [3] Triadyaksa P et al. MRI. 2020; [4] Kenchaiah S et al. J Am Coll Cardiol 2021; [5] Christodoulou AG et al. Nat Biomed Eng 2018; [6] Mozes, FE, et al. NMR Biomed. 2019; [7] Larmour S, et. al. MRM. 2017; [8] Cao T, et al. Proc ISMRM 2020; [9] Wang N, et al. Proc ISMRM 2021; [10] Roujol S, et al. Radiology 2014; [11] Liu C, et al. MRM 2007; [12] Liu C, et al. MRM 2010;

Abstract ID: 33

Convolutional Neural Network for Autonomous Segmentation of Intracerebral Hemorrhage Components for Image Guidance in Minimally-Invasive Surgical Evacuation

Thomas Lilieholm[1], Matthew Henningsen[2], Azam Ahmed[3], Alan McMillan[1,4,5], WF Block [1,4,5]

1- University of Wisconsin at Madison, Medical Physics, 2- University of Wisconsin at Madison, Electrical Engineering, 3- University of Wisconsin at Madison, Neurosurgery, 4- University of Wisconsin at Madison, Radiology, 5- University of Wisconsin at Madison, Biomedical Engineering

Purpose: Treatment of intracerebral hemorrhages (ICH) is often predicated on partial evacuation of the hematoma. ICH survivors often live with severe disability and loss of independence for the rest of their lives. Efforts have been made to use minimally-invasive techniques via ventriculostomy catheters and thrombolytic agents to evacuate these clots efficiently and with minimal risk to the patient over several days. Suction techniques have also been tried to evacuate clots more rapidly. Studies have shown that reduction of clot volume to or below 15 ml in ICH cases corresponds to improved long-term patient outcomes in treatment [1]. Consistently reaching this volume, however, has proven difficult in wide-scale clinical trials. We propose that MR-image guidance coupled with machine learning autonomous segmentation would enable surgeons to better visualize ICH components and regions during surgical procedures, enabling them to more-readily meet this 15 ml goal for improved patient outcomes.

Methods: For producing rapid, autonomous segmentations of ICH anatomy, we made use of a convolutional neural network (CNN). To train the network, 27 T2-w MRI scans of ICH cases were acquired and de-identified from the UW-Hospital records and manually segmented with oversight from a neuroradiology fellow for use in supervised learning. The CNN followed a U-Net styled structure [2] with 5 paired and concatenated convolution/deconvolution layers and periodic batch normalization. Outputs were binary masks of predicted hematoma region, and predicted edema region, based on the initial T2-w scans fed into the network. One output segmentation is the result of two separate networks- one optimized to clot, and the other to edema. The model was optimized to maximize the Dice coefficient (DC) between its own segmentation outputs and the provided manual segmentations. As data volume was relatively low, data augmentation via geometric transform and 9-fold cross validation were both applied, for additional assurances of accuracy. The networks were trained over 400 epochs for each cross validation iteration.

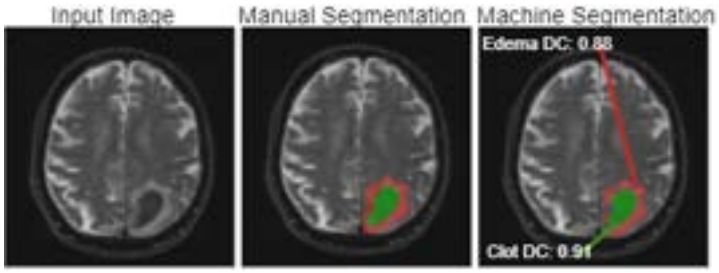

Results: The average DC for all cases in the cross-validated testing datasets was 0.74±0.22 for clot, and 0.68±0.17 for edema. Overall, the model tended to underestimate rather than overestimate these regions of clot and edema. For clot, the model segmentations underestimated the total milliliter volume of clots by an average of 17% relative to the manual.

Discussion: While the model demonstrated robust and accurate segmentations on the scans within the dataset, there are features the model was not trained on. The model was trained only over T2 scans. This is because inconsistent and limited scan protocols for ICH cases did not allow for complete T1/T2 datasets for every ICH case available. We made use of T2 scans because they were among the most-commonly acquired scan types on these patients. Furthermore, several clot morphologies were excluded from data criteria. The model was trained over clots that were unsuitable for surgical evacuation. Namely, clots that were smaller than 1 ml in volume, extremely decentralized and diffuse, or intraventricular, where the bleed breaches the ventricle and leaks into the cerebrospinal fluid.Independent of morphology, is the effects of clot aging. Over time, the extracellular hemoglobin resulting from a hemorrhage breaks down, which results in changing contrast on an MR scan [3]. ICH protocols favor treatment as soon as possible, so for the purposes of this research, we excluded any scans taken 4 days after the patient's hospital admission. Within this 4 day window, there were still significant changes in contrast between clots of differing ages. Though the model was trained over all 27 clots, we found that by subcategorizing the clots into three categories on the basis of their perceived age as determined by the contrast between hematoma core and white matter (with overview from a neurosurgeon), distinct tiers of model accuracy were made apparent. In the 12 acute clots, imaged closest to onset, we found an average DC of 0.9±0.05. The 11 early subacute clots, imaged slightly later from onset, had an average DC of 0.75±0.18. Finally, the 4 late subacute clots had an average DC of 0.38±0.15. In this way, we can see that clots imaged closer to onset provide more accurate results, which is consistent with ideal treatment protocols.

References: [1] Hanley DF et al. Efficacy and safety of minimally invasive surgery with thrombolysis in intracerebral haemorrhage evacuation (MISTIE III): a randomised, controlled, open-label, blinded endpoint phase 3 trial. Lancet. 2019;393(10175):1021-32. Epub 2019/02/12. doi: 10.1016/S0140-6736(19)30195-3. PubMed PMID: 30739747; PMCID: PMC6894906.

[2] Ronneberger O, Fischer P, and Brox T, "U-net: Convolutional networks for biomedical image segmentation." International Conference on Medical image computing and computer-assisted intervention, 234–241 (2015).

[3] Voss, Yves L. "Timeline Diagram of MRI and CT Characteristics of Intracerebral Hemorrhage: Radiology Case." Radiopaedia Blog RSS, Radiopaedia, radiopaedia.org/cases/timeline-diagram-of-mri-and-ct-characteristics-of-intracerebral-haemorrhage?lang=us.

Abstract ID: 34

Evaluation of Pulmonary Hypertension Using 4D Flow MRI

Cerne, John W.[1]; Pathrose, Ashitha[1]; Gordon, Daniel Z.[1]; Sarnari, Roberto MD[1]; Veer, Manik[2]; Blaisdell, Julie[1]; Allen, Bradley D.[1]; Avery, Ryan[1]; Markl, Michael[1,3]; Ragin, Ann[1]; Carr, James C.[1]

[1]Northwestern Radiology, [2]Northwestern Medicine, [3]Northwestern Biomedical Engineering

Purpose. Cardiac magnetic resonance (CMR) is gaining attention as a non-invasive alternative to right heart catheterization (RHC) for pulmonary hypertension (PH) evaluation. Hemodynamic parameters derived from RHC are the current gold-standard means of distinguishing pre-capillary PH (PRE-PH) from post-capillary PH (POST-PH). POST-PH patients require a different treatment approach than PRE-PH patients. The purpose of this study was to compare 4D flow MRI-derived velocities in the pulmonary arterial vasculature between PRE-PH patients, POST-PH patients, and healthy controls, using RHC as the standard-of-reference.

Methods. PH patients diagnosed using standard-of-care RHC (resting mean pulmonary artery pressure ≥25 mmHg) were recruited to undergo CMR including 4D flow MRI within 30 days of RHC. Age and sex matched healthy controls (N=25, age=52±13 years, 16 males) were prospectively enrolled and underwent the same CMR protocol. A cardiologist grouped PH patients into PRE-PH (N=29, age=55±8 years, 10 males) and POST-PH (N=19, age=66±13 years, 9 males) based on RHC cutoff values and clinical history[1]. The respiratory-navigator gated 4D flow sequence was performed in a sagittal oblique orientation after contrast administration. 4D flow analysis was performed with commercial software (Circle Cardiovascular Imaging) using a 3-step workflow (Fig 1).

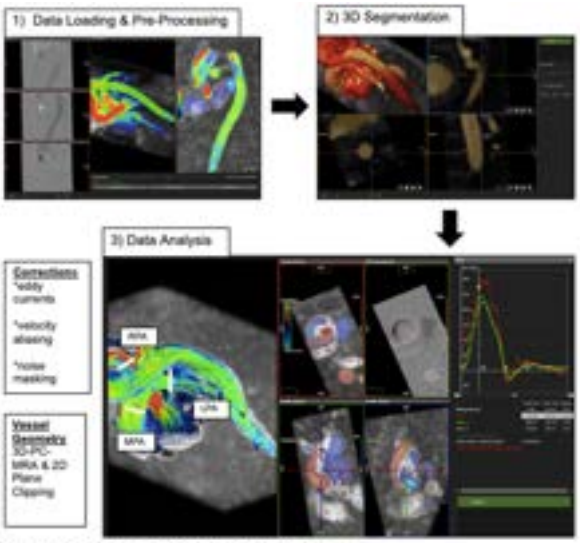

Figure 1. 4D flow data interpretation workflow

Results. PRE-PH had significantly lower peak velocities than POST-PH at the RPA (44.19±13.94 cm/sec vs. 67.94± 26.44 cm/sec) and LPA (38±12 cm/sec vs. 59±15 cm/sec). Significant differences were also found between PRE-PH and healthy controls at the LPA (32±9 cm/sec) and RPA (40±9 cm/sec) (Fig 2). Significant correlations between peak velocities and pulmonary vascular resistance were moderate at the LPA and RPA (r=-.56 and r=-.43, respectively) in PRE-PH and at the LPA (r=-.55) in POST-PH (Fig 3).

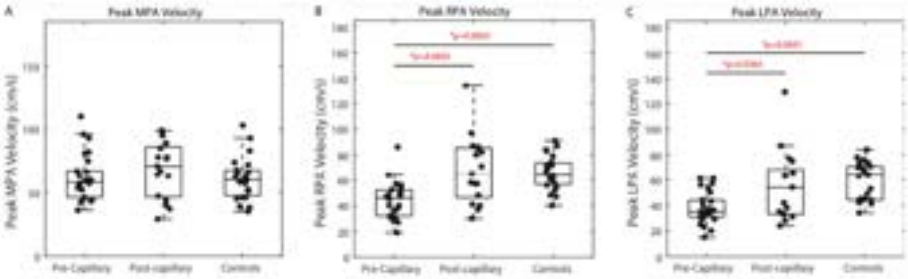

Figure 2. Peak and velocities in pre-capillary pulmonary hypertension (PH), post-capillary PH, and control subjects at the MPA, RPA, and LPA. Box plots comparing the mean and peak velocities at the main pulmonary artery (MPA; A), right pulmonary artery (RPA; B), and left pulmonary artery (LPA; C). (*) Indicates significant difference ($p < 0.05$).

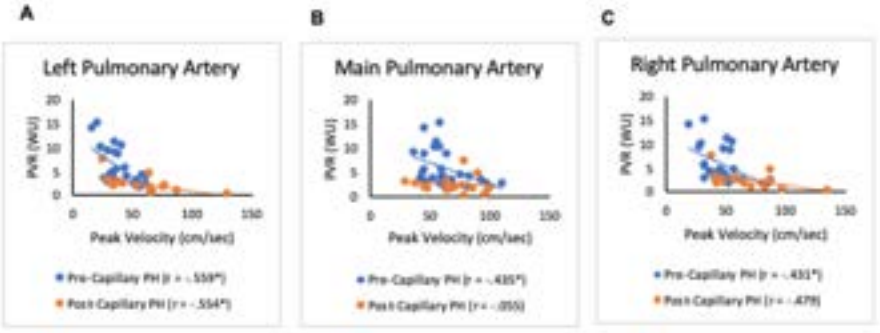

Figure 3. Pearson correlations between pulmonary vascular resistance (PVR) and peak velocity in pre-capillary and post-capillary pulmonary hypertension (PH) patients at the left pulmonary (A), right pulmonary (B), and main pulmonary (C) arteries. (*) Indicates significant correlation ($p < 0.05$).

Discussion. 4D flow MRI found significant velocity differences in both the LPA and RPA when comparing PRE-PH and POST-PH. Significant correlations were also seen between increasing PVR and decreasing pulmonary artery peak velocities when patients were categorized into hemodynamic groups. PVR has prognostic implications. Our findings suggest that velocity data may complement RHC for classifying and assessing PH patients. This study is limited by the time interval between the RHC procedure and CMR acquisition. Disease severity may have worsened or lessened, depending on treatment that occurred during this interval (20.6±5.8 days). Future work will be designed with same-day RHC and MRI procedures.

References. [1] Galiè, *Eur Heart J*, 2016.

Abstract ID: 35

Multi-planar, multi-contrast and multi-time point analysis tool (MOCHA) for intracranial vessel wall imaging analysis

Yin Guo[1], Gador Canton[2], Jie Sun[2], Li Chen[3], Thomas S Hatsukami[4], Chun Yuan[1,2]
[1]Department of Bioengineering, [2]Department of Radiology, [3]Department of Electrical and Computer Engineering,
[4]Department of Surgery, University of Washington, Seattle, WA, United States

Introduction: To design and implement an image analysis pipeline (MOCHA) that can register multi-contrast and multi-time point 3D vessel wall (VW) MRI for flexible and time-efficient multi-planar view and quantitative characterization of intracranial VW morphology, with a particular emphasis on intracranial atherosclerosis (ICAD). MOCHA is an integrated, streamlined and optimized workflow that features four distinct benefits: 1) automatic artery tracing and labeling extract segments of interest from the complicated intracranial artery tree; 2) a reliable registration ensures same plaque location from images of different contrast weightings and time points; 3) rotational straightened MPR views provide comprehensive display of the selected artery; 4) cross-sectional views allow consistent quantification of plaque features.

Methods:

MOCHA workflow: 1) Registration. Automatic 3D rigid registrations, using mutual information as the similarity metric, were performed to register multi-contrast and multi-time point images to the reference scan (Fig 1). In this study, the post-contrast T1-VISTA sequence was selected as the reference due to its clear boundaries of lumen and wall (ref) and high signal-to-noise ratio. 2) Artery tracing and labeling. An open-curve active contour model (iCafe) was used to automatically identify artery centerlines from registered TOF MRA (ref) of the reference scan. 12 vessel landmarks were then computed by maximum a posteriori estimation, and 15 vessel segments were subsequently labeled. Fig 2 demonstrated the landmarks utilized and segments of analysis in this study. With registration in place, artery traces and labels could be shared with other time points. 3) Tailored MPRs generation. For each vessel segment, coordinates of the centerline were used to interpolate for generation of straightened MPR images. Rotation of profiles in each cross-sectional image led to rotated MPR views for display of the specified artery. Selected vessel trace, cross-sectional slices and straightened MPR views were all synchronized by viewing angles and slice positions, with multiple contrast weightings side by side, in a specially designed GUI (Fig 3), dedicated for an interactive visualization and quantification.

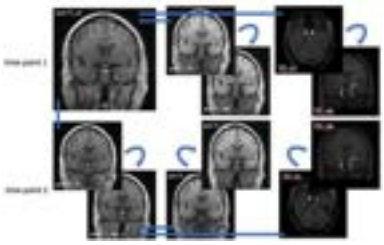

Fig 1 An example registration scheme of pre- and post-contrast T1-VISTA and TOF in two time points.

Dataset and experimentation:

Six patients with diagnosed ICAD received two identical MRIs with an interval of around one week. All the reconstructed cross-sectional and straightened MPR images of pre-contrast T1-VISTA, post-contrast T1-VISTA, DANTE-PD and TOF were displayed. At the same location on both imaging sets, 15 following vessel segments were analyzed for each patient: the distal BA, the distal VAs, the petrous ICAs, the cavernous ICAs, the supraclinoid ICAs, the proximal MCAs, the proximal ACAs and the proximal PCAs. For each segment, atherosclerotic lesions were identified based on the guidelines established by (ref). Lumen and outer wall boundaries of the detected plaque were manually traced. Inter-scan reproducibility of plaque detection and lesion quantification were evaluated to facilitate future longitudinal studies.

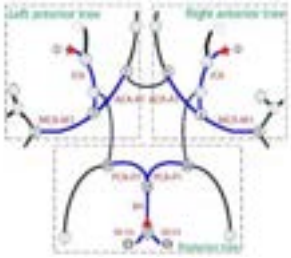

Fig 2 Demonstrations of the 12 artery landmarks and the 15 vessel segments used in this MOCHA study

Results: The agreement of plaque detection is 92.8% (kappa=0.7981). Table 1 and Fig 4 show excellent inter-scan reproducibility of lesion quantification for the same 17 plaques that were detected in both analyses.

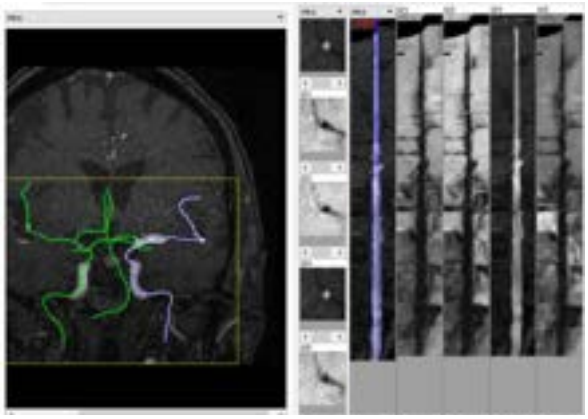

Fig 3 The interactive analysis GUI with synchronized vessel trace, cross-sectional slices and straightened MPR views (S101: pre-contrast T1-VISTA; S103: PD; S104: TOF; S105: post-contrast T1-VISTA)

Table 1 Inter-scan reproducibility of atherosclerotic lesion quantification

	ICC	95% CI
Plaque length	0.9573	(0.8689,0.9842)
Average lumen area	0.9815	(0.9511,0.9932)
Average wall area	0.9521	(0.8758,0.9822)
Max wall thickness	0.9193	(0.7983,0.9698)
Average wall thickness	0.9438	(0.8554,0.9791)
Normalized wall index	0.9655	(0.9096,0.9873)

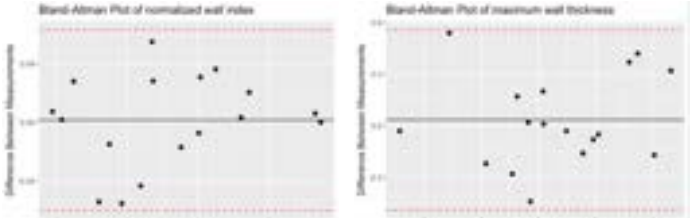

Fig 4 Bland-Altman plot of normalized wall index and maximum wall thickness

Abstract ID: 36

Deep Learning Automated Segmentation of CE-MRA Left Atrial Structures of AF Patients

Justin Baraboo[1,2], Amanda DiCarlo[2], Mitchell Collins[2], Maurice Pradella[2], Rod Passman[3], Philip Greenland[3], Daniel Lee[3], Dan Kim[1,2], Michael Markl[1,2]

[1]Northwestern Biomedical Engineering, [2]Northwestern Radiology, [3]Northwestern Medicine, Cardiology

Introduction Atrial fibrillation (AF) is the most common sustained cardiac arrhythmia and can result in thrombus formation in the left atrium (LA) or appendage (LAA), a leading cause of ischemic stroke. Contrast enhanced MR angiography (CE-MRA) has been clinically utilized for pulmonary vein (PV) mapping prior to AF therapy by catheter ablation, and LA and LAA morphology has been shown to correlate with AF and stroke risk.[1,2] Automated segmentation of the atrial structures (LA, LAA, and PV) may prove useful for streamlined clinical care and treatment management. The goal of this study was to develop a deep learning (DL) tool to automatically segment the LA, LAA, and PV anatomies in AF patients from time-resolved 3D CE-MRA.

Methods 88 prospectively enrolled AF patients [age 63±9, 64 Male] underwent time-resolved CE-MRA pulmonary vein mapping [spatial resolution = 1.3-1.8 mm^3, temporal update rate = 5-5.3 secs, 14 3D volumes] prior to catheter ablation. A 3D segmentation of the LA, LAA, and main branches of the PV were manually performed by three observers (MIMICS, Materialise, Belgium) for one CE-MRA time point determined by visually assessing maximal contrast in the LA. These served as the ground truth for training and testing of a deep learning network. We utilized a 3D U-Net[3] with dense layers architecture with 4 label outputs to learn how to individually segment the LA, LAA, and PV from a CE-MRA volume input (Figure 1). Fivefold cross validation was utilized (68-71 training sets and 17-20 test sets per fold). Dice scores (DSC) were calculated between deep learning and manual segmentation for 1) fused left atrial structure (LA-LAA-PV), and 2) each sub structure alone. We aggregated results across all five testing sets. LA and LAA volumes were calculated and compared between workflows using a Wilcoxon signed rank sum test ($\alpha = 0.05$), Pearson's correlation r^2, and Bland Altman analysis (bias and limit of agreement (LoA)).

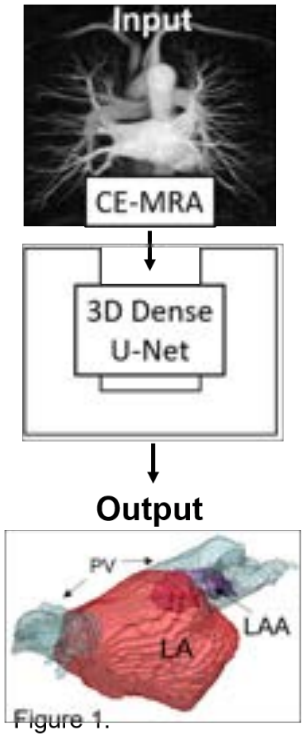

Figure 1.

Results Median fused LA-LAA-PV structure DSC were 0.90 [q1: 0.86, q3: 0.92] and the manual vs DL derived structure with the median DSC score is shown (Figure 2). Individually, median LA DSC were the highest with 0.93 [0.90, 0.94] with only three patients having low (DSC <0.80) scores. Median LAA DSC were 0.75 [0.64, 0.80], and median pulmonary vein DSC were 0.68 [0.61, 0.74]. Manual and DL LA volumes were not significantly different (Median Manual: 95 ml, Median DL: 99 ml, p = 0.52), strongly correlated ($r^2 = 0.92$) and had no significant bias (p=0.26) with LoA of -20 and 23 ml (Figure 3). DL and manual LAA volumes were not significantly different (Median Manual: 5.4 ml, Median DL: 5.2 ml, p=0.22), weakly correlated ($r^2 = 0.48$), with no bias (p=0.15) and LoA of -5.1 and 5.1 ml.

Discussion A DL tool was developed to segment the left atrial anatomy in CE-MRA of AF patients. LA automatic segmentation was successful in bulk shape segmentation and measured volumes, likely due to high signal contrast and comparatively larger anatomy. LAA and PV had lower DSC most likely due to their smaller, more variant morphologies being harder to learn and consistently segment. Our finding is similar to published reports of deep learning segmentation of left ventricular scars, which also have small patches.[4] Further, ground truth PV segmentations did not have a uniform anatomic coverage (e.g. after 3 branches or set distance) among observers, leading to cases where DL based analysis segmented the central parts of the PVs but not enough in the periphery (Figure 2) or segmented even more than the manual observer. Deep learning segmentation shows highly encouraging results for fully automated LA segmentation and promise for LAA and PV segmentation.

Median Fused LA, LAA, PV Segmentation

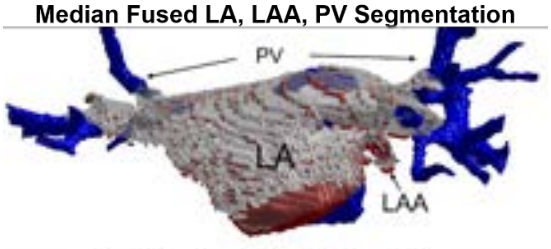

Blue – Deep Learning Missing Segmentation
Red – Deep Learning Over Segmentation
Gray – Manual and Deep Learning agreement
Figure 2.

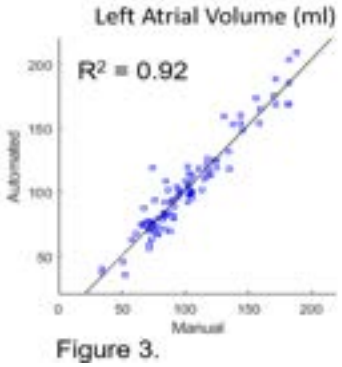

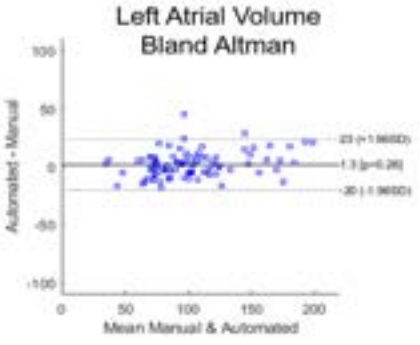

Figure 3.

References 1)Xu et al. Front Neurol 2020. 2)Masci et al. Front Physiol 2018. 3) Cicek et al. MICCAI 2016. 4) Fahmy et al. JACC 2018.

The Research of relationship between the left or right hemisphere ischemic stroke and left ventricular systolic function

Lijuan Zheng[1] Xin Lin[2] Yunjing Xue[1*]

[1]Department of Radiology, Fujian Medical University Union Hospital, Fuzhou, China

[2]Department of Neonatology, Fujian Maternity and Child Health Hospital, Affilated Hospital of Fujian Medical University, Fuzhou, China

*The author contributed equally to this work and is co-corresponding author.

Authors' contributions: L-J.Z wrote the main manuscript text, collected the clinical data and parameters. X.L analyzed the clinical data and parameters. Y-J.X amended the manuscript text.

Correspondence to: Yunjing Xue, MD Fujian Medical University Union Hospital, Department of Radiology, Fuzhou, 350001, China. Email: 1144150522@qq.com

Abstract

Background: There was a relationship between acute stroke and cardiac dysfunction, especially for the insular location of ischemic stroke. Although it was established that the activity of autonomic decreased after infarcts at either hemisphere, the different hemisphere of ischemic stroke could change left ventricular systolic function whether or not was still uncertain. There was a need to study the association between left or right hemisphere infarction and cardiac function.

Method: The patients retrospectively enrolled were hospitalized for cerebral infarction in the Department of Neurology from January 2020 to May 2021. After accepted the examination of magnetic resonance imaging (include diffusion weighted imaging sequence), echocardiography and hematology testing, they were divided into two groups according to the stroke locations: left hemisphere group and right hemisphere group. Patients with cardiac dysfunction (abnormal electrocardiogram or myocardial enzyme) were excluded before ischemic stroke.

Results: 43 patients were enrolled in total, including 21 of them with left-side group (63.6±3.5 years), and 22 of them with the right hemisphere group (64.0±3.5 years). No differences of demographic characteristics between two groups ($P>0.05$). The average of left ventricular ejection fraction (LVEF) (67.06±1.27) and fractional shortening (FS) (37.32±0.99) in the left hemisphere group were significantly lower than those (71.04±1.22, 40.49±1.04) in the right hemisphere group ($P<0.05$).

Conclusions: The differences of the left ventricular systolic function (EF and FS) corresponding with two sides of cerebral hemisphere infarction were found in the study, and which were related to a better regulation protection of the left cerebral infarction by the vagus nerve. In order to reduce the incidence rate of cardiac ventricular dysfunction, it is suggested clinical doctors to pay more attention to the right hemisphere stroke.

Abstract ID: 38

A study on the size of 3D patch in the vascular segmentation of neck TOF MRA images based on 3D ResUnet

Qiu Wei[1], Wei Hanyu[1], Zhang Miaoqi[1], Li Rui[1]
[1]Center for Biomedical Imaging Research, Department of Biomedical Engineering, School of Medicine, Tsinghua University, Beijing 100084, China

Purpose: To investigate the effect of the size of the 3D crop patch on the performance of the 3D ResUnet model in the vascular segmentation of 3D neck TOF MRA.

Methods: A total of 166 neck TOF MRA images were selected from the Cardiovascular Risk of Old Population(CROP) study. Vessel segmentation labels were manually delineated by professional means. The dataset was divided into training, validating and test dataset according to a ratio of 8：1：1. 3D ResUnet was utilized as the segmentation model. Three different sizes (Large:256×256×64, Medium:192×192×64 and Small:192×192×32) of 3D patch randomly cropped from the original image were selected for model training and predicting. The Dice coefficients of different parameters were calculated on the testing dataset with manual annotation results as the gold standard. The average and standard deviation of the Dice values under 10-fold cross-validation were used to evaluate the segmentation performance of the model. In this comparative experiments, One-way ANOVA was carried out for the experiments of the three kinds of patch size.

Results: The 3D ResUnet model obtained the highest segmentation Dice coefficient value (0.9239) and the smallest standard deviation (0.0096) by selecting large-size patch (Table 1). In the results of One-way ANOVA (Figure 1), the $p<0.001$, indicated that the results of different patch sizes had significant differences.

Conclusion: The 3D ResUnet model, using larger-size crop patch for training, has better performance in blood vessel segmentation of the neck TOF MRA images. This study can provide the basis for the optimization of neural network performance parameters, and then provide more accurate vascular morphology information for clinical diagnosis.

Table 1: Statistical results of segmentation accuracy under different patch sizes under 10 fold cross validation

Size	Dice (Std)
Large	**0.9239（0.0096）**
Medium	0.9058（0.0132）
Small	0.8748（0.0149）

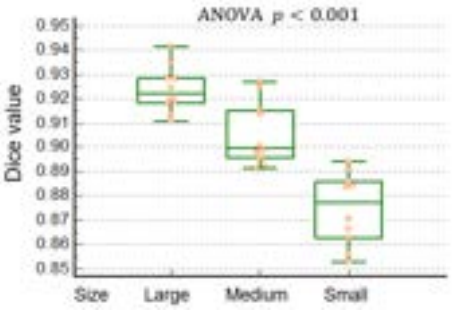

Figure 1: Statistical distribution and one way ANOVA of Dice value.

Abstract ID: 39

An investigation on the similarity-driven multi-dimensional binning algorithm using a numerical phantom simulation

Ludovica Romanin[1,2], Christopher W. Roy[1], John Heerfordt [1,2], Matthias Stuber[1,3] Davide Piccini[1,2]
[1]Department of Diagnostic and Interventional Radiology, Lausanne University Hospital and University of Lausanne, Lausanne, Switzerland; [2]Advanced Clinical Imaging Technology, Siemens Healthcare AG, Lausanne, Switzerland; [3]Center for Biomedical Imaging (CIBM), Lausanne, Switzerland.

Purpose: Due to the long acquisition times associated with whole-heart MRI, data collection is usually performed during free-breathing and triggered with the use of an ECG device. Several methods have been proposed to explicitly extract cardiac and respiratory motion: ECG-triggering (1), navigator-gating (2), self-navigation (3), or retrospectively binned free-running acquisitions (4). Recently, a similarity-based multi-dimensional binning algorithm (SIMBA) has been introduced for the reconstruction of a static 3D volume from a free-running acquisition by projecting the acquired data into a lower dimensional space and exploiting their intrinsic similarities without explicitly targeting a predefined cardiac or respiratory phase (5). SIMBA was shown to effectively reconstruct images with minimized motion artifacts by selecting a subset of the data within the respiratory and cardiac resting phases. However, a more in-depth understanding of the relationship between the physiological states and the data distribution in the lower dimensional space is still missing. In this work we therefore employ well-controlled numerical phantom simulations to better characterize the data distribution and the data selection via clustering in SIMBA.

Methods: The numerical phantom used in this study (6,7) is derived from the XCAT framework (8). The phantom can generate high resolution (1 mm^3) 3D volumes of the whole heart for user defined cardiac and respiratory motion positions and assign specific intensity values to each tissue type (9) before generating 3D radial k-space data (7). In this work, we simulated 50 distinct cardiac and 30 respiratory phases. As part of the simulation framework, the amplitude of the respiratory phases varied with a maximum displacement of 2 mm in RL, 12 mm in AP, and 20 mm in FH direction. Different scenarios were simulated: only respiratory motion, only cardiac motion, both respiratory and cardiac motion, and no motion as a reference. Simulation of the data acquisition scheme as well as the SIMBA reconstruction steps were performed as in the original paper (5). The number of clusters was chosen according to the search procedure in (5) but within a bigger range, i.e. from 10 to 30, to account for the high number of simulated respiratory phases. The data distribution in the lower dimensional space was visually assessed by plotting the principal components against each other and quantified by computing the Euclidean distance (d) between pairs of points in different phases. Finally, two 3D gridded reconstructions were compared: the first including only data from the SIMBA-selected cluster, and the second including all the data. The quality of the reconstructed images was compared by visually assessing and quantifying the blood-myocardium sharpness (s_{BM}) by fitting parametrized sigmoid functions as described in (5).

Results: For all the different simulated scenarios, the distribution of the data in the lower dimensional space seems to be correlated with the physiological phases in which they were simulated (Figure 1) and a certain regularity, matching the periodic nature of the physiological signals, can be observed. Two consecutive respiratory phases, e.g. during end-expiration, are relatively close to each other (d=1.23 [a.u.]), while end-expiration and end-inspiration are further apart (d=5.56 [a.u.]). Between adjacent diastolic phases we measure the lowest distance (d=0.55 [a.u.]), while between diastole and early systole the distance is the highest (d=9.42 [a.u.]). When simulating both cardiac and respiratory motion, the respiratory motion dominates the data distribution. In the reconstructed volumes, the observed cardiac features as well as the liver dome always appear visually sharper in the images reconstructed with SIMBA than those using all data. The SIMBA images, however, are overall noisier due to the selection of a reduced amount of reconstructed data thus resulting in undersampling artifacts. When we apply an equivalent SIMBA selection to the reference dataset without simulated motion, the sharpness is higher (s_{BM}=3.73 [a.u.]) than the one from the reconstructed image with both cardiac and respiratory motion (s_{BM}=2.63 [a.u.]) (Figure 2). End-expiration is the respiratory phase consistently selected by SIMBA, while a mixed set of cardiac phases is usually selected (Figure 1).

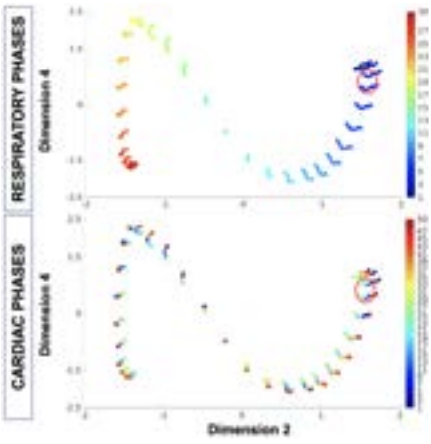

Figure 1. Visualization of the data in the lower-dimensional space when simulating both respiratory and cardiac motion. The points are color coded according to the physiological phases and the data selected by SIMBA are circled in red.

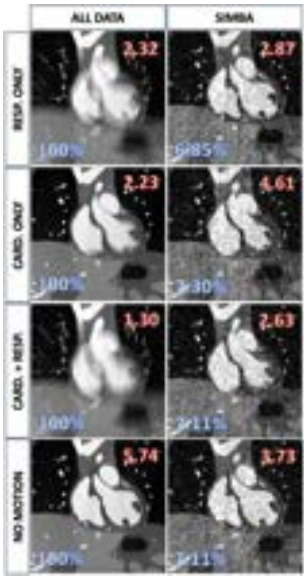

Figure 2. Reconstructed images. The percentage of points selected (blue) and sharpness (red) are reported.

Discussion: The lower-dimensional space in which the data is projected by the SIMBA algorithm shows direct correlations with the simulated physiology, although a two-dimensional visualization of the principal components has some limitations. In the future, we plan to apply these insights to directly reconstruct a specific cardiac phase using SIMBA, and concurrently optimize the dimensionality reduction and clustering steps, transferring this knowledge in vivo. Additionally, we could also consider implementing and training a neural network using a rich dataset combining both simulated data from the numerical phantom and in vivo datasets.

References: [1] Sievers B, JCMR 2005, 7:587–593 [2] Ehman R, AJR 1984, 143:1175–1182 [3] Stehning C, MRM 2005, 54:476–480 [4] Coppo S, MRM 2014, 74:1306–1316 [5] Heerfordt J, MRM 2021, 86:213–229 [6] Roy CW, JCMR 2019, 21 [7] Roy CW, JCMR 2021, 23 [8] Segars WP, Med Phys 2010, 37:4902–4915 [9] Wissmann L, JCMR 2014, 16 [10] Piccini D, MRM 2011, 66:1049–1056

Abstract ID: 40

Cerebral blood flow distribution at different phases in different types of Circle of Willis using 4D Flow imaging

Xiaoyan Bai[2], Zhiye Li[2], Peiyi Gao[2], Yan Lin[2], Haiqing Zhao[3], Binbin Sui[1,2]

1. Tiantan Neuroimaging Center of Excellence, China National Clinical Research Center for Neurological Diseases, Beijing, China; 2. Department of Radiology, Beijing Tiantan Hospital, Capital Medical University, Beijing Neurosurgical Institute, Beijing, China; 3. Department of Radiology, Beijing ChuiYangLiu Hospital, Beijing, China.

Objective Variants of the Circle of Willis (CoWs) have implications for stroke etiology and outcome as they present several primary types of collateral pathways and are associated with aneurysm formation [1-2]. This study investigated the cerebral blood flow distribution during cardiac phases between different types of the Circle of Willis.

Methods Four-dimensional flow magnetic resonance imaging (4D flow MRI) was used in 30 healthy subjects (18 females and 12 males, mean 27.5±4.1 years old). CoW was classified into six types according to the vessel anatomical structures. The cerebral blood flow distribution in different arteries and the total cerebral blood flow (tCBF) were analyzed and compared between the different types of CoWs. The changes of cerebral blood flow during different phases of the cardiac cycle were observed and compared between the different types of CoWs.

Results Twelve subjects (40%) had complete CoW (Type I), and 18 (60%) had incomplete CoW (including Type II: ACoA absent; Type III: bilateral PCoA absent; Type IV: unilateral PCoA opening; Type V: Fetal-type PCA with the contralateral PCoA opening; and Type VI: Fetal-type PCA with the contralateral PCoA absent) (Figure 1). No significant difference was found in tCBF between the different CoWs (P=0.787). In Type V, the average flow rates (FRavg) at contralateral ICA was significantly higher than that of the ipsilateral ICA (P=0.003) (Figure 2). During the peak systolic and end diastole, compared with Type I, the Δflow rates (ΔFR) at bilateral MCA in Type IV were significantly higher than that of Type I (P=0.012 and P=0.006, respectively). The ΔFR at contralateral MCA in Type V was significantly higher than that of Type I (P=0.007).

Conclusions and Discussion

Blood flow distribution differs in different types of CoWs during the different phases of the cardiac cycle, especially in type IV and type V at peak systolic. Our study analyzed the anatomical variation in CoWs from the perspective of hemodynamics. We found that the blood flow changes during the cardiac cycle in Type IV or Type V were significantly higher than Type I. Such flow fluctuation and hemodynamic changes of different phases may cause damage to the endothelial cell of vessel wall. Whether it is an important factor leading to aneurysm formation, atherosclerotic disease, plaque rupture or intraplaque hemorrhage needs to be further investigated.

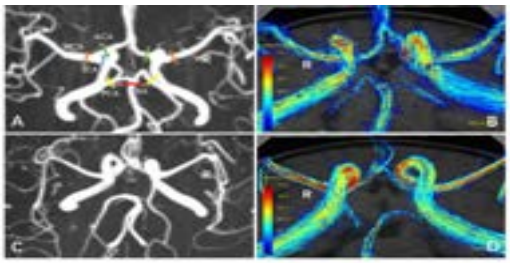

Figure1.The interception analysis plane of each artery in the complete(A) and incomplete (B) CoWs on the 3D-TOF MRA and the 3D streamlines demonstrate the blood flow field colored by velocity magnitude (C and D).

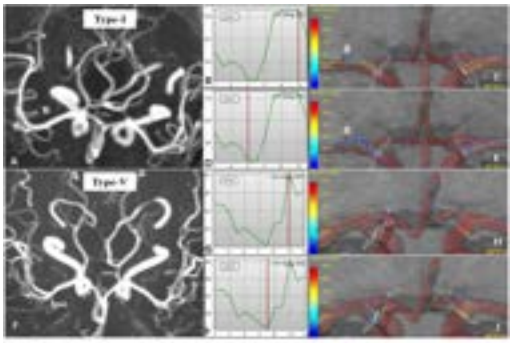

Figure 2. Comparison of the cerebral blood flow velocity and flow rates at different phases of the cardiac cycle between Type I (A-E) and Type V (F-J).

References

[1] Liebeskind DS.Stroke. (2003) 34:2279-84.

[2] Kluytmans M, et al. Stroke. (1999) 30:1432-9.

Abstract ID: 41

Standardization of the Intracranial Atherosclerotic Plaque Enhancement Measurement by Using Multi-phase Contrast-enhanced Vessel Wall MRI

Beibei Sun[1], Lingling Wang[1], Xiao Li[1], Jin Zhang[1], Jianjian Zhang[1], Jiaqi Tian[1], Chengcheng Zhu[2], Huilin Zhao[1]

[1] Department of Radiology, Renji Hospital, Shanghai Jiaotong University, Shanghai China

[2] Department of Radiology, University of Washington, Seattle, WA, United States

Purpose：Plaque enhancement is a marker of intracranial plaque instability related to stroke risk. However, there have no unified method to quantify intracranial plaque enhancement (IPE). We aim to explore optimal reference structure to normalize IPE and the optimal post-contrast timing using multi-phase contrast-enhanced MRI.

Methods：Patients with acute stroke prospectively underwent vessel wall MRI (SPACE with MSDE blood suppression module, whole brain coverage, 0.6mm isotropic) with 1 pre-contrast phase and 4 consecutive post-contrast phases using 3.0T MRI scanner. Each scan was 9 minutes. The total scan time of 4 post-contrast phases was 36 minutes. The signal intensity (SI) values of intracranial structures (including white matter, grey matter, middle infundibulum, low infundibulum, muscle, cavernous sinus, choroid plexus, cerebrospinal fluid) on both pre- and post-contrast phases were measured to select an optimal reference structure to normalize IPE. Intracranial plaque enhancement index (PEI) of each post-contrast enhanced phase was calculated with the following formula: $PEI = ([SI_{Plaque\text{-}post}/SI_{reference\text{-}post}] - [SI_{Plaque\text{-}pre}/SI_{reference\text{-}pre}])/(SI_{Plaque\text{-}pre}/SI_{reference\text{-}pre})$ (where “pre” indicates pre-contrast and “post” indicates post-contrast). The trend of PEI after contrast enhancement was analyzed for both culprit and non-culprit plaques. Enhancement was also graded into 0 (none), 1(higher than normal vessel wall) and 2(similar or higher than low infundibulum).

Results：30 acute stroke patients (30 culprit plaque and 83 non-culprit plaque) were included in this study. The SI values of white matter of brain, grey matter of brain and infundibulum, muscle, cavernous sinus and choroid plexus changed significantly in the 4 post-contrast phases (changes up to 30%, $p<0.05$), while cerebrospinal fluid showed no significant difference in SI values for post-contrast phases ($p>0.05$) and was selected as reference structure to standardize the PEI. The mean PEI of culprit plaque increased during the first 3 post-contrast enhanced phases and reached its maximum in the 3 post-contrast enhanced phases (in about 27 mins), while mean PEI of non-culprit plaque kept constant during the 4 post-contrast enhanced phases (in about 36 mins). The percentage of grade 2 tends to increase during 4 post-contrast enhanced phases in culprit and non-culprit plaque, while the percentage of grade 1 gradually decreased during 4 post-contrast enhanced phases.

Discussions：Cerebrospinal fluid should be considered as an optimal reference structure for quantifying plaque enhancement, and using other structures will lead to significant variability. Protocols should be designed to maximize the post-contrast delay up to 27 minutes after contrast administration to best demonstrate the enhancement of culprit plaques. Pooling results from multiple studies with different timing should be cautious. It is critical to standardizer the post-contrast timing in multi-center studies because the plaque enhancement changed significantly over time. Our study provided a basis for designing future multi-center studies targeting intracranial plaque and stroke risk.

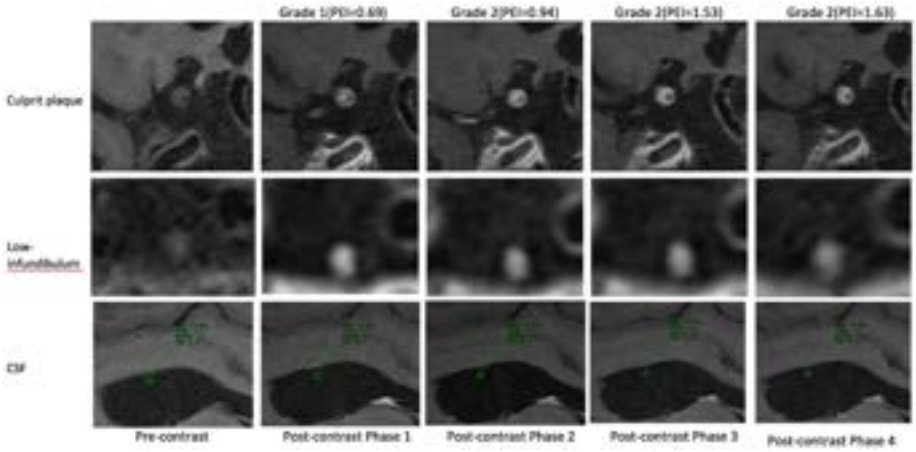

Figure. An example of a culprit plaque. Top: plaque has increased signal after contrast injection. Middle, Low infundibulum has decreased signal over time. Bottom: CSF has constant signal over time. The enhancement grade changes from 1 to 2 from phase 1 to 2; PEI increases from 0.69 (phase 1) to 1.63 (phase 4).

Abstract ID: 42

Standardization of Intracranial Aneurysm Enhancement Measurement by Using Multi-phase Contrast-enhanced Vessel Wall MRI

Xiao Li[1], Jianjian Zhang[1], Beibei Sun[1], Jin Zhang[1], Jiaqi Tian[1], Lingling Wang[1], Bing Zhao[2], Huilin Zhao[1], Chengcheng Zhu[3]

[1] Department of Radiology, Renji Hospital, Shanghai Jiaotong University, Shanghai China

[2] Department of Neurosurgery, Renji Hospital, Shanghai Jiaotong University, Shanghai China

[3] Department of Radiology, University of Washington, Seattle, WA, United States

Purpose: Aneurysm wall enhancement (AWE) is associated with intracranial aneurysms (IAs) instability. However, there have no unified method to quantitatively analyze AWE. We aim to explore optimal reference structure to normalize AWE and the optimal post-contrast timing by multi-phase contrast-enhanced MRI.

Methods: Patients with unruptured IAs prospectively underwent vessel wall MRI (SPACE with MSDE blood suppression module, whole brain coverage, 0.6mm isotropic) with 1 pre-contrast phase and 4 consecutive post-contrast phases using 3.0T MRI scanner. The total scan time of 4 post-contrast phases was 36 minutes. The signal intensity (SI) values of intracranial structures (including white matter, grey matter, middle infundibulum, low infundibulum, muscle, cavernous sinus, choroid plexus, cerebrospinal fluid) on both pre- and post-contrast phases were measured to select an optimal reference structure to normalize AWE. Aneurysm wall enhancement index (WEI) of each post-contrast phase was calculated with the following formula: $WEI = ([SI_{wall\text{-}post}/SI_{reference\text{-}post}] - [SI_{wall\text{-}pre}/SI_{reference\text{-}pre}])/(SI_{wall\text{-}pre}/SI_{reference\text{-}pre})$ (where "pre" indicates pre-contrast and "post" indicates post-contrast). The trend of WEI after contrast enhancement was analyzed for both saccular and fusiform aneurysms.

Results: 34 patients with 42 IAs (27 saccular IAs and 15 fusiform IAs) were included in this study. The SI values of white matter, grey matter and infundibulum changed significantly between pre- and post-contrast phases (p<0.05). While cerebrospinal fluid showed no significant difference in SI values from pre- to postcontrast (p>0.05) and was selected as reference structure to standardize the WEI. The mean WEI of fusiform IAs decreased over time after contrast enhancement while that of saccular IAs kept constant during the 4 post-contrast phases (in about 36 minutes).

Discussions: Cerebrospinal fluid should be considered as an optimal reference structure for quantifying aneurysm enhancement, and using other structures will lead to significant variability. When evaluating fusiform IAs wall enhancement, protocols should be designed to minimize the duration between contrast administration and image acquisition to best demonstrate the enhancement of aneurysm, while the temporal confines might less stringent for saccular IAs. Pooling results from multiple studies with different timing should be cautious. It is critical to standardize the post-contrast timing in multi-center studies because the enhancement of IAs, especially fusiform IAs, changed significantly over time. Our study provided a basis for designing future multi-center studies targeting intracranial aneurysm. In addition, this is the first study to report the distinct contrast enhancement dynamics between saccular and fusiform IAs, however, the underneath pathological differences need further investigation.

References: 1. Fu Q, Wang Y, Zhang Y, et al. Qualitative and Quantitative Wall Enhancement on Magnetic Resonance Imaging Is Associated With Symptoms of Unruptured Intracranial Aneurysms, STROKE, 2021, 52: 213-222. 2. Liu X, Zhang Z, Zhu C, et al. Wall enhancement of intracranial saccular and fusiform aneurysms may differ in intensity and extension: a pilot study using 7-T high-resolution black-blood MRI, EUR RADIOL, 2020, 30: 301-307.

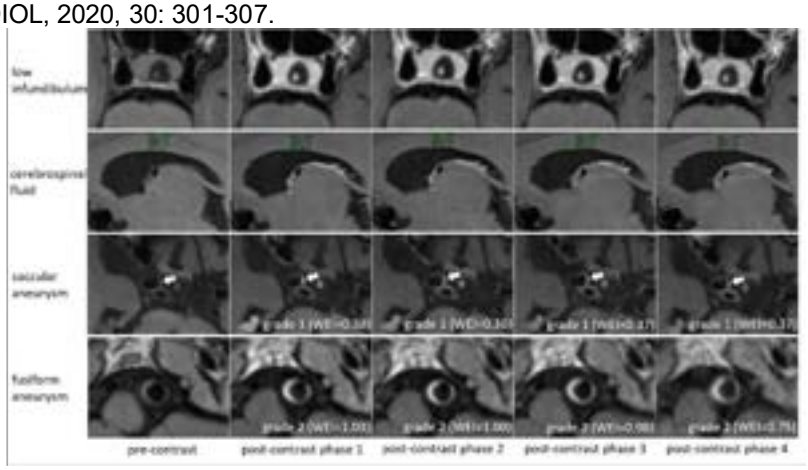

Figure. Cases of reference structure, a saccular IA and a fusiform IA. First row: Low infundibulum has decreased signal over time. Second row: CSF has constant signal over time. Third row: WEI of saccular IA keep constant over time. Fourth row: WEI of fusiform IA decreases from 1.03 (phase 1) to 0.75 (phase 4).

Shorter length of visible intracranial arteries on non-contrast enhanced MRA is associated with cognitive impairment

Zhensen Chen[1], Anders Gould[1,2], Duygu Baylam Geleri[1], Niranjan Balu[1], Li Chen[3], Baocheng Chu[1], Kristi Pimentel[1], Gador Canton[1], Thomas Hatsukami[4], and Chun Yuan[1]

[1]Radiology, University of Washington; [2]Carle Illinois College of Medicine, University of Illinois at Urbana-Champaign; [3]Electrical and Computer Engineering, University of Washington; [4]Surgery, University of Washington

Purpose: Developing novel risk markers for vascular contributions to cognitive impairment and dementia is important[1]. We aimed to explore the associations of a novel imaging marker, i.e. intracranial artery length[2] measured from non-contrast enhanced TOF or simultaneous non-contrast angiography and intraplaque hemorrhage (SNAP) magnetic resonance angiography, with global cognition.

Methods: In 29 older subjects with atherosclerotic disease, TOF and SNAP intracranial artery length, arterial spin labeling (ASL) CBF, and phase contrast (PC) CBF were measured (Figure 1). Linear regression was performed to study their associations with global cognition measured with Montreal Cognitive Assessment (MoCA).

Results: All four imaging measurements were found to be positively associated with MoCA score (All $P < 0.01$). The associations remained significant for TOF intracranial artery length ($P = 0.003$), SNAP intracranial artery length ($P = 0.038$) and PC CBF ($P = 0.032$), after adjusting for clinical covariates and white matter hyperintensity volume (Table 1). The association remained significant for TOF intracranial artery length after adjusting for clinical covariates and ASL CBF or PC CBF.

The TOF/SNAP centerline tracings and CBF maps of 3 representative subjects, with low, median and high MoCA score, are shown in Figure 2 (The first subject (the first row) was a 77-yr-old male with a MoCA score of 18 and a PC CBF of 34.0 ml/100g/min; the second subject (the second row) was a 77-yr-old male with a MoCA score of 25 and a PC CBF of 34.1 ml/100g/min; the third subject (the third row) was a 40-yr-old male with a MoCA score of 30 and a PC CBF of 44.5 ml/100g/min).

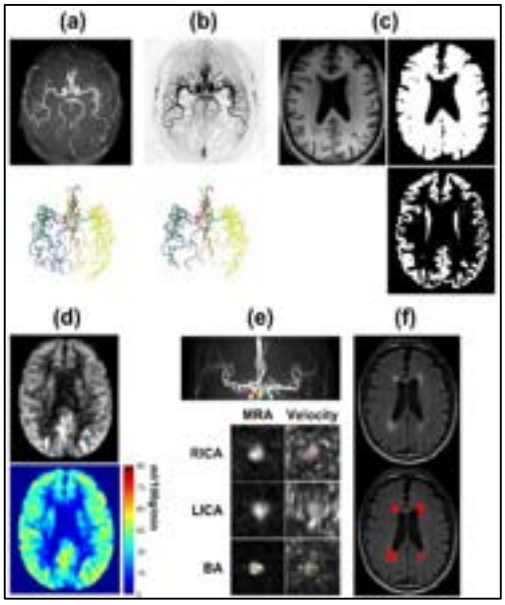

Figure 1. Illustration of image analyses. (a-b): TOF (a) and SNAP (b) MRA was analyzed with iCafe[3] software to yield total vessel length. (c): Brain segmentation and volume calculation was performed on 3D T1W. (d): Gray matter CBF was calculated from ASL. (e): Whole brain PC CBF was calculated from PC images by summing up that of RICA, LICA and BA. (f): Volume of white matter hyperintensity was obtained from 2D FLAIR image.

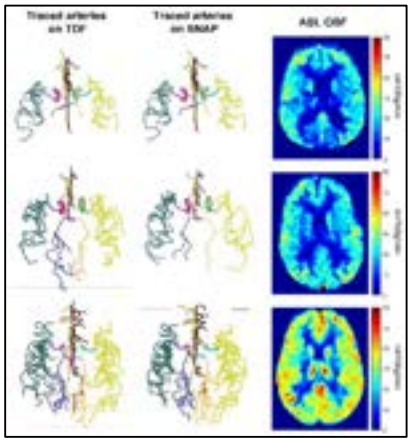

Figure 2. Traced brain arteries on TOF and SNAP, and ASL CBF maps of 3 representative subjects with different MoCA scores.

Table 1. Associations of different brain blood flow measurements, WMH volume with MoCA score (N=29[a])

Blood flow measurement	Univariable linear regression			Multivariable linear regression					
				Model 1[b]			Model 2[b]		
	β	P	adjusted R^2	β	P	adjusted R^2	β	P	adjusted R^2
TOF artery length	0.605	**<0.001**	0.343	0.511	**0.003**	0.497	0.515	**0.003**	0.477
SNAP artery length	0.520	**0.004**	0.244	0.418	**0.040**	0.383	0.443	**0.038**	0.363
ASL CBF	0.526	**0.003**	0.260	0.369	0.097	0.341	0.329	0.097	0.316
PC CBF	0.460	**0.008**	0.202	0.352	**0.046**	0.377	0.427	**0.032**	0.372
WMH volume	-0.178	0.355	-0.004	-0.018	0.923	0.256			

[a]Systolic blood pressure was not available for one subject. Therefore, the same size for Model 1 and Model 2 was 28.
[b]Model 1 was adjusted for age, use of antihypertensive drug and systolic blood pressure; Model 2 was Model 1 plus adjustment for WMH volume.
WMH: white matter hyperintensity; MoCA: Montreal cognitive assessment; SNAP: simultaneous non-contrast angiography and intraplaque hemorrhage; ASL: arterial spin labeling; PC: phase contrast

Discussion: Intracranial artery length on TOF and SNAP MRA is associated with MoCA score, suggesting that intracranial artery length on non-contrast enhanced MRA may be a useful marker of cerebrovascular health in cognitive impairment. Furthermore, the association of TOF intracranial artery length with MoCA score is independent of age, systolic blood pressure, use of anti-hypertensive drug, ASL CBF and PC CBF, suggesting that TOF intracranial artery length provides unique information beyond conventional blood flow measurement about health of distal intracranial medium-sized arteries.

References: 1. Gorelick PB et al. Stroke 2011;42:2672-2713; 2. Gould A et al. MRI 2021; 3. Chen L et al. MRM 2018;79:3229-3238;

Abstract ID: 44

Thin-Slab Stack-of-Stars Multi-echo Quantitative Time-of-Flight (qTOF) MRA for Simultaneous Luminal and Hemodynamic Evaluation of the Intracranial Arteries

Ioannis Koktzoglou, PhD[1,2], Rong Huang, PhD[1], Robert R. Edelman, MD[1,3]

[1]Radiology, NorthShore University HealthSystem, Evanston, IL
[2]Radiology, Pritzker School of Medicine, University of Chicago, IL
[3]Radiology, Feinberg School of Medicine, Northwestern University, IL

Purpose: Time-of-flight (TOF) magnetic resonance angiography (MRA) is routinely used in clinical practice to evaluate the intracranial arteries[1]. However, TOF provides for only luminal evaluation of the intracranial arteries and does not provide quantitative flow information, which may be informative in patients presenting with acute and chronic cerebral pathology. The purpose of this study is to introduce a new quantitative variant of time-of-flight (qTOF) MRA that allows for simultaneous luminal and hemodynamic evaluation of the intracranial arteries, while also performing initial comparisons of the approach to standard 3D TOF as well as 3D phase contrast (PC) MRA.

Methods: This study was IRB approved and all participants (n=10, 5 male, 22-71 years) provided written informed consent. Imaging was done on a 3T system (MAGNETOM Skyra^{fit}, Siemens Healthineers). Inspired from recent work[2], prototype qTOF MRA used a thin-slab multi-echo stack-of-stars fast low-angle shot readout. Blood flow velocity was quantified through 3D analysis of small blood flow displacements between echo times. Parameters for qTOF MRA were: 0.58×0.58×1.0mm^3 spatial resolution interpolated to 0.29×0.29×0.5mm^3, 3 TEs of 2.9ms (TE_1), 5.1ms, and 7.2ms (TE_3), 5.2cm axial coverage, 3 slabs, scan time (TA)=4min3s, ramped RF pulses, bandwidth (BW)=587Hz/pixel, flow compensated TE_1 and TE_3, 213 views acquired in 3 shots with inner slice loop acquisition and angular increment of 13.52°, shot TR of 1.5s, TR=21.1ms, flip angle(α)=15°. Veins were suppressed using a superior inversion RF pulse applied every 1.5s. Using computer vision techniques of template matching and mass-based tracking, blood flow velocity was quantified in 3D by analyzing in-plane and through-plane shifts in the MR signal between TE_1 and TE_3 on a voxel-by-voxel basis using custom in-house software. Local weighted averaging of resulting values was used to reduce intervoxel variability and compute mean blood flow velocity (MFV). Resolution-, coverage-, and time-matched standard 3D TOF was acquired with parameters: TR/TE/α=21.0ms/3.4ms/15°, GRAPPA=2, flow-compensation, BW=186Hz/pixel, TA=4min3s. Resolution- and coverage-matched 3D PC (PC_{HR}) with a similar TA (4min40s) was acquired with parameters: TR/TE/α =47.8ms/7.3ms/10°, GRAPPA=3, VENC=60cm/s, BW=440Hz/pixel. Contrast-to-noise ratio (CNR) was measured. qTOF and PC measures of MFV were compared using linear regression, intraclass correlation (ICC), and Bland-Altman analyses. Due to the low CNR of PC_{HR} which precluded its use in quantitative analysis, lower-resolution PC (PC_{LR}, 1.2×1.2×1.3mm^3 interpolated to 0.6×0.6×0.65mm^3) and medium-resolution PC (PC_{MR}, 0.85×0.85×1.30mm^3 interpolated to 0.43×0.43×0.65mm^3) were acquired in 10 and 5 subjects, respectively. qTOF was also compared to PC_{MR} in a helical 3mm diameter tubing phantom at continuous flow rates (60-180mL/min, 30mL/min increments).

Results: qTOF provided excellent agreement with PC_{MR} in the flow phantom (ICC=0.981, P<0.001), and with pumped MFVs (ICC=0.978, P<0.001). **Figure 1** shows the image quality of qTOF in comparison with resolution-matched standard TOF and PC_{HR}. qTOF TE_1 improved CNR with respect to PC (20.6±3.0 [mean±standard deviation] versus 11.5±2.2, P<0.001), while standard TOF provided the largest CNR (37.8±8.7, P<0.001 versus both qTOF and PC). The use of a stack-of-stars readout with qTOF eliminated misregistration artifacts from oblique in-plane blood flow that were seen with standard TOF (red arrow in Figure 1)[3]. The low CNR from PC_{HR} precluded its use for measuring MFV. Strong positive correlation (r=0.759, P<0.001) and good agreement (ICC=0.700, P<0.001) for MFV was found between qTOF and PC_{LR} (**Figure 2**) and PC_{MR}. **Figure 3** shows a MFV map obtained with qTOF.

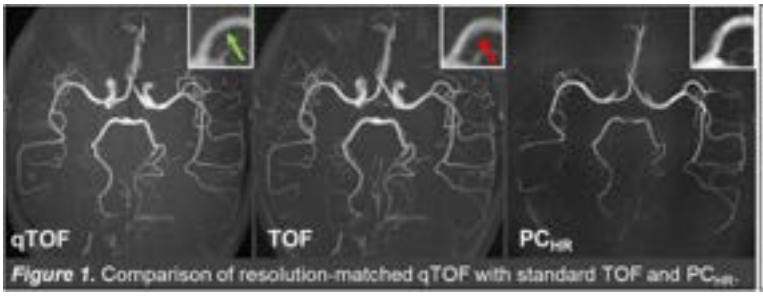

Figure 1. Comparison of resolution-matched qTOF with standard TOF and PC_{HR}.

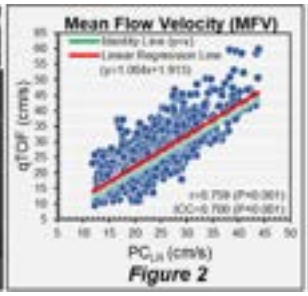

Figure 2

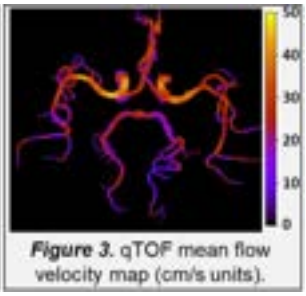
Figure 3. qTOF mean flow velocity map (cm/s units).

Discussion: We presented the new method of qTOF MRA for simultaneous luminal and hemodynamic evaluation of the intracranial arteries. Compared to standard TOF, the approach quantifies blood velocity in the intracranial arteries and eliminates artifacts from in-plane oblique blood flow. Compared to PC, qTOF nearly doubles CNR, supports the acquisition of higher spatial resolution, and shows good agreement with PC for mean cross-sectional blood flow velocity.

References: **1.** Masaryk TJ et al. *Radiology*. 1989;171:793-799. **2.** Koktzoglou I et al. *Magn Reson Med*. 2020;84 (6):3316-3324. **3.** Nishimura DG et al. *Magn Reson Med*. 1991;22:481-492.
Funding: NIH NIBIB 1R01EB027475.

Abstract ID: 45

Impact of loss function in phase-contrast MRI reconstruction using deep learning

[1]Gaël Touquet, [1,2]Loic Boussel, [1,2]Philipe Douek, [1]Monica Sigovan

[1] Univ Lyon, Université Claude Bernard Lyon 1, INSA-Lyon, CNRS, Inserm, CREATIS UMR 5220, U1294, F-69621, LYON, France

[2] Department of Interventional Radiology and Cardio-vascular and Thoracic Diagnostic Imaging, HCL, Lyon, France

Purpose: Phase-contrast (PC) MRI provides a non-invasive method for quantification of blood flow in the heart and vessels throughout the cardiac cycle, with particular impact in the exhaustive and early diagnosis of cardio-vascular diseases, such as for example congenital heart disease. Because of the need to encode displacement in the phase of the MR signal and to subtract at least 2 sequential acquisitions, PC MRI is even more time consuming than morphological MRI. Undersampling can be used to accelerate the time-consuming acquisitions, with a penalty on both image quality and quantitative information.

Deep learning techniques have shown significant potential in the MRI reconstruction problems [1]. The training stage, and therefore the resulting performance of a deep neural network, are both heavily driven by the choice of loss function, and should always be tailored to the needs of the task at hand. Therefore, we intend to estimate the impact of the choice of loss function in the training of convolutional deep learning approaches on the resulting reconstruction of flow in PC MRI.

Methods: We chose the U-net architecture [2] as a benchmark for this study, since it is the most widely used approach in image-based tasks.

Three separate trainings of this U-net architecture have been performed independently, one for each of the three selected loss functions. These loss functions are the mean square error (MSE), the mean absolute error (MAE), and the structural similarity index (SSIM) [3], as they are the most commonly used in image-based reconstruction.

The images used in the training and testing of the reconstruction were 2D PC-MRI acquisitions performed on a 1.5T Phillips system (Philips, Best, The Netherlands). Complex images were created using the morphological images as magnitude and flow images as phase. Acceleration is simulated by masking measurements in the kspace along variable density lines according to Lustig et. al. [4]. In the training phase, all 40 acquired cardiac phases are used independently from the 608 acquisitions, resulting in 24320 images. Complex values are separated into real and imaginary parts at each layer evaluation, and independent weights are applied.

The quality of the reconstructed flow images was quantified using the relative difference of flow in the vessel of interest. In order to evaluate the gain in clinical applications, vessels were manually segmented in systolic peak magnitude images in a similarly acquired validation dataset and the segmented regions are then used to compare the flow between the original phase contrast images and the obtained reconstructed images.

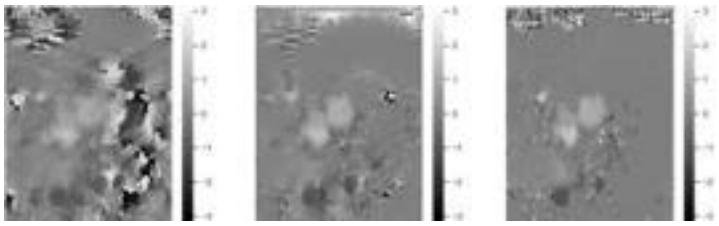

Figure 1 image of the undersampled (left), reconstructed (middle) and fully sampled (right) phase-contrast image used as the image phase (displayed here in radian) in the training for an acceleration of 2

Results: The whole approach is repeated for acceleration values of 2, 5 and 7. The obtained reconstructed flows are then compared to the fully sampled measured flow. The mean of the 300 ratios of reconstructed to fully sampled flows are detailed in table 1. An illustration of reconstruction with the SSIM for an acceleration of 2 is shown in fig 1. Indeed, it seems that the MSE gives best flow fidelity at low acceleration values, whereas the MAE seems best at high acceleration value.

Acceleration\Loss	MAE	MSE	SSIM
2	0.381	**0.355**	0.407
5	0.392	**0.347**	0.555
7	**0.532**	0.603	0.684

Table 1 Mean relative difference of the reconstructed flow for different accelerations for trainings with the three studied losses.

Discussion: The performance of the different losses shown here could help direct the design of a loss function specifically designed for phase-contrast reconstruction, which would ultimately out-perform the ones discussed here.

Funding: ANR-18-CE19-0025-01

References:

[1] -" Applications of deep learning to MRI images: A survey" Jin Liu et al. Big Data Mining and Analytics (Volume: 1, Issue: 1, March 2018) 10.26599/BDMA.2018.9020001

[2] -"U-net: Convolutional Networks for Biomedical Image Segmentation" O.Ronneberger,et al. arXiv:1505.04597

[3] - "Image quality assessment: From error visibility to structural similarity," Z. Wang, et al. IEEE Transactions on Image Processing, vol. 13, no. 4, pp. 600-612, avril 2004.

[4] - Lustig et. Al. 10.1002/mrm.21391

Abstract ID: 46

Assessing the mechanism of action of sodium-glucose co-transporter 2 inhibition using quantitative interleaved cardio-renal MRI: pre-treatment findings in SUGAR-DM-HF study

M.M.Y. Lee[1], S. Sourbron[2], R. Woodward[1], K.J.M. Brooksbank[1], P. Hall Barrientos[1], S. Allwood-Spiers[1], B. AlHummiany[3], S. Dobbin[1], K. Mangion[1], J.J.V. McMurray[1], P.S. Jhund[1], M.C. Petrie[1], C. Berry[1], P.B. Mark[1], G. Roditi[1], N. Sattar[1], A. Radjenovic[1]

[1]Institute of Cardiovascular and Medical Sciences, University of Glasgow and GGC NHS Trust, Glasgow, UK; [2]University of Sheffield, Sheffield, UK; [3]University of Leeds, Leeds, UK

Purpose: Multi-organ involvement is a hallmark of many chronic diseases, such as diabetes mellitus (DM), hypertension and heart failure (HF), as well as a prominent feature in both acute and long-term manifestations of infections such as COVID-19. Traditionally, clinical imaging focuses on a single organ assessment, due to multiple practical and technical constraints. We have designed a proof-of-concept interleaved cardio-renal MRI protocol to investigate the mechanism of action of sodium-glucose co-transporter 2 (SGLT2) inhibition in patients with HF and type 2 DM or prediabetes [1-2].

Methods: SUGAR-DM-HF (NCT03485092) is a single-centre, double-blind, placebo-controlled randomised clinical trial of empagliflozin in patients with HF (left ventricular ejection fraction ≤40%), type 2 DM or prediabetes, and an estimated glomerular filtration rate of ≥30 ml/min/1.73m^2 [3]. Interleaved cardio-renal dynamic-contrast enhanced (DCE) MRI was performed at baseline and 36-weeks, on a 3T clinical MRI system (Prisma, Siemens Healthcare). Dual-bolus DCE-MRI (**Figure 1**) was acquired using an imaging protocol described earlier [4]. A subset of 22 baseline pre-treatment scans were analysed, blinded to treatment allocation and date/time of scan: 14 males; age (years) range 54-86, median 73; BMI (kg/m^2) range 23.6 – 38.6, median 31.3. Image pre-processing, segmentation and motion correction were performed prior to pharmacokinetic modelling using PMI software [5]. Cardiac DCE was modelled using a 1-compartment model, and Renal DCE was fitted to a 2-compartment filtration model (**Figure 1**).

Results: A summary of myocardial and renal perfusion measurements is presented in **Table 1**. The table lists myocardial blood flow (MBF), renal blood flow (RBF) and regional Glomerular Filtration Rate (rGFR) estimates. A range of other parameters, including mean transit times (MTT) were also collected.

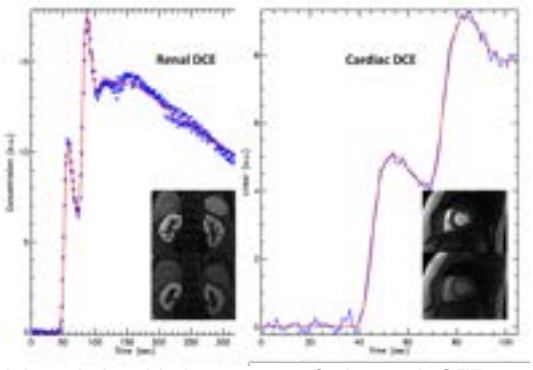

Figure 1. Illustrations of interleaved DCE time-series and model fits: 2-compartment filtration model (Renal) and 1-compartment pharmacokinetic model (Cardiac) derived from a single acquisition (pre-treatment scan in a 74-year old male patient). Insets represent wash-in and wash-out coronal renal and mid-ventricular short-axis cardiac image frames. MBF = 0.81 ml/g/min (corrected for cardiac work via rate pressure product, RPP), RBF = 211.9 ml/100ml/min, Blood MTT = 7.2 s.

We explored the relationship between perfusion and rGFR, and patient age and sex. There was a significant difference in MBF between males and females, with females having a significantly higher resting MBF (1.03 ± 0.22 vs 0.77 ± 0.18, P = 0.014, independent samples t-test). Both RBF and rGFR were significantly correlated with age (linear regression ANOVA P < 0.0001), with a steady decrease in both parameters with increasing age (**Figure 2**).

N = 22	Mean	SD
MBF [ml/g/min]	0.87	0.23
RBF [ml/100ml/min]	208.9	72.7
rGFR [ml/min]	13.4	6.7

Table 1. Summary of perfusion and filtration parameters.

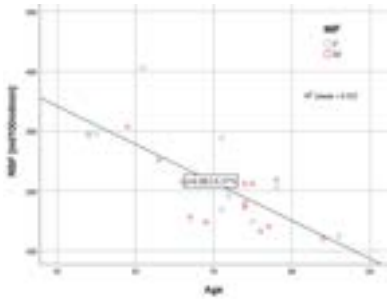

Figure 2. RBF regression against patient age.

Discussion: Baseline measurements of quantitative biomarkers of cardio-renal perfusion in the SUGAR-DM-HF study are in agreement with published values, where renal and cardiac components were acquired independently in separate scans. Myocardial perfusion at rest seems to be elevated in females, and there is a significant decline in renal blood flow and rGFR with age. The results of our proof-of-concept cardio-renal DCE-MRI study are encouraging, and we hope that the introduction of highly accelerated, undersampled and self-navigated sequences will lead to more widespread use of multi-organ quantitative MRI.

References: [1] Zinman et al. N Eng J Med 2015;373:2117-28; [2] Lee MMY et al. Arterioscler Thromb Vasc Biol 2020;40:506-22; [3] Lee MMY et al. Circulation 2021;143:516-25; [4] Lee M et al. SMRA 2018; [5]. Sourbron S et al. Magn Reson Mater Phy 2009;22:539.
Funding: Grant from Boehringer Ingelheim.
Acknowledgements: Glasgow Clinical Research Imaging Facility, Ann Wright, Joyce Thompson, Liz Coyle, Kanishka Sharma.

Abstract ID: 47

Simultaneous Multi-slice Cardiac MR Multitasking for Motion-Resolved, Non-ECG, Free-Breathing Joint T1-T2 Mapping

Xianglun Mao[1], Hsu-Lei Lee[1], Tianle Cao[1,2], Fei Han[3], Yibin Xie[1], Debiao Li[1,2], Anthony G. Christodoulou[1,2]
[1] Biomedical Imaging Research Institute, Cedars-Sinai Medical Center [2] Department of Bioengineering, UCLA
[3] Siemens Medical Solutions, Inc., Los Angeles, CA

Purpose: Quantitative myocardial T1 and T2 mapping techniques using cardiac magnetic resonance imaging (CMR) have been shown to be useful for assessing myocardial pathologies and characterizing tissue. CMR Multitasking[1] has shown promise for non-ECG and free-breathing T1-T2 mapping, for 2D single-slice[1] imaging in a 1.5 min scan and for 3D[2-3] volumetric imaging in 9 min or longer. Here we combine the CMR Multitasking framework with radial simultaneous multi-slice (SMS) acquisition[4-5] to perform cardiac-resolved T1/T2 mapping of basal, mid, and apical short-axis slices in a single non-ECG, free-breathing 3-min scan—roughly half the exam time of a conventional six-breath-hold sequence of three T1 slices followed by three T2 slices.

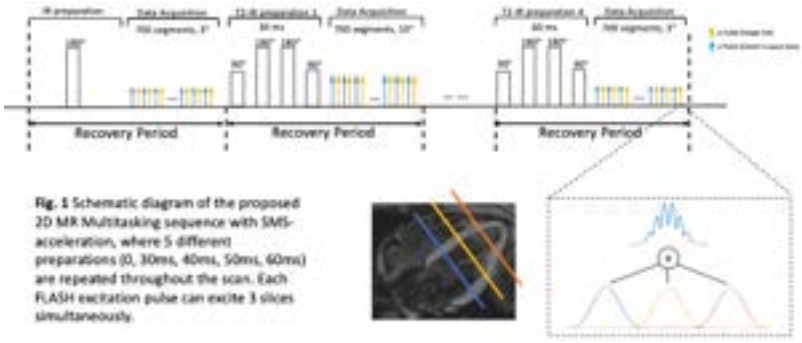

Fig. 1 Schematic diagram of the proposed 2D MR Multitasking sequence with SMS-acceleration, where 5 different preparations (0, 30ms, 40ms, 50ms, 60ms) are repeated throughout the scan. Each FLASH excitation pulse can excite 3 slices simultaneously.

Methods: *Sequence Design*: The proposed continuous 2D sequence uses a radial trajectory modified to collect low-rank tensor auxiliary data interleaved with image data. A golden angle (111.24°) angular increment was used between consecutive imaging readouts. A CAIPIRINHA-type phase modulation pattern was applied to the excitation pulses to achieve a multi-band factor of 3. The auxiliary data is acquired every other readout. Interleaved IR and T2-IR pulses are employed to generate the T1 and T2 contrasts (Fig. 1). FLASH excitations alternate between 3° and 10° to allow B1+ mapping, characterizing the Look-Locker effect during T1 mapping[6].

Data Collection: Five healthy consenting volunteers (2 males, 25±1.4 yrs; 3 females, 44±6.1 yrs) were imaged on a 3T scanner (MAGNETOM Vida, Siemens Healthcare, Erlangen, Germany). Multitasking pulse sequence parameters were FA=3° and 10°, TR/TE=3.5 ms/1.7 ms, recovery period = 2.5 s, FOV=270x270mm^2, spatial resolution=1.7x1.7, slice thickness=8 mm^3, 3 slices, scan time=3 min, 20 cardiac bins, 6 respiratory bins. Reference 2D T1 maps with MOLLI and 2D T2 maps with T2-prep FLASH (spatial resolution=1.4x1.4x8 mm^3) were acquired at both systole and diastole using an end-expiration breath-hold.

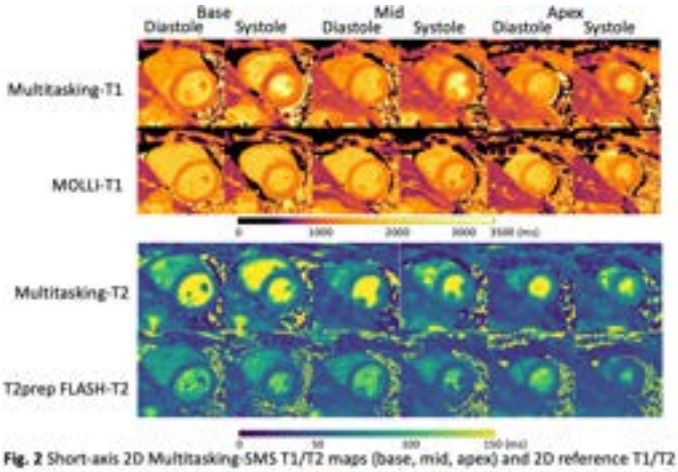

Fig. 2 Short-axis 2D Multitasking-SMS T1/T2 maps (base, mid, apex) and 2D reference T1/T2 maps (base, mid, apex) of the same volunteer (F, 46).

Results & Discussion: Diastolic and systolic T1 and T2 mapping results from one subject are shown in Fig. 2, and the AHA segment plots across all five subjects are shown in Fig. 3. The Multitasking T1 maps reported slightly higher myocardial T1 values (1349±135 ms) than the MOLLI T1 maps (1249±39 ms), which are known to underestimate T1. Regional image noisiness increases the standard deviation of the Multitasking T1 values in the myocardium. The Multitasking T2 maps reported a slightly higher range of myocardial T2 values than the T2-prep FLASH T2 maps. The myocardial T2 values are 47.4±3.2 ms and 43.7±2.4 ms, respectively.

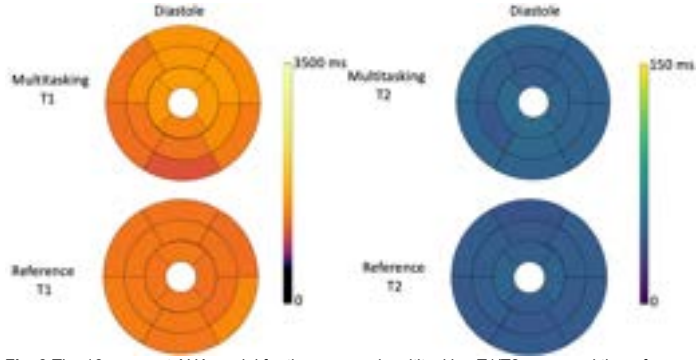

Fig. 3 The 16-segment AHA model for the proposed multitasking T1/T2 maps and the reference T1/T2 maps in the myocardium in all 5 scanned subjects.

Conclusions: Co-registered T1 and T2 maps were simultaneously acquired at base, mid, and apex slices using an SMS accelerated Multitasking technique in a 3-min MRI scan. The myocardial T1, T2 quantification showed slight bias compared to reference MOLLI and T2-prep FLASH measurements, but were still in the reported normal range. This method shows potential for reducing exam time for quantitative CMR without ECG or breath-holds.

References: [1] Christodoulou, A.G. et al. Nature BME. 2018; [2] Mao, X. et al. SCMR. 2020; [3] Mao, X. et al. ISMRM. 2021; [4] Weingärtner, S. et al. MRM 2017; [5] Ye, H. et al. MRM 2017; [6] Serry F, et al. ISMRM 2020.

Abstract ID: 48

What's Wrong with our MRAs? The Lightbulb Moment!

Rosario Lopez[1,3], Laura Petrie[2], and Giles Roditi[2,4]

1 Clinical Physics and Bioengineering, NHS Greater Glasgow and Clyde, UK, 2 Radiology, NHS Greater Glasgow and Clyde, UK, 3 Institute of Neurosciences and Psychology, University of Glasgow, UK, 5 Institute of Cardiovascular and Medical Sciences, University of Glasgow, UK

Situation: November 2020 a reduction in image quality is flagged by radiographic and radiology staff for our Siemens Avanto 1.5T scanner, this particularly affected CE-MRA with a drastic drop in SNR for time-resolved imaging in particular, effects were less obvious for other MRI scans. MRI Physics and the manufacturer engineers were involved in troubleshooting these phenomena. MRI Coils were tested and were all within expected values, several equipment parts were changed (such as sockets) yet the problem persisted, hence we abandoned using this scanner for CE-MRA examinations for several months attributing the problem to the age of the scanner (nearly 13 years old). However, eventually the lights within the scan room were suspected and tests were carried out with lights on and off from which we traced the issue to new energy-efficient LED lights used to replace previous halogen units. We managed to source halogen bulbs and CE-MRA on the scanner was eventually reinstated as of May 2021.

Background: Energy saving LEDs are now commonplace as a result of European Union directive (EC 244/2009) and Commission Delegated Regulation (EU) No 874/2012 supplementing Directive 2010/30/EU which led to the phasing out from 2018 of incandescent bulbs. To investigate the impact this episode had on our MRA image quality we retrospectively reviewed MRA scans carried out during the period that our MRI scanning room had LED lights.

Assessment: Examples of image quality issues are provided below - a renal MRA plus a base image from a TWIST series performed for the calves showing marked generalised image noise.

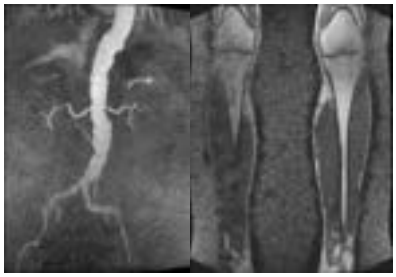

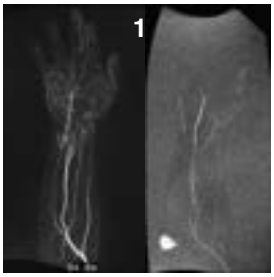

Additionally, two patients were identified who had had exactly the same MRA protocol before and during the LED period. In both cases the patient pathologies were largely unchanged but there was a drastic drop in SNR with general increase in image noise and clear degradation of image quality. Case 1: 39 year old male, forearm arteries with SNR values calculated as 67 and subsequently 11.5 (2017/2020). Case 2: 62 year old male, lower limb arteries with SNR values calculated as 60.5 and subsequently 39.3 (2014/2020).

Discussion: The commonest issue with scan room bulbs is the 'Zipper' artifact, where low frequency RF from a flickering incandescent bulb results in spikes in images. Energy-efficient compact fluorescent lights (CFLs) have also been recorded as culprit for this type of artifact, similar to the issues that occur with imperfection in the Faraday shield or an incompletely closed cabin door allowing RF leak. However, a drastic drop in SNR with specific sequences in relation to LEDs has not been previously reported. LEDs have been primarily designed for reduced energy consumption and longer life, however these new designs are not simply bulbs and need dedicated internal driver integrated circuitry, this may be very sophisticated and can vary significantly between manufacturers.

LED

Halogen

Conclusions: A drastic drop in SNR for CE-MRA with propagated image noise can be caused by energy-efficient LEDs, presumably related to resonances generated in ac/dc converter or driver circuitry. By reinstating halogen bulbs the issue has been temporarily solved in our institution, however further work will need to be undertaken to determine whether there are energy-efficient LEDs that can be used with our MRI systems going forward.

Abstract ID: 49

Non-rigid Motion-compensated Whole-heart 3D T2 mapping in a hybrid PET-MR

Alina Psenicny[1], Camila Munoz[1], Alina Hua [1], Karl P Kunze[2], Radhouene Neji[1,2], René M Botnar[1], Claudia Prieto[1]
[1]School of Biomedical Engineering and Imaging Sciences, King's College London, London, United Kingdom
[2]MR Research Collaborations, Siemens Healthcare Limited, Frimley, United Kingdom

Purpose: Quantitative T2 mapping and simultaneous ^{18}F-FDG PET-MRI has shown promise for improved diagnostic accuracy of inflammatory cardiac diseases, such as cardiac sarcoidosis[1]. However, respiratory motion and mis-registration between free-breathing 3D PET and conventional 2D breath-held MRI remain challenges when interpreting imaging findings, hindering clinical adoption of this technique. Here we introduce and evaluate an efficient (accelerated and non-rigid motion-compensated) free-breathing 3D whole-heart T_2-mapping sequence, which provides myocardial inflammation characterisation and non-rigid respiratory motion fields to correct simultaneously acquired PET data in a 3T hybrid PET-MR system. This is achieved by extending a previously introduced approach for 3D translational motion-corrected T_2 mapping at 1.5T[2]. Preliminary evaluation is performed in 8 healthy subjects and 8 patients with suspected cardiovascular disease for MR-only acquisitions at 3T.

Methods: Free-breathing 3D whole-heart T_2-mapping was implemented on a PET-MRI system. Three datasets with different T_2-preparation pulses (0, 28 and 55 ms) are acquired using a 3-fold undersampled variable-density Cartesian trajectory[3]. The sequence includes a saturation pulse in each heartbeat to render it heart-rate insensitive and a fat saturation pulse (Fig1). Beat-to-beat translational motion is estimated from 2D image navigators (iNAVs)[4] (foot-head and right-left directions) and virtual 3D (v3D) iNAV based on autofocus[5,6] (right-left and anterior-posterior direction), and used to motion-correct and bin the MR data and produce respiratory-resolved 3D images. 3D non-rigid motion is then estimated and incorporated into a motion-compensated reconstruction[7] with patch-based low-rank regularization[8]. T_2-maps are computed using dictionary,-matching[9]. The approach was tested in phantom, 8 healthy subjects and 8 patients (Biograph mMR, Siemens Healthcare). Relevant parameters include: coronal orientation, FOV=312x312x60-72 mm, 1.5 mm^3 isotropic resolution, TR/TE=3.45/1.57 ms, FA=15°, acquisition time = 9.3±1.1 min. The proposed technique was compared against the spin echo reference (phantom) and conventional 2D T_2 mapping (healthy subjects and patients).

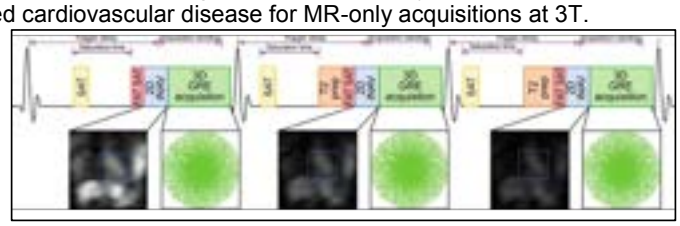

Fig.1 3D free-breathing T_2 mapping pulse sequence diagram including three T_2 preparation pulses, saturation pulse and fat saturation. 2D iNAVs are acquired for translational motion estimation and correction.

Results: Phantom results show high correlation of the proposed approach with gold standard 2D T_2-mapping (R^2=0.996). Repeatability studies were performed acquiring 2 datasets on 3 consecutive days. T_2 values for all 6 acquisitions of the repeatability study had an average standard deviation of ±0.98ms. In-vivo 3D T2 septal myocardium values estimated with the proposed approach in healthy subjects (40.1±1.3ms) and patients (healthy tissue) (40.5±3.1 ms) are in good agreement with those measured using conventional 2D T_2 mapping (healthy=39.7±1.3ms, patients=40.3±2.2 ms) (Fig.2.a). Improvements due to v3D iNAV motion correction can be observed in comparison to no motion correction and 2D iNAV based non-rigid motion correction (Fig.2.b).

Discussion: We introduce a method for good quality high-resolution 3D T_2 maps at 3T from an efficient scan of ~10 min. Furthermore, the proposed approach provides non-rigid motion fields to correct both the MRI and PET data to the same motion position, enabling direct fusion of both datasets for analysis and interpretation. Future studies will evaluate the proposed method in patients with cardiac sarcoidosis undergoing PET-MRI.

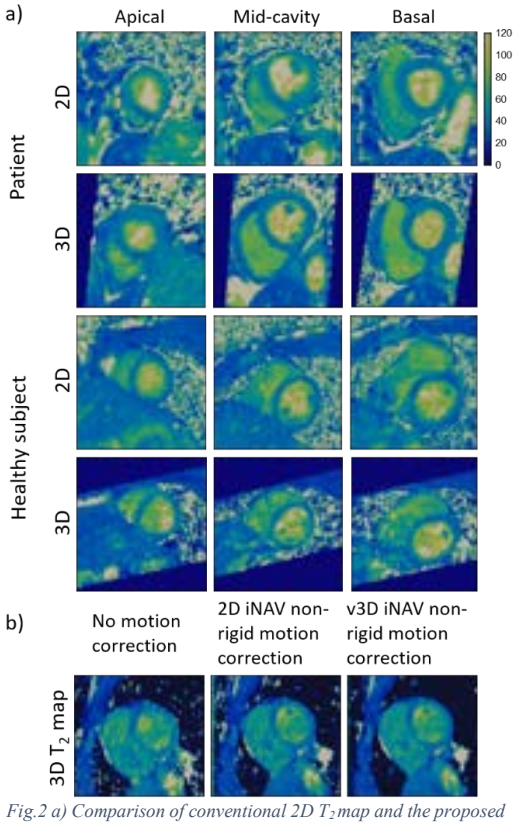

Fig.2 a) Comparison of conventional 2D T_2 map and the proposed 3D T_2 map for a patient (top) with suspected acute myocarditis and a healthy subject (bottom). Good agreement with clinical reference is observed. b) 3D T2 mapping with different respiratory motion correction strategies. No motion correction, 2D iNAV non-rigid motion correction and virtual 3D iNAV non-rigid motion correction are shown here. Improved image quality can be observed with 2D iNAV non-rigid motion correction and further improvements with the proposed virtual 3D iNAV non-rigid motion correction.

References:

1. Birnie, D. H. *et al. JACC.* 68, 411-421 (2016). 2. Bustin, A. *et al. MRM.* 83,988-1002 (2020). *3.* Prieto, C. *et al. JMRI* 41, 738–746 (2015). 4. Henningsson, M. *et al. MRM.* 67, 437–445 (2012). 5. Atkinson, D., *et al.* IPMI 1997. *Lecture Notes in Computer Science,* vol. 1230, 341–354. 6. Psenicny, A *et al.* ISMRM2021 7. Batchelor, P. G. *et al. MRM.* 54, 1273–1280 (2005). 8. Bustin, A. *et al. MRM.* 81, 3705–3719 (2019). 9. Weigel, M. JMRI. 41, 266-2.95 (2015).

Abstract ID: 50

Decomposition-Recomposition: Memory Efficient Deep Learning Reconstruction for High Resolution, 3D, Non-Cartesian Pulmonary Magnetic Resonance Angiography (MRA)

Zachary Miller[1], Kevin M. Johnson[1,2]

University of Wisconsin-Madison, Departments of [1]Medical Physics and [2]Radiology

Purpose: Fully 3D non-Cartesian acquisitions offer many benefits over traditional Cartesian methods as they efficiently sample k-space in all dimensions, offer intrinsic motion and flow robustness, and allow ultrashort echo times. For these reasons, 3D non-Cartesian sampling is being developed for highly accelerated 4D-flow acquisitions and free breathing pulmonary MRA. One barrier, however, to the clinical adoption of these techniques is the need for lengthy compressed sensing (CS) iterative reconstructions even when run on graphical processing units (GPUs) (4).

Deep Learning (DL) based on unrolled loops offers the potential for reconstructions which significantly reduce reconstruction time and outperform CS reconstructions, as has been demonstrated for under-sampled Cartesian acquisitions (1). These methods, however, have seen limited application to the fully 3D non-Cartesian setting due to GPU memory limitations. Unlike volumetric Cartesian acquisitions and trajectories like stack of spirals that can be decoupled into 2D sub-problems and trained patch-wise, fully 3D non-Cartesian trajectories require the complete 3D volume for data-consistency (3). This means in the unrolled setting that the entire 3D volume must be passed through the DL regularizer prior to data-consistency during training. For high resolution acquisitions, this requirement makes reconstructions using standard neural network (NN) regularizers unable to fit on even state of the art GPU cards.

In this work, we investigate an unrolled DL reconstruction method, denoted decomposition-recomposition, that makes these high resolution, fully non-Cartesian reconstructions feasible on standard GPUs. For a single unroll, we decompose the input volume into a series of slabs, push each slab iteratively through the denoising network, and then rebuild the denoised volume for data-consistency all during training. In place of traditional backpropagation, where all slabs and their associated NN steps would be saved in memory during the forward pass (meaning no net memory savings compared to passing the full volume through the network), we use gradient checkpointing which recomputes intermediate network steps during backpropagation rather than saving them in memory (2). Maximum GPU memory burden then becomes proportional to the size of a single slab rather than proportional to the full volume.

We apply decomposition-recomposition to reconstruction of highly under-sampled (R=7), high resolution (280x280x280) pulmonary MRA datasets on a single 16 GB V100 GPU as proof of concept. We show that our method reduces reconstruction time by 18 fold and results in improved PSNR when compared to conventional CS methods.

Methods, *Algorithm Pipeline:* We unroll a supervised DL algorithm iterating between a NN regularizer (residual network, 32 channels/conv) and SENSE non-uniform Fast Fourier transform (NUFFT) data consistency term. We use three unrolls, and train end to end in a supervised fashion using mean-square-error loss between the network output and (effectively) fully sampled data. The model is implemented in Pytorch with NUFFT from Sigpy (5) and trained using a 16 GB V100 GPU. One unroll of our reconstruction involves the following steps during the forward pass (gradient checkpointing used for all steps):

1. **Volume Decomposition:** decompose p x p x p zero-padded input volume into set of m x n x o slabs.
2. **Denoising:** Iteratively pass slabs one by one through the denoising network. GPU memory reduction relative to passing the full volume through the network then is proportional to mno/p^3 for a single unroll.
3. **Recomposition:** Slabs are then stitched back together into the full volume. Zero padding at block edges means that passing the volume block-wise through the network is not equivalent to passing the whole volume through the network. We correct for these artifacts by passing a second set of blocks through the network with each new block centered at the edges of the original blocks. We then replace the edge artifacts with the center of denoised new blocks.
4. **Data Consistency:** The corrected volume is then passed to a (NUFFT) data-consistency step.

Training Data/Evaluation: We acquired 32-channel radial, pulmonary MRA volumes in five healthy volunteers during free breathing on a 3.0 T GE (Waukesha, WI) scanner. Data sets were coil compressed to 20 channels, and then binned using respiratory bellows signal. End expiratory phase volumes were reconstructed using the adjoint NUFFT, and then retrospectively under-sampled (R=7). Three cases were used for training, one case each was used for validation and testing. We compared decomposition-recomposition to L1 wavelet CS reconstruction (100 iterations, implemented in Sigpy, ran on V100 GPU) based on reconstruction time and PSNR.

Results/Discussion: Decomposition-Recomposition results in significantly faster reconstructions (81 s vs. 1481 s) with higher PSNR values (34.10 dB vs. 31.62 dB) than offered by conventional CS reconstructions. To our knowledge, this is the first time high resolution, fully non-Cartesian datasets have been reconstructed using unrolled DL methods. We note that if the full volume was used for training rather than the decomposition-recomposition method, a single unroll would require at least 85 GB of GPU memory. Here, we use a single 16 GB GPU for multiple unrolls. For future work, we plan to extend this work to 4D respiratory binned and time-resolved reconstructions. Figure 1 demonstrates example test results:

Figure 1: Representative coronal slices from zero-filled, CS and NN recons compared to fully sampled slice

References: 1.Sandino et.al., ISMRM 2020, 2. Sohoni et al. Preprint, 3.Ong et. al. MRM 2020, 4.Ong et al. Trans. Med. Imag. 2019, 5.Ong et. al. Sigpy

Abstract ID: 51

Carotid atherosclerosis is associated with brain infarcts and cognitive decline.

Niranjan Balu[1], PhD, Duygu Baylam Geleri[1], MD, Daniel S Hippe[1], MS, Gador Canton[1], PhD, Jie Sun[1], MD, Thomas Hatsukami[2], MD, Chun Yuan[1], PhD

1. Department of Radiology, University of Washington, Seattle, USA; 2. Department of Surgery, University of Washington, Seattle, USA

Purpose: Carotid atherosclerosis can lead to cognitive decline by causing brain infarction secondary to thromboembolism from unstable carotid plaque components (1). However, the relationship between the different carotid plaque components, brain infarcts and resultant effects on cognition are yet to be studied.

Aim: To investigate the relationship between carotid atherosclerosis, brain infarcts and cognition.

Table 1: Correlation of carotid morphology and composition with brain lesions and MoCA

	Brain Infarct Volume (N=33) (Ipsilateral)		Brain Infarct Volume (N=33) (Whole Brain)		MoCA (N=32)	
Variable	**r***	**P-value**	**r***	**P-value**	**r***	**P-value**
Mean NWI	0.26	**0.048**	0.14	0.44	-0.18	0.32
Mean WT	0.23	***0.076***	0.24	0.18	-0.11	0.53
Max WT	0.31	**0.017**	0.25	0.16	0.09	0.62
Calcium % volume	-0.14	0.29	-0.24	0.17	-0.36	**0.046**
LRNC % volume	0.29	**0.029**	0.34	0.053	-0.07	0.69
IPH % volume	0.25	***0.062***	0.29	0.10	-0.10	0.60

* Spearman's rank correlation coefficient. NWI: normalized wall index, WT: wall thickness, LRNC: lipid-rich necrotic core, IPH: intraplaque hemorrhage. Significant p-values bolded, trending p-values bolded and italicized.

Methods: 33 subjects with >15% carotid atherosclerosis by duplex ultrasound underwent carotid and brain MRI after informed consent. Carotid MRI for measurement of plaque burden and plaque composition included 3D-TOF, 3D-MERGE (pre- and post-gadolinum contrast) and 3D SNAP. Structural brain MRI scans included 3D-TOF, 2D T1w, FLAIR and DWI. Contours of carotid lumen, outer wall and plaque components (lipid-rich necrotic core (LRNC), calcification and intraplaque hemorrhage (IPH) were drawn by a reviewer and an experienced peer reviewer. Brain infarcts were contoured independent of carotid MRI by a reader with over seven years of brain review experience. Quantitative plaque burden measurements (mean/max wall thickness (WT) and normalized wall index (NWI, wall area normalized by outer wall area)) and plaque compositional measurements (percent volume of each component) were derived from the contours. Carotid atherosclerosis score (CAS) indicating unstable carotid lesion (2) was also calculated. Volume of brain cortical infarcts was measured. Montreal Cognitive Assessment score (MoCA) was assessed for each participant. The association of quantitative plaque metrics, brain infarcts (presence and volume) and MoCA score was assessed using R statistical software.

Table 2: Comparison of brain lesions by unstable carotid lesion score

		Unstable Carotid Lesion		
Variable		**Present**	**Absent**	**P-value***
Brain infarct (ipsilateral)	Present	5/22 (23%)	2/36 (6%)	***0.092***
	Number	1.1 ± 2.3	0.2 ± 1.2	***0.061***
	Volume	77.4 ± 237.4	11.3 ± 65.4	***0.058***
Brain infarct (whole brain)	Present	5/16 (31%)	3/17 (18%)	0.44
	Number	1.6 ± 2.6	0.6 ± 1.9	0.33
	Volume	106.5 ± 275.0	24.6 ± 94.9	0.30

*Wilcoxon rank-sum test or Fisher's exact test.

Results: 1) Carotid morphology and plaque composition correlate with brain infarcts on the same side (Table 1): Increasing mean NWI was associated with larger ipsilateral brain infarcts. Maximum WT showed a similar trend (significant p-values bolded, trending p-values bolded and italicized). These results suggest that larger carotid plaque size is associated with larger ipsilateral brain infarcts. Among plaque components, increasing percent LRNC (p=0.029) and IPH volume (p=0.062) were associated with larger ipsilateral infarct size. The ipsilateral association suggests that the brain infarcts may be caused by thromboembolism from upstream carotid plaque.

Carotid plaque composition is associated with poor cognition (Table 1): Mean time interval between MoCA and MRI was 144 days (range: -144 to 371 days). Larger calcification was associated with poor MoCA scores suggesting that subjects with more advanced carotid plaque composition have worse cognition.

Unstable carotid plaque composition is associated with ipsilateral brain infarcts (Table 2)): When examining carotid plaques based on the presence of unstable plaque components as indicated by the CAS score (lipid rich necrotic core > 40% of wall volume, presence of IPH or disrupted lumen surface) brain infarcts were more common when there were ipsilateral unstable carotid plaques than without.

Conclusion: Larger carotid plaques and unstable carotid plaque components are associated with larger ipsilateral cortical brain infarcts suggesting that unstable carotid plaques are causative of brain infarcts. Furthermore, more advanced carotid plaque composition is also associated with worse cognition. Larger studies are warranted to examine these association of carotid atherosclerosis, clinical/silent brain infarcts, and cognitive function.

References: 1) Bayer-Karpinska A et al, BMC Neurol. 2013; 13:201. doi: 10.1186/1471-2377-13-201, 2) Underhill et al, AJNR. 2010 Jun-Jul; 31(6): 1068–1075. doi: 10.3174/ajnr.A2007

Abstract ID: 52

Free-Breathing, Multiple Overlapping Thin-Slab Stack-of-Stars Balanced Steady-State Free-Precession MR Angiography: a Non-contrast Alternative to CT Angiography for TAVR Planning

Bradley D. Allen, MD, MS[1]; Ioannis Koktzoglou, PhD[2,3], Jianing Pang, PhD[4]; Robert R. Edelman, MD[1,2]
[1]Radiology, Northwestern University Feinberg School of Medicine, Chicago, IL, USA; [2]Radiology, Northshore University Health System, Evanston, IL, USA; [3]Radiology, Pritzker School of Medicine, University of Chicago, Chicago, IL, USA; [4]Siemens Medical Solutions USA Inc., Chicago, IL, USA.

Purpose: Patients undergoing transcatheter aortic valve replacement (TAVR) require high-quality diagnostic imaging of the aortic valve and vasculature to size the valve prosthesis and ensure appropriate vascular access. This task is usually performed with contrast-enhanced CT angiography (CTA). However, due to multiple comorbidities related to their aortic valve disease including poor renal function, there are frequent requests for "low contrast dose" CTA. Along with potential breath-holding artifacts, this approach can limit diagnostic quality. Free-breathing, non-contrast MRA techniques have the potential to be an alternative to CTA in a subset of TAVR patients, but historically have suffered from relatively poor spatial resolution, inadequate SNR, or motion artifacts, especially at the aortic root. In this study, we explored the use of a highly accelerated multiple overlapping thin-slab stack-of-stars balanced steady-state free-precession (tsSOS-bSSFP) acquisition for thoracic MRA in TAVR patients. We hypothesized that tsSOS-bSSFP would provide similar aortic annulus measurement to standard TAVR-planning CTA.

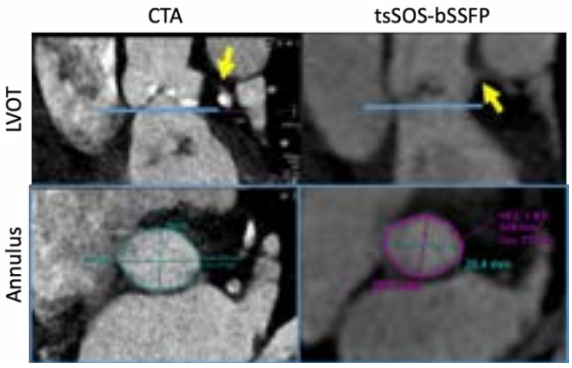

Figure 1: Left ventricular outflow tract (LVOT) and annulus views of TAVR planning CTA and tsSOS-bSSFP showing comparable image quality. Blue line: annular plane, yellow arrow: left main coronary artery

Methods: Patient recruitment: In accordance with an IRB-approved protocol, potential subjects were identified in collaboration with our hospital TAVR team and prospectively enrolled to undergo research MRA within 3 months of their standard of care TAVR planning CTA. tsSOS-bSSFP MRA: The prototype navigator-gated tsSOS-bSSFP sequence was acquired using a clinical 1.5T scanner (MAGNETOM Avanto Dot, Siemens Healthcare, Erlangen, Germany) with 9 overlapping thin slabs, 3D slice thickness = 0.9mm, sampling bandwidth = 1420 Hz/px, 2 shots, fat suppression, and T2 prep during end-diastole. The field of view was optimized for coverage of the aortic root. Acquisition time was approximately 2 minutes. Image Quality: Overall image quality was graded as 3 – excellent, 2 – diagnostic, 1 – poor, or 0 – non-diagnostic by an experienced cardiovascular radiologist based on ability to resolve the coronary arteries and generate acceptable MPR images for TAVR measurements.

TAVR Measurements: Following reconstruction, tsSOS-bSSFP images were loaded into dedicated measurement software (Vitrea, Vital Images, Inc., MN, USA). Using standard TAVR measurement procedures, the aortic annulus was identified and visualized in double-oblique orientation to the left ventricular outflow tract centerline by an experienced cardiovascular radiologist (Figure 1). The maximum aortic diameter and annular area were measured manually. The same measurements were performed on CTA by a single dedicated technologist as a part of the clinical workflow.

Statistics: Diastolic maximal diameter and annulus area were each compared group-wise between CTA and tsSOS-bSSFP using paired t-tests. Bland-Altmann analysis was also performed for both measures.

Results: A total of n=7 patients were recruited (age: 76.1 ± 6.6 years, M|F: 3|4). Overall image quality of tsSOS-bSSFP was 2.7 ± 0.5. A total of 5 exams were scored as "excellent" quality, and the remainder were scored as "diagnostic." There was no difference between CTA and tsSOS-bSSFP for maximal aortic annular dimension (30 ± 4 mm vs. 30 ± 4 mm, p = 0.94) or annulus area (538 ± 182 mm^2 vs. 559 ± 200 mm^2, p = 0.84). Bland-Altman analysis (Figure 2) demonstrated minimal bias and narrow limits of agreement for maximal diameter measurements (mean difference: 0.14 [-1.2, 1.5] mm). There was a slight bias towards increased area with tsSOS-bSSFP (mean difference: 21 [-66, 24] mm^2].

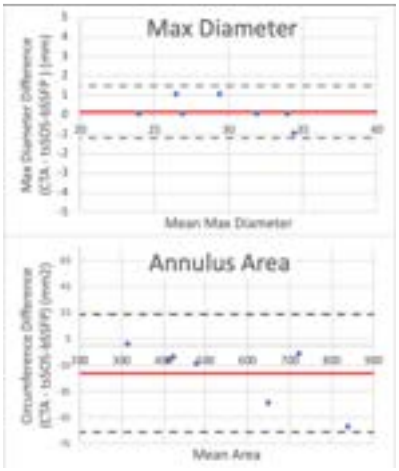

Figure 2: Bland-Altman Analysis.

Discussion and Conclusions: Our initial results suggest that free-breathing, multiple overlapping thin-slab tsSOS-bSSFP MRA provides high image quality and acceptable diastolic TAVR measurements at the aortic annulus in patient undergoing TAVR planning. Further analysis is ongoing to assess the performance for measuring other TAVR parameters such as coronary heights as well as determining correction factors for systolic phase sizing. The slight bias toward larger circumference is of uncertain clinical significance at this time, but future work will determine if this degree of difference impacts device selection.

Abstract ID: 53

4D Flow MRI of Porcine Pulmonary Hypertension Induced via Pulmonary Vein Banding

D. Seiter[1], B. Allen[2,3], DM. Tabima[3], TA. Hacker[4], TH Oechtering[5], NC. Chesler[6], and O. Wieben[1]

[1]Department of Medical Physics, [2]Department of Surgery, [3]Department of Biomedical Engineering, [4]Department of Medicine, [5]Department of Radiology, University of Wisconsin-Madison, Madison, WI, [6]Edwards Lifesciences Center for Advanced Cardiovascular Technology and Department of Biomedical Engineering, University of California-Irvine, Irvine, CA

Purpose: Pulmonary hypertension (PH) is a common consequence of left heart failure (PH-LHF) but can also occur due to PV narrowing.[1,2] As the disease progresses from isolated post-capillary to combined post- and pre-capillary PH (CPC-PH), mortality rate rises due to right heart failure. CPC-PH is diagnosed by elevated mean pulmonary artery pressure (mPAP), pulmonary capillary wedge pressure, and pulmonary vascular resistance (PVR). In this pilot study, we use 4D flow MRI to assess a novel porcine model of severe PH due to PV narrowing, aiming to characterize the vascular effects of CPC-PH in the lungs and the right heart.

Methods: Pulmonary vein banding (PVB) surgery[3] was performed on two large white male pigs (48kg, 56kg) using a non-occlusive banding of the inferior pulmonary venous confluence. A sham operation without band placement was performed on another male pig of similar weight (56kg). After 16 weeks, each pig was scanned using cine bSSFP for cardiac function, CE MRA for vascular anatomy, and radially undersampled 4D flow MRI.[4] (3.0 T MRI scanner [GE Healthcare Discovery MR750, Waukesha, WI], TR=6.3ms, TE=2.1ms, Isotropic Resolution=1.95mm^3, tip=8^o, Total Scan Time=13min) Cut planes were placed to measure velocities and flow in the vessels of interest using Ensight (Ansys, Canonsburg PA) and quantified using custom software in Matlab. (Mathworks, Natick MA) Flow path line visualizations were also created using Ensight. Cardiac pressures were invasively measured via right heart catheterization within hours of the MRI exam.

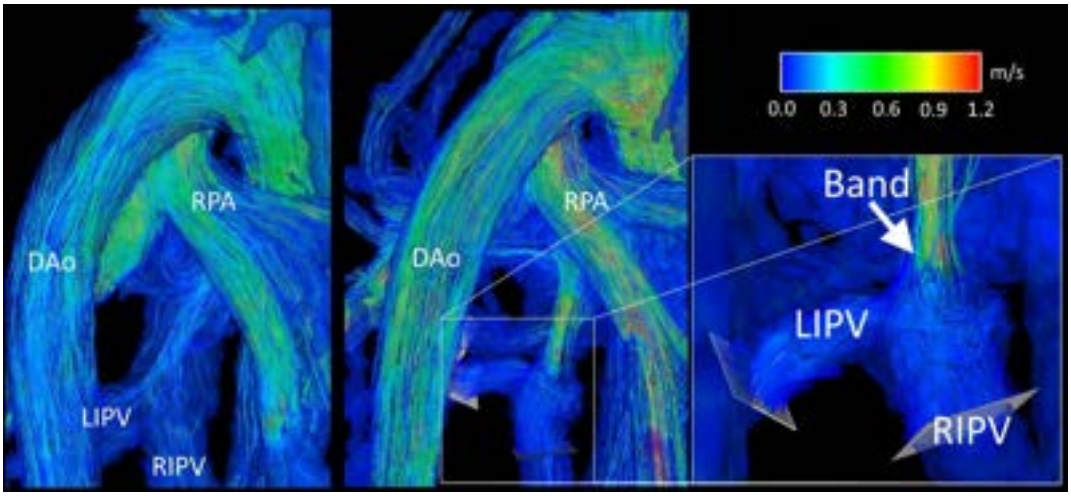

Figure 1: Side by side pathline visualization of Sham (left) and PVB1 (right, with band inset). Descending aorta (DAo), Right Pulmonary Artery (RPA), and Left and Right Inferior Pulmonary Veins (LIPV, RIPV) are labelled for reference. Band placement is shown.

Results: Flow pathline visualization for PVB1 and Sham is shown in Figure 1, with an inset highlighting the band. Velocities in the banded region of PVB1 reached peaks equivalent to the right and left pulmonary arteries and ascending aorta. The banded animals developed severe PH quantified by mPAP compared with the sham. Quantification of 4D Flow MRI after PVB shows dramatic reductions in inferior pulmonary vein (IPV) flow. PVB1 was banded at the confluence of left and right inferior pulmonary veins (LIPV, RIPV), while the PVB2 had a band placed on the RIPV alone. Compensatory flow through the LIPV was observed in PVB2.

	IPVs Mean Flow (L/min) (right, left)	IPVs Peak Velocity (cm/s) (right, left)	MPA Mean Flow (L/min)	RV EF (%)	mPAP (mmHg)	PVR (mmHg-min/L)
PVB 1	0.44, 0.43	10.8, 11.6	2.94	28.7	51	11.00
PVB 2	0.13, 1.23	16.3, 40.2	2.40	63.3	30	2.20
Sham	1.3, 0.87	31.4, 23.5	4.50	65.0	19	1.74

Discussion: In this study, we used 4D flow MRI in a novel porcine model of severe PH due to PV narrowing. 4D Flow MRI provided noninvasive measurement of blood flow and velocity in the vessels of interest, confirming success of the difficult surgical procedure and offering insight into the progression of PH due to PV narrowing independent of LHF. Future work will increase the number of subjects and further characterize and quantify the impact of increased pulmonary venous pressure on pulmonary vascular and right heart function.

References: 1. Assad TR, *J Am Coll Cardiol*. 2016;68(23):2525-2536. 2. Noordegraaf AV, Pulmonary hypertension. doi:10.1183/16000617.0096-2015 3. Pereda D, *J Cardiovasc Transl Res*. 2014;7(5):494-506. Johnson KM, *Magn Reson Med*. 2008;60(6):1329-1336.

Abstract ID: 54

A Deep Learning-Based Approach to Identify Patients without Myocardial Scar to Reduce Unnecessary Gadolinium Administration in Cardiac MRI

Ahmed S Fahmy[1], Ethan J Rowin[2], Talal Al-Otaibi[1], Martin S Maron[2], Reza Nezafat[1]

[1] Department of Medicine, Beth Israel Deaconess Medical Center and Harvard Medical School, Boston, MA
[2] Hypertrophic Cardiomyopathy Center, Tufts Medical Center, Boston, MA

Background and Purpose: Nearly 50% of non-ischemic cardiomyopathy patients undergoing gadolinium (Gd) based imaging cardiac MRI have no myocardial scar. Identifying these patients prior to Gd injection can reduce costs and improve scan efficiency and safety by minimizing use of unnecessary Gd administration. In this study, we test the hypothesis that deep convolutional neural network (CNN)-based analysis of *non-Gd* cine MRI images can allow accurate identification of patients without scar.

Methods: We retrospectively collected MRI datasets for 759 hypertrophic cardiomyopathy patients. Each dataset included two MRI scans: (1) pre-contrast (i.e. non-Gd) cine, and (2) post-contrast late gadolinium enhancement (LGE) images. The dataset was split into training (n=450), validation (n=150), and testing (n=159) subsets. The testing subset was held-out and was not seen by the model during training or parameter optimization. We developed a CNN model (Fig 1) to automatically identify patients with scar (SCAR+) from input stack of non-Gd cine images (short-axis slices at both end-diastolic and end-systolic phases). The model output was the probability of having scar in the input images. A patient is labeled SCAR+ if at least one image had a probability >50% to contain scar. Reference labels (SCAR+ or SCAR-) were determined by visual evaluation of the LGE images by two expert readers. We used hyperband method to optimize the hyper-parameters of the CNN model using a 5-fold cross-validation of the training/validation dataset. The CNN was trained for 400 epochs with optimized parameters: kernel size=5x5, number of channels =64 in first layer, learn-rate=0.0001, mini-batch size=8, dropout=0.5, and cross-entropy loss function. To avoid overfitting, we used inline image augmentation through rotation, translation, and mirroring. Also, we selected the final model as the one yielded best performance in the validation set.

Results: The two readers identified scar in 275 (36%) patients. The optimized CNN model showed strong discriminatory power (i.e. area-under ROC curve (AUC)) to identify patients with scar from non-Gd cine images in the validation and testing datasets (AUC =0.91 and 0.83, respectively). In the testing dataset, at a cutoff probability threshold = 50%, the model correctly identified 81% of patients without myocardium scar with accuracy 74% (Table 1). The overall number of patients who could have avoided unnecessary Gd contrast-injection is 34%.

Conclusion: Deep learning based analysis of non-Gd cine images allows accurate identification of myocardium scars in HCM patients and may save 1/3 of the patients from having unnecessary Gd injections.

Table 1. Performance metrics of the CNN-based scar identification model.

Metrics	AUC	Accuracy	Sensitivity	Specificity	F1	Recall	Precision
Validation	0.92	0.79	0.9	0.74	0.73	0.94	0.63
Testing	0.83	0.74	0.81	0.67	0.74	0.8	0.69

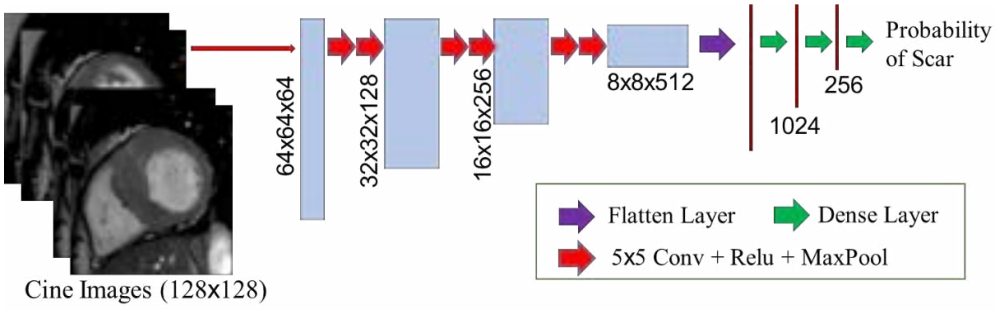

Figure 1. The architecture of the CNN model used for identifying patients with scar from non-Gd cine images.

Abstract ID: 55

Free-running 3D Simultaneous T_1/T_2 Myocardial Mapping in Less than 5 min with Low-rank Non-rigid Cardiac Motion-corrected Reconstruction

Andrew Phair[1], Gastao Cruz[1], Haikun Qi[1], René Botnar[1], Claudia Prieto[1]
[1]School of Biomedical Engineering and Imaging Sciences, King's College London, UK

Purpose: We have recently introduced a free-running framework for the simultaneous acquisition of 3D T_1/T_2 myocardial maps and 3D cine images with whole-heart coverage and isotropic spatial resolution in ~10 min[1]. In that study, ECG cardiac gating was used to reconstruct diastolic 3D T_1/T_2 maps and cine images by splitting data into one (T_1/T_2 maps) or multiple (cine) cardiac phases. Herein, we propose incorporating non-rigid cardiac motion correction to the low-rank dictionary-based reconstruction such that all acquired data may be used in the reconstruction of each cardiac phase for both T_1/T_2 maps and cine images, enabling improved image quality and significantly reduced scan time.

Methods: Data were acquired using a low flip angle spoiled gradient echo readout on a 3D golden angle radial trajectory. To provide sufficient T_1/T_2 encoding, each shot was preceded by an IR pulse and either no T_2-prep pulse or a T_2-prep pulse with an echo time of 30 or 60 ms. 3D rigid respiratory motion correction was applied to the k-space by extracting a respiratory signal from the k-space centre[2] and estimating translational motion from auxiliary respiratory bin images. The respiratory-motion-corrected spokes were ECG-gated into 10 cardiac phases, and further divided into three bins in the T_1 direction. For each T_1/cardiac frame, an auxiliary soft-weighted[3] GROG[4] reconstruction was performed and used to estimate the 3D non-rigid cardiac motion fields. The final data sorting, used for the motion-corrected reconstruction, consisted of the same 10 cardiac phases (with hard-gating), 15 T_1 bins and 3 T_2 bins. The reconstruction proceeded via the proposed low-rank motion-corrected method, minimising $\|E\boldsymbol{\rho} - W\boldsymbol{k}\|_2^2$ with conjugate gradient iteration. Here, $\boldsymbol{\rho}$ is the multi-compressed-contrast 3D image at the reference cardiac phase, $\boldsymbol{k}$ is the respiratory-motion-corrected k-space data, W contains the 3D radial density compensation factors and $E = \sum_n W\, U_r A_n F S M_n$ is the encoding operator, where M_n acts to apply the motion distortion for the nth cardiac phase, S contains the coil sensitivity maps, F is a 3D nuFFT operator, A_n is the k-space sampling operator for the nth cardiac phase and U_r is a low-rank T_1/T_2-dictionary-based compression operator obtained via a truncated SVD, which acts to compress and expand between the 45 T_1/T_2 bins and the r most significant singular contrasts[5] (here $r = 3$). For comparison, a motion-resolved reconstruction ($M = I$) was also performed. A temporal width of 190 ms (~twice the width of an individual cardiac bin) was considered for the latter. Both reconstructions were applied to a full set of data and to the same set of data undersampled such that only the first 50% of the acquired spokes were retained.

Results: The proposed approach is seen to produce good quality 3D images and parameter maps (Fig. 1), and no particular image degradation is evident from the undersampled data set (~5 min scan time). Compared to the motion-resolved reconstructions, the method is seen to avoid the noise and motion artefacts that are present in both cases and are significantly worse in the presence of undersampling.

Discussion: We have presented an extension of the free-running 3D T_1/T_2 mapping framework[1] which utilises non-rigid cardiac motion correction to increase image quality and increase robustness to undersampling. Future work will incorporate regularisation into the proposed approach.

References: [1]Qi, H, et al. MRI 2019;63:59-169; [2]Qi, H., et al. MRM 2019;82(4):1331-1342; [3]Küstner, T., et al. NMR Biomed. 2021;*34*(1):e4409; [4]Seiberlich, N, et al. MRM 2007;*58*(6):1257-1265; [5]Assländer, J, et al. MRM 2018;*79*(1):83-96.

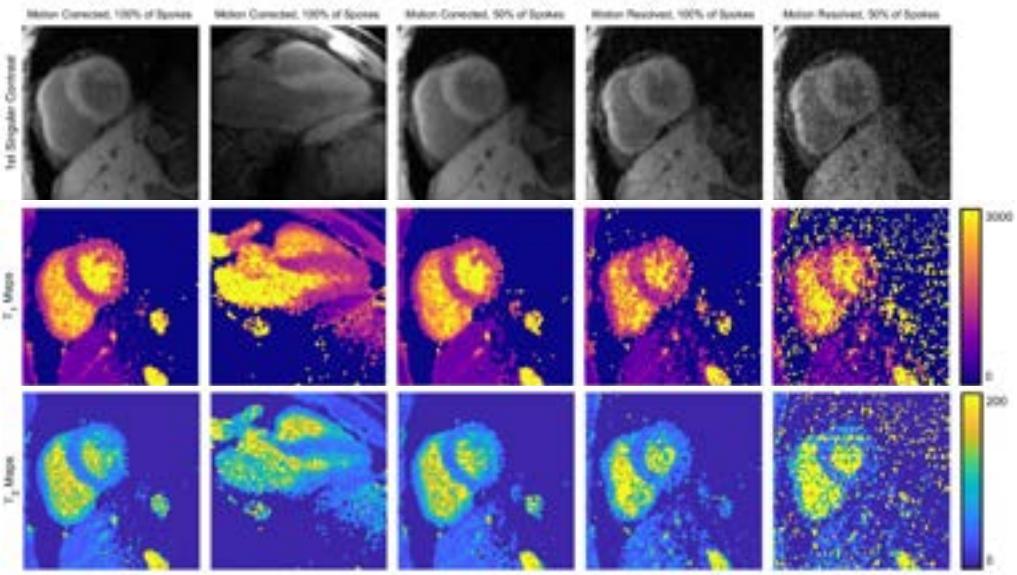

Fig. 1 2D slices of the 1st singular contrast and T_1 and T_2 maps achieved using the proposed motion correction scheme (shown at diastolic phase) and a motion resolved scheme, with 100% or 50% of the acquired k-space spokes. The motion-corrected 100% reconstruction is shown for two different slice orientations.

Abstract ID: 56

Shortening the saturation recovery time improves accuracy for quantification of arterial input function and myocardial blood flow from cardiac perfusion MRI

Lexiaozi Fan[1, 2], Kyungpyo Hong[1], Li-Yueh Hsu[3], Bradley D. Allen[1], Daniel C. Lee[4], Daniel Kim[1, 2]
[1]Department of Radiology, Northwestern University Feinberg School of Medicine, Chicago, IL
[2]Department of Biomedical Engineering, Northwestern University, Evanston, IL
[3]Department of Radiology and Imaging Sciences, National Institutes of Health, Bethesda, MD
[4]Division of Cardiology, Internal Medicine, Northwestern University Feinberg School of Medicine, Chicago, IL

Purpose: To investigate the impact of reducing the saturation-recovery time (TS) as short as 10 ms for quantification of arterial input function (AIF) and myocardial blood flow (MBF) from cardiac perfusion images.

Methods: We prospectively enrolled 12 subjects (mean age = 61±14 years, 7/5 males/females) and performed resting perfusion scans during administration of 0.0075 to 0.01 mmol/kg of gadobutrol (Gd) with a previously described pulse sequence with radial k-space sampling [1]. Relevant imaging parameters included: FOV=384mmx384mm, matrix size =192x192, TE/TR=1.5/2.9 ms, flip angle = 15°, nominal TS=10 ms, and 38 radial spokes per frame (corresponding to an acceleration factor of 5). From the same raw k-space data, we applied two different k-space weighted image contrast (KWIC) filters [3] for AIF and tissue function (TF) images, as previously described [1]. For TF image reconstruction using compressed sensing (CS)[2], KWIC was applied to maintain the center of k-space from the last radial spoke only such that the effective TS was 117.3 (=10+2.9*37) ms. For AIF using CS, we reconstructed five different KWIC filtered images, maintaining the center of k-space from the first to the fifth spoke only to produce effective TS from 10 to 21.6 ms (2.9ms steps). We then quantified five MBF maps (same TF image, five different AIF images) using the following steps: same motion correction and segmentation for all sets, signal intensity to gadolinium concentration conversion using the Bloch equation, T2* correction to AIF as previously described [4], and pixel-by-pixel MBF quantification.

Results: As shown in Figure 1, shorter effective TS linearizes the relationship between signal and Gd concentration ([Gd]), decreases the peak normalized signal, increases peak [Gd] and correspondingly decreases MBF values. For summarized results, see Table 1. Compared to TS = 10 ms, higher effective TS resulted in significantly decreased peak AIF ($p<0.05$) and increased MBF ($p<0.05$). The resting MBF (0.69 ml/g/min) calculated from AIF with effective TS of 10ms agrees better with the resting MBF reported by two cardiac PET studies: (a) mean MBF = 0.71 ml/g/min in 363 healthy subjects using ^{13}N-ammonia [5] and (b) mean MBF = 0.74 ml/g/min in 382 healthy subjects using ^{82}Rb [5].

Discussion: This study highlights the importance of reducing TS as short as 10 ms for accurate quantification of AIF and MBF. Limitation of this study is that it lacks ground truths for AIF and MBF. This is a common problem for quantitative cardiac first-pass perfusion studies in patients, unless one is able to perform multiple quantitative perfusion MRI scans on different days at different TS (logistical and gadolinium risk challenges, image processing steps among different image datasets can cause MBF variation).

References: [1] Naresh NK, et. al. Magn Reson Med 2019 [2] Lustig M, et. al. Magn Reson Med 2007 [3] Song HK, et. al. Magn Reson Med 2007 [4] Fan L, et. al. Magn Reson Med 2021 [5] Murthy VL,, et. al. Society of Nuclear Medicine 2018

Table 1. Summary of peak AIF and resting MBF values from 12 subjects. Reported values represent mean ± standard deviation. Compared with TS=10 ms as reference, both AIF and MBF values for different effective TS values were significantly different.

	TS = 10ms	TS = 12.9 ms	TS = 15.8 ms	TS = 18.7 ms	TS = 21.6 ms
AIF (mM)	13.57 ± 1.85	11.07 ± 1.79	9.65 ± 1.55	8.64 ± 1.41	8.1 ± 1.32
MBF(ml/g/min)	0.69 ± 0.14	0.85 ± 0.16	0.98 ± 0.19	1.11 ± 0.21	1.19 ± 0.23

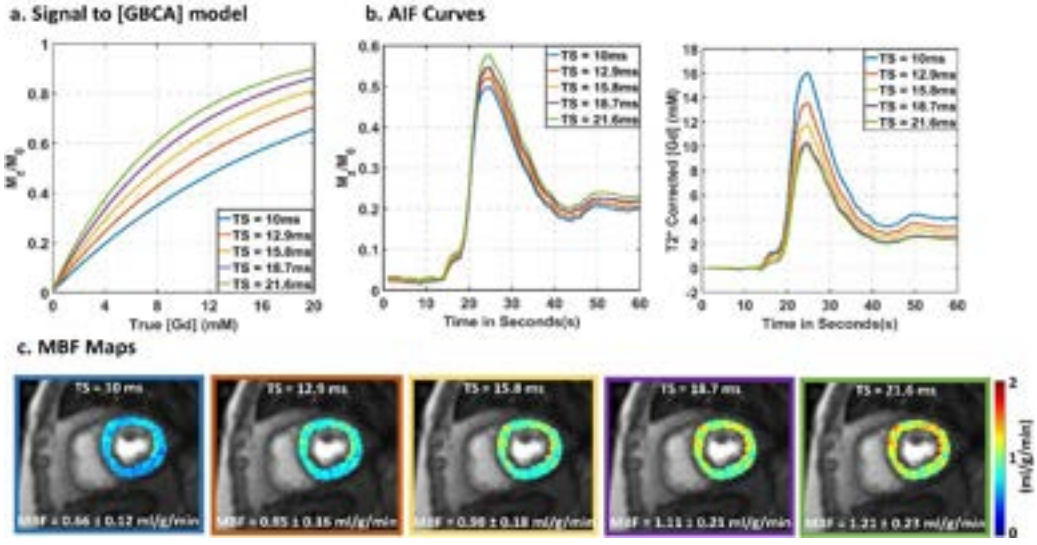

Figure 1. (a) Plots describing the relationship between the normalized signal and [Gd] for five different TS values;

(b) Plots of the AIF signal-time curves, and AIF [Gd]-time curves with T2* correction;

(c) The corresponding MBF maps with mean values as shown.

Abstract ID: 57

Self-calibrating method to simultaneously optimize 4D Flow eddy current correction & detect wraparound artifacts using a novel stochastic 4D flow-field disparity signature technique

Thara Nallamothu[1,2], Haben Berhane[1,2], Liliana Ma[1,2], Justin Baraboo[1,2], Daniel C. Lee[3], Daniel Kim[1], Philip Greenland[4], Michael Markl[1,2], Rod Passman[3], Mohammed S.M. Elbaz[1]

[1]Radiology, [2]Biomedical Engineering, [3]Medicine (Cardiology), [4]Preventive Medicine, Northwestern University

Purpose: Eddy current correction is an essential preprocessing step to correct velocity offset errors in 4D Flow MR images for accurate flow quantification. Offset errors present spatiotemporally varying inaccuracies in each of the 4D Flow velocity components corrupting the resulting velocity vectors. Manual corrections can be time-consuming, observer-dependent, and sensitive to wraparound artifacts. Emerging automated methods (e.g. deep learning) may require large training data with limited generalizability to different scan protocols and do not fully account for the spatiotemporal-dependent error distributions in the velocity components. Here, we propose a self-calibrating method to simultaneously optimize eddy current corrections and detect wraparound errors using our recently introduced 4D flow-field signature technique that stochastically encodes the entire spatiotemporal pairwise *velocity vector disparity profile*. We hypothesize that disparate spatiotemporal eddy current errors over velocity directions result in altered velocity vector disparity signatures that further diverge in the case of a wraparound error. Effective correction would reduce spatiotemporal errors over all velocity directions across the flow region, yielding converging vector disparity signatures, allowing the signature to be an optimization metric for eddy current correction. Here, we show the method's feasibility and generalizability to different 4D Flow protocols.

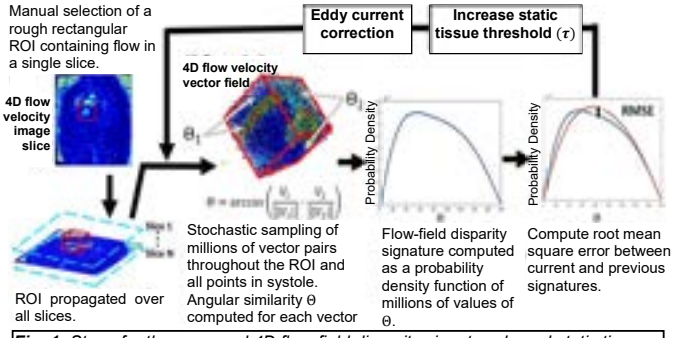

Fig. 1: *Steps for the proposed 4D flow-field disparity signature-based static tissue threshold optimization*

Table 1: 4D Flow Scan protocols

Protocol 1	Protocol 2
Sagittal orientation, Prospective gating, PEAK-GRAPPA, R=2-5, spatial resolution 2.4-2.7mm^3, temp. resolution= 40-77 ms	Coronal orientation, retrospectively-gated, highly-accelerated Compressed Sensing 4D Flow, R=10.2, spatial resolution=2.4-2.8 mm^3 temp. resolution = 41ms

Methods: A total of 36 IRB-approved subjects were included: 26 atrial fibrillation patients scanned with 4D flow protocol 1, and 10 healthy volunteers with 4D Flow MRI protocol 2 (Table 1). *Eddy current correction:* Static tissue regions over all the slices were defined as voxels with a standard deviation of temporal velocity below a static tissue threshold ($\boldsymbol{\tau}$), and a 3D linear regression was fit to the static tissue region to compute a 3D offset map. This was subtracted from the entire 4D flow image volume[1]. Initial $\boldsymbol{\tau}$ was such that the static tissue region occupied ≥ 1% of the 3D image volume. ***Proposed Optimization of static tissue threshold (τ):*** A 2D ROI containing flow region was manually selected and propagated over all slices and time frames (Fig. 1). Stochastic *4D flow-field disparity signature:* The flow-field disparity signature was computed as a probability density function of ~30 million pairwise angular velocity-vector disparity values (Θ) over the spatiotemporal ROI[2]. (Fig. 1) *Convergence:* The eddy current correction and resulting signature were iteratively computed with increasing $\boldsymbol{\tau}$ with a step size of 0.001. Root mean square error (RMSE) was computed between signatures for each successive pair $\boldsymbol{\tau_i}$, $\boldsymbol{\tau_{i-1}}$. Criteria for signature convergence were RMSE<1% for 10 successive iterations. The optimal threshold $\boldsymbol{\tau_{automated}}$ was defined as the minimum converging $\boldsymbol{\tau}$. ***Automated wraparound error detection:*** Presence of wraparound artifact was defined as non-monotonic sequence of RMSE for ≥3 successive iterations prior to convergence to $\boldsymbol{\tau_{automated}}$ (Fig.2). ***Validation:*** 4D Flow Images were processed using $\boldsymbol{\tau_{automated}}$ and compared to an independent manually identified optimal threshold $\boldsymbol{\tau_{manual}}$. Volumetric left atrial (LA) Peak ($\boldsymbol{v_{peak}}$) and mean ($\boldsymbol{v_{mean}}$) velocities over the cardiac cycle were computed in segmented LA and tested for agreement using coefficient of variation (CoV) intraclass correlation (ICC). Ground-truth for wraparound errors was determined manually by a blinded visual inspection of 4D flow magnitude slices.

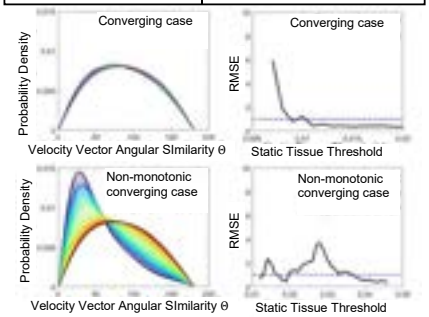

Fig. 2 *Example of a monotonic disparity signature convergence in wraparound-free case & non-monotonic convergence in a case with wraparound.*

Results: The method correctly identified 10 out of the 12 manually identified scans with wraparound error. All were AF patients scanned with protocol 1. The remaining 24 scans using both protocols 1 & 2 were all correctly identified as wraparound-free (Fig. 2). Excellent LA velocity agreement was found regardless of the 4D Flow protocol used or the presence of wraparound artifact with all showing CoV<3%. The 24 wraparound-free cases showed ICC=0.99 for $\boldsymbol{v_{peak}}$ and ICC=0.97 for $\boldsymbol{v_{mean}}$. Similarly, excellent ICC = 0.96 for $\boldsymbol{v_{peak}}$and ICC=0.92 for $\boldsymbol{v_{mean}}$ were found in the 12 AF patients with wraparound artifact. Bland-Altman showed no significant bias and narrow limits of agreement [-2, 2] cm/s.

Discussion: Using our novel 4D flow-field disparity signature to encode the disparity profile of the entire spatiotemporal three-directional velocity vector-field, we developed a self-calibrating method for optimizing eddy current corrections and simultaneously identifying wraparound errors. The proposed method does not require training data nor comparison to other patients. Importantly, the results demonstrated the generalizability of the method showing excellent agreement in LA velocity measurements vs. the manually optimized, in two 4D Flow MRI protocols with different scan orientation, acceleration methods (CS vs. GRAPPA) as well as in the cases with identified wraparound artifact. Our results may support the potential wide utility of our method. Future work will validate in larger cohort with different scan protocols & multi-vendors scanners.

Ref. [1] Walker, P.G., et al. (1993), JMRI, 3: 521-530.; [2] Nallamothu et al. ISMRM, 2021. **Ack.** Grant Support: AHA 20TPA35490311, Sylvia Wolff Award

Abstract ID: 58

Placental Maternal Blood Volume Measurements in Rhesus Macaques using Variable Flip Angle T1 Mapping

Ruiming Chen[1], Sydney Nguyen[2 3 4], Megan E. Murphy[2 3 4], Kathleen M. Anthony[2 3 4], Terry K. Morgan[7], Philip Corrado[1], Sean B. Fain[1 5], Ronald R. Magness[8], Dinesh Shah[4], Thaddeus Golos[2 3 4], Oliver Wieben[1 5 6], and Kevin M. Johnson[1 6]

[1]Medical Physics, [2]Wisconsin National Primate Research Center, [3]Comparative biosciences, [4]Obstetrics & Gynecology, [5]Biomedical Engineering, [6]Radiology, University of Wisconsin-Madison, Madison, WI, United States, [7]Pathology, Oregon Health & Science University, Portland, OR, United States, [8]Obstetrics & Gynecology, University of South Florida, Tampa, FL, United States

Purpose: In-vivo MRI measurement of placental vasculature during pregnancy can provide novel insight into placental development and sufficiency of nutrient exchange [1-2]. This study investigates the use of iron-based Ferumoxytol to quantify maternal fractional blood volume (mFBV) and maternal placental blood volume (mPBV) in the rhesus macaque placenta across multiple gestation ages.

Methods:

Image Acquisition: Seven pregnant rhesus macaques were imaged longitudinally across gestational days 64.5±1.9, 100.8±3.9, and 145.3±1.8. Four subjects received a zika virus injection into the amniotic fluid around day 55 and three control subjects received a saline injection. All subjects were sedated using isoflurane and imaged in right-lateral position on a 3.0 T system (Discovery MR750, GE Healthcare) with a 32-channel phased array coil. T1 mapping was performed with a respiratory-gated center out, 3D radial, VFA T1-weighted spoiled gradient echo (SPGR) sequence (TR = 6.0 ms, TE = 1.2 ms, resolution = 0.78*0.78*0.78 mm^3, flip angle = 2°, 6°, 10°, 14°). After pre-contrast imaging, Ferumoxytol was intravenously administered with a power injector (4 mg/kg Feraheme™, diluted 5:1 with saline and infused over 20 sec). Approximately 30 minutes later, the T1 mapping sequence was repeated (Figure 1).

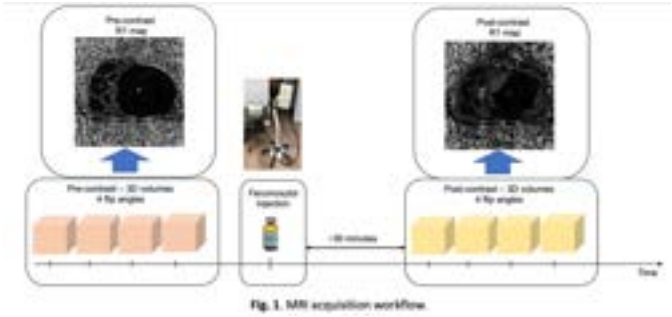

Fig. 1. MRI acquisition workflow.

Data analysis: R1 maps were derived using complex fitting to SPGR signals using an inhouse toolbox. Pre- and post-contrast scans were registered using non-rigid registration (ANTs [4]). Placental volumetric segmentations and ROIs in major vascular structures were drawn manually. Pre- and post- contrast R1 changes (ΔR1) in placental and vascular regions were used to derive (1) mFBV, the fractional amount of placental volume occupied by maternal blood, calculated as the ratio between median ΔR1 in placenta and maternal blood [3], and (2) mPBV, the total amount of maternal blood in the placenta, calculated as placental volume multiplied by mean mFBV.

Results and Discussion: The zika virus injection was shown to result in modest pathological changes compared to the controls [5]. mFBV exhibited a regionally heterogeneous distribution as shown in Figure 2. Longitudinally, mPBV for all subjects increased constantly with gestational age, whereas mFBV showed heterogeneous trends, with higher degree of heterogeneity during early pregnancy (Figure 3). Pixel-wise histogram distributions (Figure 4) of ΔR1 values show a shift to the left for both placental and blood regions at the second gestational time point. Some variation in the ΔR1 of blood was observed which could be due to imperfect injections stemming from the use of a power injector designed for larger volumes. However, this variation did not affect fractional blood volume measurements since they do not require prior knowledge of the amount of contrast injected.

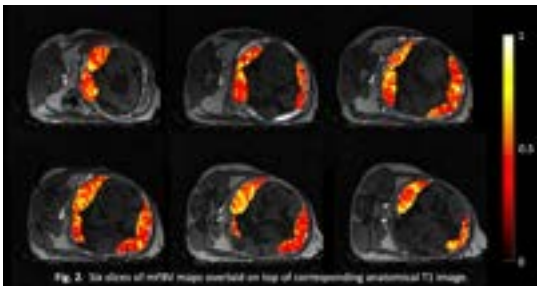

Fig. 2. Six slices of mFBV maps overlaid on top of corresponding anatomical T1 image.

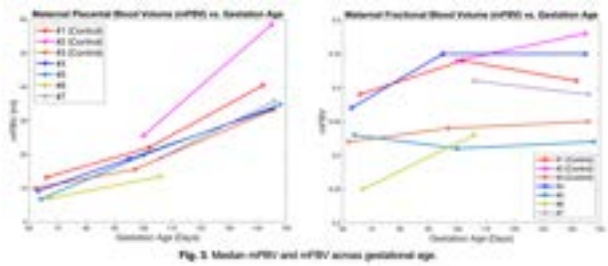

Fig. 3. Median mPBV and mFBV across gestational age.

To our knowledge, this is the first study to report placental regional blood volume estimates in vivo. The mean fractional blood volume across all subjects shows a slight increase with gestation, which is consistent with the findings from previous literature using a mouse model [3]. However, more subjects and more gestational time points are needed for further investigation.

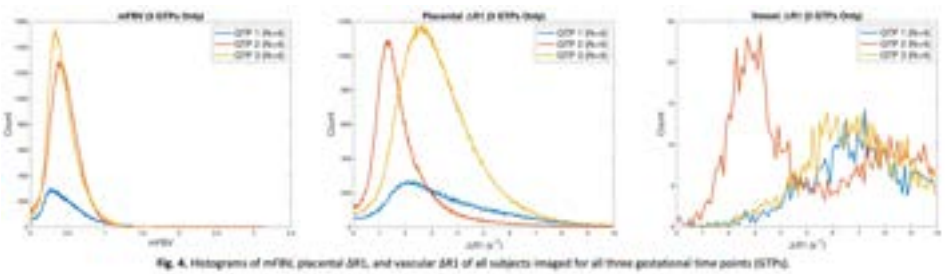

Fig. 4. Histograms of mFBV, placental ΔR1, and vascular ΔR1 of all subjects imaged for all three gestational time points (GTPs).

References: [1] Roberts VHJ et al. *Reprod Sci.* 2018;25(1):110-119. [2] Hutter D. et al. *Int. J. Pediatr.* 2010, 401323. [3] Badachhape, AA et al. *Sci Rep 9, 18707 (2019). [4] Brian BA et al. Proceedings of the Fifth Workshop on Biomedical Image Registration 2012:266-275. [5] Nguyen SM et al. Biol Reprod. 2020 Feb 14;102(2):434-444.*

Abstract ID: 59

Multi-echo 3D-MERGE for Large-coverage Quantitative Carotid Vessel Wall Imaging

Zechen Zhou[1], Niranjan Balu[2], Shuo Chen[3], Baocheng Chu[2], Peter Börnert[4], Thomas Hatsukami[2], Chun Yuan[2]

1. Philips Research North America, Cambridge, MA, United States; 2. Vascular Imaging Lab, University of Washington, Seattle, WA, United States; 3. Center for Biomedical Imaging Research, Tsinghua University, Beijing, China 4. Philips Research Hamburg, Hamburg, Germany

Purpose: 3D-MERGE[1] has been developed as a fast screening sequence for carotid vessel wall imaging (VWI). However, it can only provide plaque burden measurement without quantitative MR maps for plaque component analysis. Enlarged field-of-view (FOV) may also ease sequence planning for screening applications. To this end, an enlarged FOV multi-echo 3D-MERGE acquisition with DIXON water fat separation and quantitative susceptibility mapping (QSM) reconstruction was developed and evaluated on 10 healthy subjects and 5 patients.

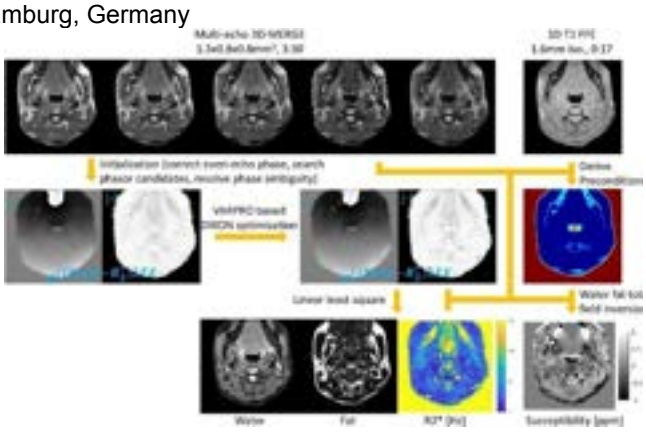

Figure 1: Proposed flowchart for multi-echo 3D-MERGE processing to produce water fat separation and quantitative R2*/susceptibility maps. Examples are from a volunteer data.

Methods: *Multi-echo 3D-MERGE with enlarged FOV*: FOV in anterior-posterior (AP) was enlarged to cover the whole neck (160mm vs 40mm), and the scan was accelerated to keep the same acquisition time (3:30). Unlike 3D-MERGE, fat suppression was not applied. To reduce ΔTE (1.57ms) for more robust water fat separation, bipolar readout with anisotropic resolution (1.3x0.8x0.8mm^3) was used for 5-echo acquisition. *DIXON water fat separation*: To estimate water, fat, R2*, and field map, a variable projection (VARPRO) based DIXON approach[2] was adapted with additional even-echo phase correction for bipolar readouts. *Water fat total field inversion (TFI) for QSM*: The DIXON model was further used to estimate the susceptibility map by using a preconditioned water fat TFI approach[3]. The preconditioner was derived from another rapid low-resolution gray-blood scan which can better separate the foreground tissue (including lumen regions) from the background air. The overall post-processing flowchart was summarized in figure 1. *MR scans*: All MR scans were performed on a Philips 3.0T scanner using an 8-channel carotid coil. Besides multi-echo 3D-MERGE, 0.8mm isotropic 3D-MERGE and SNAP[4] were acquired for comparison.

Results: Example images from a patient were shown in figure 2. The enlarged AP FOV can cover the entire carotid arteries and allow simplified scan planning even without a localizer MRA. Compared to water fat separation by Philips mDIXON product, the proposed approach can robustly reduce the water fat swapping artifacts (red arrows), which allows more accurate fat quantification. Additional large-coverage carotid R2* and susceptibility maps can also be reconstructed to provide quantitative maps. Figure 3 showed a zoom-in comparison for a calcified plaque (identified by bright-blood I2 image of SNAP, red arrow). Multi-echo 3D-MERGE provided quantitative evidence (i.e. high R2* and negative QSM, red arrows) to identify calcification.

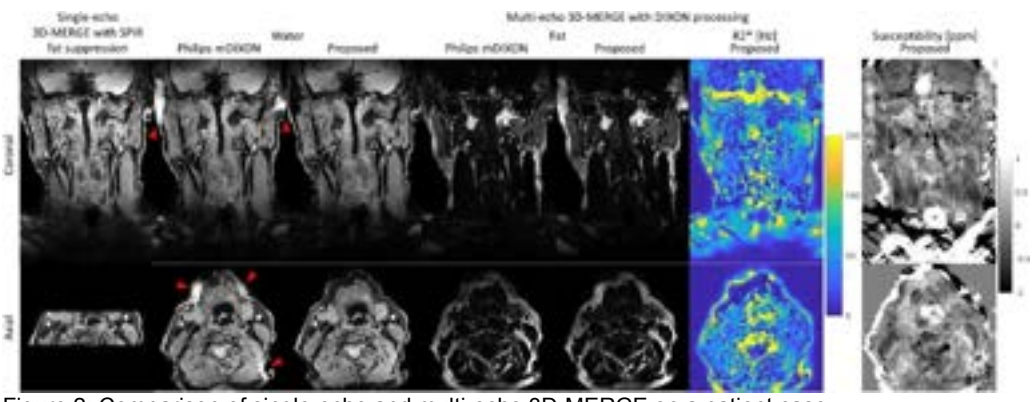

Figure 2: Comparison of single-echo and multi-echo 3D-MERGE on a patient case.

Discussion: A 3:30 multi-echo 3D-MERGE with DIXON and QSM reconstruction was developed for carotid VWI, which simplifies the scan planning and provides robust water fat separation and quantitative MR maps for plaque component analysis.

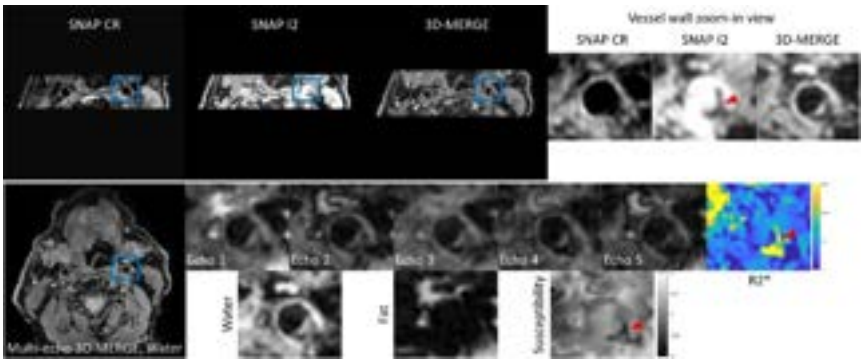

Figure 3: Zoom-in comparison (blue square) of different scans for calcification detection.

References: [1] Balu N, et al. Magn Reson Med. 2011;65:627-37. [2] Zhou Z, et al. ISMRM 2021, p1627. [3] Boehm C, et al. ISMRM 2021, p0792. [4] Wang J, et al. Magn Reson Med. 2013;69:337-45.

Abstract ID: 60

!"#$%&'%()*+(*,%-.*/0$.1%(%2 3 4 5 0 6 #$*7.('"06'*8)#('*7.(&#('"0'%.(*%(** 7.('"06'*9(:0(&#$*;<8*506#$*.(*51..$*=%)(01*+('#(6%'>*

!"#$%&'(()*+,%-./$01/(%231$/)4/(5,%6'*1)7#*#%8%:;#(<+,%=);/*%>9%?)(31)$@,%-(/A'(B%89%C);*'$D,E,%8/FF(/B%G9%=#<)+,D%

+%H% I $)" /(*)0B%'F% : ';'(#4',%>.('(#,%:J,% I 2>%%%D%H% I $)" /(*)0B%'F%C#*1)$A0'$,%2/#00;/,%C>,% I 2>%%%

%5%K% I $)" /(*)0B%G'*L)0#;%'F%2##(;#$4,%G'7M.(A,%-/(7#$B%%%@%H%N(#33'%07#A)$A,%=);#$,%00#;B%%%E%H%N#B/(,%C1)LL#$B,%&8,% I 2>%

!2"?.6#P% Q/3/$0%!"# $!%& '%#$4%01/'(/0)3#;%R'(<%S+,DT%1#*%4/7'$*0(#0/4%#%*.M;)$/#(%(/;#0)'$*1)L%M/0R//$%01/%M;''4% 3'$3/$0(#0)'$%'F%A#4';)$).7KM#*/4%3'$0(#*0%#A/$0*%SU - N : >VT%#$4%Q+,%#*%R/;;%#*%L'0/$0)#;;B%)7L#30F.;%QDW%"#;./*%#0%1)A1% 3'$3/$0(#0)'$*9%%61/*/%(/;#0)'$*1)L*%R/(/%(/3/$0;B%"#;)4#0/4%)$%##%L)A%7'4/;%R1/(/%M;''4%U - N : >V%#$4%0)7/K(/*';"/4%:!K =Q>%*)A$#;%)$0/$*)0B%S2 0T%R/(/%*)7.;0#$/'.*;B%7/#*.(/4,%3'$3;.4)$A%01#0%#T%M;''4%2 0%F'(%:!K=Q>%3#$%M/%#33.(#0/;B% L(/4)30/4%M#*/4%'$%U - N : >V,%#$4%MT%)F%01/%#F'(/7/$0)'$/4%(/;#X)")0B%(/;#0)'$*1)L*%#(/%4)*3'.$0/4,%L(/4)30)'$%'F%2 0%)*%L''(,% L#(0)3.;#(;B%#0%1)A1%U - N : >V%S5T9%61)*%)*%'F%*)A$)F)3#$0%)7L'(0#$3/%0'%01/%'L0)7#;%.*/%'F% - N : >%F'(%0/31$)Y./*%*.31%#*%:!K =Q>,%#$4%*.LL'(0*%01/%.*/%'F%*;'R/(,%;''$A/(%3'$0(#*0%)$Z/30)'$*9%%>;*'%)7L'(0#$0%)*%01/%(/"/(*/%H%$#7/;B%3#$%U - N : >V%M/% #33.(#0/;B%L(/4)30/4%F(''7%20[%%61)*%)*%'F%3'$*)4/(#M;/%)$0/(/*0%F'(%0/31$)Y./*%*.31%#*%4B$#7)3%3'$0(#*0%=Q0,%R1/(/% #33.(#0/%(/;#0)'$*1)L*%M/0R//$%20%#$4%U - N : >V%#(/%)7L'(0#$0%F'(%Y.#$0)0#0)"/%0/31$)Y./*%*.31%#*%L/(F.*)'$9%%61)*%R'(<% .0);)\/*%01)*%*#7/%4#0#*/0%0'%/XL;'(/%01/%](/"/(*/^%L('M;/7_%)9/9%1'R%R/;;%U - N : >V%3#$%M/%L(/4)30/4%F('7%209%

;#':.$6**@% C/%)$"/*0)A#0/4%*)X%Z."/$);/%-/(7#$%*R)$/%SE5K`5%<AT9%I$4/(%A/$/(#;%#$#/*01/*)#,%0R'%#$)7#;*%/#31%R/(/% #47)$)*0/(/4%01(//%*/L#(#0/%a9+%77';b<A%4'*/*%'F%'$/%'F%01(//%-N : >*P%A#4'0/()4';%Sc('G#$3/,%N(#33'T,%A#4'M.0(';% S-#4#")*0,%N#B/(T,%A#4'M/$#0/%S=.;0)G#$3/,%N(#33'T9%>;;%)$Z/30)'$*%R/(/%L/(F'(7/4%#0%(#$4'7)\/4K'(4/(%"#(B)$A%(#0/*%S+,% D,%'(%5%7db*T%4.()$A%0)7/K(/*';"/4%5e%2c-Q%)7#A)$A%'F%01/%#'(0#%S+9E6%2)/7/$*%>/(#,%6Qb6!%@9`b+9@%7*,%!f5a$^a$,%0/7L'(#;% (/*';.0)'$%+9g%*T9%:'$3.((/$0%R)01%=Q%#3Y.)*)0)'$,%a9E%7d%#;)Y.'0*%'F%#(0/()#;%M;''4%R/(/%*#7L;/4%/"/(B%D%*/3'$4*%X%@a% 01('.A1%#$%)$4R/;;)$A%#'(0)3%3#01/0/(%#$4%*/$0%F'(%7#**%*L/30('7/0(B%0'%4/0/(7)$/%U - N : >V9%J$;B%01/%)$)0)#;%)$Z/30)'$%F'(% /#31%L)A%S$f`T%R#*%#$#;B\/4,%#*%M#*/;)$/%U - N : >V%R#*%\/('9%=#0;#M%R#*%.*/4%0'%3(/#0/%#%;''<.L%0#M;/%'F%U - N : >V%"*9%2 0% M#*/4%'$%01/%<$'R$%2c-Q%20%/Y.#0)'$%K%20$_{2c-Q}$!%S+K/$^{K6Q%Q+}$TbS+%K%3'*!/$^{K6Q%Q+T%*}$%!/$^{K6!%QDW%}$K%#*%R/;;%#*%01/%R#0/(%/X31#$A/% #$4%*L)$K*L)$%/FF/30*%#FF/30)$A%01/%M/1#")'(%'F%Q+%#$4%QDW%)$%M;''4%S+,DT9%%h'(%/#31%<$'R$%U - N : >V%M#*/4%'$%7#% *L/30('7/0(B,%01/%3'(((/*L'$4)$A%20%R#*%4/0/(7)$/4%F('7%01/%#LL('L()#0/%=#0;#M%;''<.L%0#M;/%#F0/(%$'(7#;)\)$A%01/%M#*/;)$/% =Q%20%0'%\/('%U - N : >V9%%6)7/%*1)F0*%M/0R//$%#30.#;%#$4%L(/4)30/4%U - N : >V%R/(/%F)$/K0.$/4%*'%01#0%()*/%0)7/*%3')$3)4/49% Q/A(/**)'$%#$#;B*)*%R#*%L/(F'(7/4%'$%#30.#;%"*9%L(/4)30/4%*3#00/(%4#0#9%%

<#621'6@*20#3</4%;/F0%F)A.(/%L#)(%M/;'R%4/7'$*0(#0/*%/X#7L;/%L(/4)30/4%"*9%#30.#;%UA#4'0/()4';V%H%Y.)0/%A''4%F'(%i%j`Kg% 7=,%M.0%7.31%;/**%#33.(#0/%#0%1)A1/(%L/#<%U - N : >V%S$'0/%#((RT9%07 7/4)#0/;B%0'%01/%()A10%)*%01/*#7/,%1'R/"/(%$/A;/30)$A% 4/*3()M/4%Q+%/FF/30*%S)9/9%#**.7)$A%Q+%M/1#"/*%#*%)$%L;#*7#T%#$4%4)*3'.$0)$A%QDW%/FF/30*_%$'0/%L''(%3'(((/;#0)'$9%23#00/(% L;'0%(/L(/*/$0*%L(/4)30/4%"*9%#30.#;%U - N : >V%S;)7)0/4%0'%i%`9E%7=T,%4/7'$*0(#0)$A%A''4%3'(((/;#0)'$%#0%01/*/%;'R/(%U - N : >V_% 5%#A/$0%3'(((/;#0)'$%*;''L/*%a9k5%H%a9kk,%Q^D%a9gkKa9IE,%7/#$%#M*';.0/%/((('(%a9+gKa9DD,%7/#$%*Y.#(/%/(((''(%a9aIKa9D`9%%

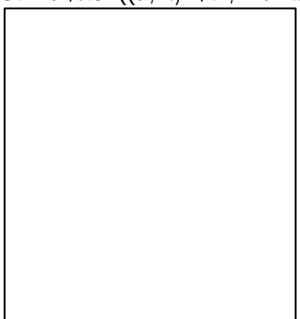

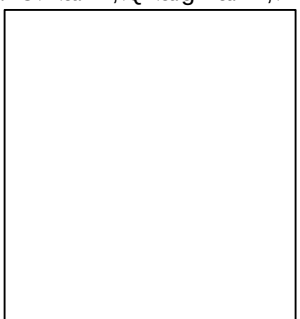

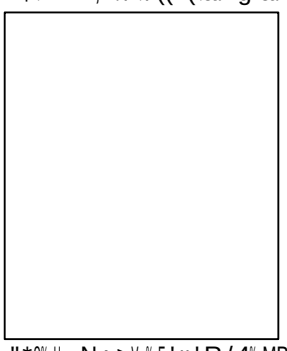

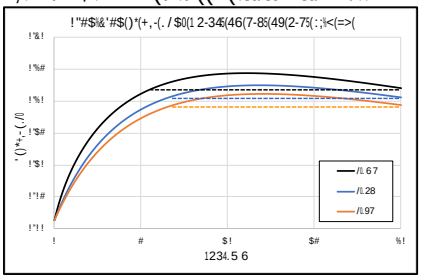

A%6&266%.(@%>;;%-N : >*%#(/%/XL/30/4%0'%1#"/%#%M()*<%M.0%*.M;)$/#(%()*/%)$%20% "*9%U - N : >V,%F';;'R/4%MB%#%L;#0/#.%#$4%4/*3/$0%S()A10%A(#L1T9% N/B'$4%`%K%g%7=,%01/%3.("/%F;#00/$*%$R)01%0R'%*';.0)'$*%F'(%/"/$% 1)A1/(%20m*%4.0/%0'%QDW%/FF/30*T%61.*%)0%)*%/XL/30/4%01#0%L(/4)30)'$% R);;%M/%L''(%#0%1)A1/(%U - N : >V9%h.(01/(7'(/,%*;)A10%A#)$%'FF*/0*%1#"/%$'%*';.0)'$%)F%20%/X3//4*%L(/4)30/4%20 7 #X%S#((''R%;/F0% A(#L1T9%%:'$*)4/()$A%'$B%U - N : >V%i%`9E%7=%S*3#00/(%L;'0T%01/(/%)*%A''4%3'(((/;#0)'$%R1/$%)$3'(L'(#0)$A%01/%4/*3()M/4%Q+% #$4%QDW%/FF/30*,%R)01%#%0(/$4%'F%.$4/(/*0)7#0)$A%U - N : >V%MB%j+En%#$4%7/#$%/(((''(*%a9D%7=%'(%;/**9%&'0#M;B,%01/*/%(/*.;0* *.AA/*0%01/%F/#*)M);)0B%'F%#33.(#0/;B%L(/4)30)$A%U"#$!$'%U - N : >V%F(''7%20%)$%#$%#$)7#;%7'4/;,%#(A.#M;B%01/%7''*0%4)FF)3.;0%L(''")$A% A(''.$4%F'(%*.31%Y.#$0)0#0)"/%#$#;B*)*%C/%M/;)/"/%01/%;#(A/*0%/((''(*%''33.(%4.()$A%U - N : >V%L/#<%4./%0'%*;)A10%0)7)$A% 4)FF/(/$3/*%)$%*#7L;)$A%"*9%=Q,%#$4%R)01''.0%'33#*)'$#;%*.31%/((#$0%4#0#%/"/$%M/00/(%(/*.;0*%#(/%L'**)M;/9%%

<#B#"#(&#6@*

*()# *!+,''"#-./#*''0,#1/#23&!"45&#62#5%#7+)#174"#85,''"#150#9:(;<=9>(=;?@A;)##*

*9)# *!+,''"#-./#23&!"45&#62#.&/#B7,%7C&'D,#2/#17E!#.F)#174"#85,''"#150#9:(?<==>9:(A@9=)##*

G)# H'&&!,#I/#2JK"5!05&#-/#6+7&EL./#M!&JK!"#1N/#!+,''"#-./#17E!#.F)##O&'J550!"4,#P2181#9:9(/#NQ,%&7J#((G=)##

Abstract ID: 61

Automated Cerebral Vascular Function Estimation for Permeability Estimation

W.S. Loos[1-3], R. Souza[3,4], L.B. Andersen[1-3], R.M. Lebel[1,3,5], and R. Frayne[1-3]
[1]Radiology and [2]Clinical Neuroscience, Hotchkiss Brain Institute, University of Calgary
[3]Seaman Family MR Research Centre, Foothills Medical Centre,
[4]Electrical and Software Engineering, University of Calgary, and
[5]General Electric Healthcare, Calgary, AB, Canada

Purpose

Quantitative physiological maps of permeability parameters, like volume transfer constant (k_{trans}) and fractional plasma volume (v_p), have proven to be a valuable tool for the diagnosis of brain cancer.[1,2,3] However, the estimation of permeability maps involves the identification of a suitable vascular function (VF) that describes the concentration of the injected contrast agent over time in a blood vessel within the organ of interest.[4] A VF is often obtained manually, making this process time-consuming and subject to error. In this work, we propose a method to automatically extract a suitable VF to estimate the permeability maps.

Methods

A total of 43 patients with glioblastoma were enrolled in this study (age: 59 ± 9.8 years [mean ± standard deviation], 19 male). They were scanned post-resection using a protocol approved by our local research ethics board. A total of 155 DCE-MR image volumes were obtained from these patients. Manually, 155 regions in the left or right transverse sinus were selected from a coronal image slice. The image volumes were randomly divided into 100 (64.5%) volumes for training, 23 (14.8%) volumes for validation, and 32 (20.6%) volumes for testing. We used a 3D U-net architecture to take full advantage of the volumetric information from the DCE MR images. The VF extracted from our model was compared with the manually extracted function. The permeability maps (k_{trans} and v_p) estimated by the manual VF were compared to the maps estimated using our VF extracted automatically. The non-brain tissues were removed from the permeability maps prior to performing the statistical test.

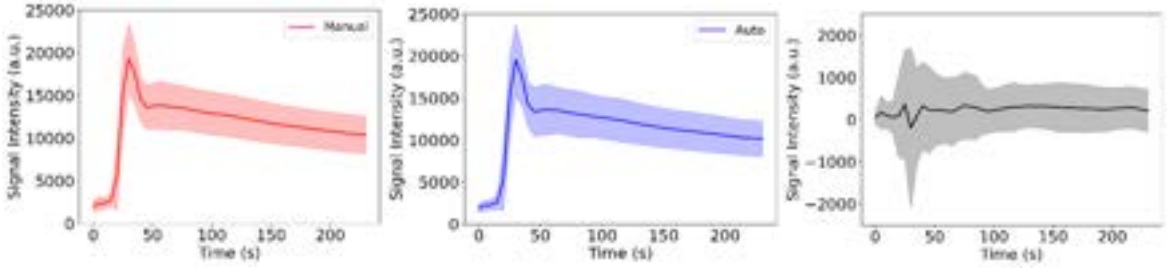

Figure 1: The average (line) and standard deviation (shaded region) over (left) manual test data and (middle) predicted vascular function (VF) curves. The average and standard deviation difference (right) between the manual and predicted VF curves. Note the six-fold reduction in scale for the vertical axis in the difference plot.

Results and Discussion

The mean absolute error found for the test set was 6.98 x 10^{-4}, where an error close to zero represents a good VF (Figure 1). This small error suggests that our model can predict an acceptable VF. The median and IQR of all 32 k_{trans} and 32 v_p maps using the VF manually extracted were 4.68 × 10^{-3} min^{-1} [3.63, 5.50] × 10^{-3} min^{-1} and 3.33 × 10^{-2} [3.04, 3.73] × 10^{-2} (unitless). Values obtained using our automatic VF were 4.87 × 10-3 min-1 [3.60, 5.53] × 10^{-3} min^{-1} and 3.31 × 10^{-2} [2.94, 3.72] × 10^{-2}. No statistical differences were found. Our method was able to estimate permeability maps similar to the those obtained with manual VF. Additional experiments are required to evaluate the generalization of the model and to evaluate the quality of the permeability maps in broader clinical practice.

References

[1] Nam JG, Kang KM, Choi SH, et al. *AJNR Am J Neuroradiol*. 2017; **38**(12): 2243-2250. [2] Thomas AA, Arevalo-Perez J, Kaley T, et al. *J Neurooncol*. 2015; **125**(1): 183-190. [3] Yun TJ, Park CK, Kim TM, et al. Radiology. 2015; **274**(3): 830-840. [4] Calamante F. *Prog Nucl Magn Reson Spectrosc*. 2013; **74**: 1-32.

Abstract ID: 62

Guidelines for institutional policy regarding the safe use of ferumoxytol for MRI and MRA

Yasaman Soltani; Mubeena Abdulkarim, MD; Shivam Kaushik, BS; Liisa L. Bergmann, MD, MBA; Chris J. François, MD; Mark L. Schiebler, MD; J. Paul Finn, MD

Purpose: Ferumoxytol (Feraheme®, AMAG Pharmaceuticals, Waltham, Massachusetts, USA) is a type of ultrasmall superparamagnetic iron oxide (USPIO) agent which the FDA approved for the treatment of iron deficiency anemia (IDA) in adult patients with chronic kidney disease in 2009. In 2018, approval was broadened to all adults with IDA. Ferumoxytol is also useful, off-label, as an intravenous contrast agent for magnetic resonance imaging (MRI) and angiography (MRA). Ferumoxytol's high cost, Boxed Warning, and highly specialized knowledge level regarding its use as an MR contrast agent have been barriers to wide clinical adoption. Recently an adult congenital cardiologist ordered an adult cardiac MRI with MRA and requested ferumoxytol contrast, at a multi-specialty medical center where MR with ferumoxytol had never been performed clinically in an adult before.

Method: Numerous stakeholders were identified following a web-based MR Operations Committee meeting. Stakeholders included hospital administration, pharmacy, MR technicians, radiology nursing, radiologists, and the few cardiologists who interpret adult cardiac MR at our institution. Initial policy was drafted by a faculty member who had completed fellowship less than one year previously at an institution where ferumoxytol was used regularly, with assistance from a trainee and students. Searching the 2021 ACR Manual on Contrast Media for "ferumoxytol" generated zero results. Searching the same document for "iron" did not generate results regarding intravenous iron-based contrast agents. The hospital's affiliated children's hospital ferumoxytol quick reference guide (QRG) was reviewed following correspondence with the pediatric radiologist MR Medical Director. Additional references were identified via a search of the peer-reviewed literature. At the time of this writing, the policy is undergoing multiple iterations. The trainee involved will graduate fellowship shortly after the abstract submission due date and intends to pursue similar policy creation at her first faculty job.

Result: The authors hope that by the time of SMRA 2021 a policy will have been approved. Ferumoxytol has unique relaxivity characteristics with a high r2 of 100 L $mmol^{-1}$ sec^{-1} low r1/r2 ratio, and an intravascular half-life of 14 - 15 hours, nearly 15 times that of gadolinium. This makes ferumoxytol ideal for patients who require serial scans or repeat imaging and endowing it with uniquely flexible properties. In order to ensure safety in use of ferumoxytol, some specific actions are recommended prior to, during, and after its administration. Patient history must be reviewed for any factor that contraindicates ferumoxytol administration, such as iron overload or a history of adverse reactions to intravenous iron products. Informed consent should be obtained from the patient or patient representative, unless this is waived per local institutional policy. In all cases, patients should be informed that about 1 in 200 may experience self-limiting 'Fishbane' reactions to intravenous iron, which most commonly manifests as flushing, chest tightness, back pain or abdominal pain. These symptoms usually resolve spontaneously within minutes of stopping intravenous infusion but can be distressing if patients are not aware of their nature and significance. Fishbane reactions are not accompanied by signs of anaphylaxis, such as wheezing, tachycardia and hypotension. Once symptoms resolve, slow infusion of ferumoxytol can generally be safely resumed without recurrence of symptoms. If patients are not made aware that these symptoms can occur, they may panic and become distressed. True anaphylaxis with ferumoxytol is extremely rare and has not been described with its diagnostic use. Ferumoxytol administration should generally be slow, over a period of about 10 minutes, with recommended blood pressure check at baseline, 5-minutes following the start of infusion and at the end of the study. For outpatients, this could be performed under the supervision of radiology nursing; for inpatients, this may be performed by radiology nursing or by inpatient nursing with specific training in assessing symptomatology. Nurses should be physically present and maintain communication with the patient. In the rare event of a severe contrast reaction, local contrast adverse reaction policy should be followed as necessary.

Discussion: It is our hope that sharing our ferumoxytol policy creation experience with SMRA will be of assistance to individuals at other institutions in developing their own ferumoxytol policies as needed or amending existing policies for improved patient safety. We also hope to inspire discussion regarding how to propel our already innovative field into the future while simultaneously increasing patient safety and attracting the brightest young minds to our profession.

References

ACR Committee on Drugs and Contrast Media. ACR Manual on Contrast Media 2021. www.acr.org.
Nguyen K, Yoshida T, Kathuria-Prakash N, *et al*. Multicenter safety and practice for off-label diagnostic use of ferumoxytol in MRI. Radiology 2019;293:554-64.
Rampton D, Folkerson J, Fishbane S *et al*. Hypersensitivity reactions to intravenous iron: guidance for risk minimization and management. Haematologica 2014;99:1671-6.
Starekova J, Nagle SK, Schiebler ML, Reeder SB, Meduri VN. Abstract 0186: Ferumoxytol-enhanced pulmonary MRA in pregnancy: Evaluation of initial safety and image quality. ISMRM 2021.
Vasanawala SS, Nguyen K, Hope MD, *et al*. Safety and technique of ferumoxytol administration for MRI. Magn Reson Med 2016;75:2107-2111.

Abstract ID: 63

Prototype Platform for Real-time MR-guided Brain Clot Evacuation

Robert Moskwa[1],Eugene Ozhinsky[2],Azam Ahmed[3],Walter Block[1]

[1]Medical Physics, University of Wisconsin-Madison, [2]Department of Radiology and Biomedical Imaging, University of California San Francisco, [3]Neurological Surgery, University of Wisconsin-Madison

Purpose: The international Phase III MISTIE Trial, which used CT-image guidance to position a catheter at the site of intracerebral hemorrhage (ICH) for periodic clot drainage and infusion of thrombolytic drugs, showed a subset of patients whose interventions left less than 15 ml of residual clot volume had statistically significant reductions in morbidity and increased independence[1]. The Trial concluded that improved guidance was needed to help a wider set of neurosurgeons meet the 15 ml residual volume goal without endangering rebleeds. MR-guidance of ICH evacuation could help meet these needs. We present here an MR-guidance prototype that is designed to allow neurosurgeons to periodically assess and alter the clot evacuation by manipulating catheter position and spatially visualizing the delivery and distribution of clot-busting drugs with respect to normal brain tissue.

Methods: We used the HeartVista RTHawk interventional platform[2], as it allows us to design the interventional guidance without knowing specific software constructs or data pathways on the commercial scanner. Interfaces were created with the purpose of providing neurosurgeons easy and intuitive access to MRI viewpoints that are already commonly used in a stereotactic operating room setting. For this work, these viewpoints included standard axial, sagittal, and coronal views, as well as two views in the plane of an invasive deice, and one perpendicular to the device, termed 'probe's eye view'. Interface based on a similar project in ablation monitoring pioneered by Ozhinsky[3]

Results: Due to time constraints and difficulties related to COVID-19 MR, the prototype results are all from a simulated phantom. A prototype 6-panel interface is presented in figures 1 and 2. A real-time spiral GRE sequence is used. Each of the 6 panels are fully adjustable by the user, and can be individually manipulated without affecting other panels. This includes selecting any through-plane to visualize, rotating the image, and selecting parameters in real-time such as TR, TE, and FOV. The TE can easily be extended to provide T2* imaging that highlights clot. All parameter changes and image acquisitions would be performed in real time and displayed accordingly.

Discussion: The flexibility provided by the RTHawk interface allow for rapid prototyping and feedback from our neurosurgery collaborators. After integration, we plan to first test the real-time visualization system in ex-vivo models of swine blood and then move to a swine model of ICH using injected blood to simulate an ICH. The MR-guidance prototype created using RTHawk shows potential to be a flexible and reliable tool to assist as a monitoring and guiding tools and lysing drugs during clot-evacuation procedures, potentially for more extensive clot evacuation while minimizing chances of rebleeds.

References:

[1] Hanley DF, Thompson RE, et al. Lancet. 2019. doi: 10.1016/S0140-6736(19)30195-3. PubMed PMID: 30739747.

[2] Santos JM, Wright GA, Pauly JM. Conf Proc IEEE Eng Med Biol Soc. 2004;2:1048-51. PubMed PMID: 17271862.

[3] Ozhinsky E, Salgaonkar VA, Diederich CJ, Rieke V. J Ther Ultrasound. 2018 Aug 13;6:7.

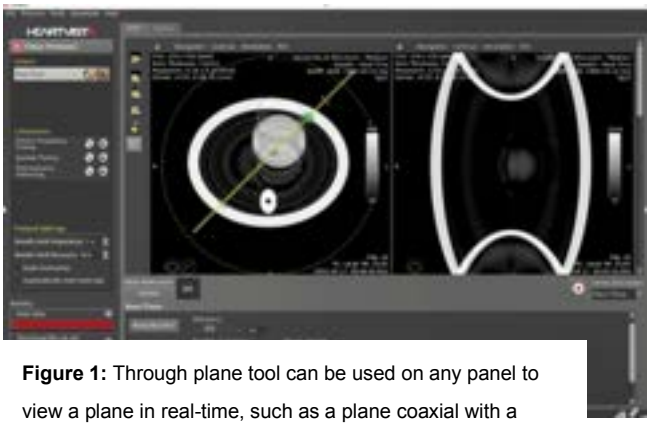

Figure 1: Through plane tool can be used on any panel to view a plane in real-time, such as a plane coaxial with a catheter.

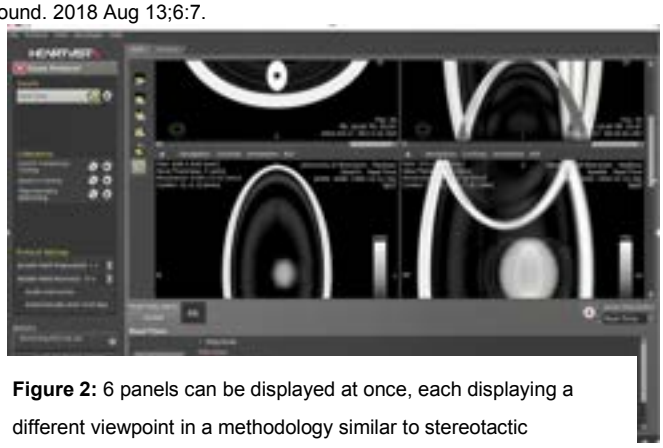

Figure 2: 6 panels can be displayed at once, each displaying a different viewpoint in a methodology similar to stereotactic neurosurgical worksatations. Views and parameters can be adjusted.

Abstract ID: 64

Abdominal 4D Flow MRI in Obese Patients – A Pilot Study

Alma Spahic[1], Thekla H. Oechtering[2], Grant S. Roberts[1], Alejandro Roldán-Alzate[2,3,4], Scott B. Reeder[1, 2, 4], Oliver Wieben[1 ,2] , Kevin M. Johnson[1, 2]
Departments of [1]Medical Physics, [2]Radiology, [3]Mechanical Engineering, [4]Biomedical Engineering, University of Wisconsin-Madison, Madison, WI, United States

Purpose: The image quality in abdominal and chest 4D Flow MRI deteriorates in obese patients due to the high confounding signal from fat, larger required imaging volume, and chemical shift artifacts from fat [1]. These artifacts are exacerbated when using accelerated imaging such as non-Cartesian trajectories and can also compromise background phase corrections [2]. In this pilot study, we investigate the utilization of fat suppression and advanced reconstruction approaches in hepatic 4D Flow MRI to improve image quality and flow consistency in severely obese (BMI>40) patients.

Methods:

Image Acquisition: In this IRB-approved study, 4D Flow data were acquired after fasting using a 5-point encoded radially undersampled trajectory (PC-VIPR [3], full volumetric coverage of the upper abdomen: imaging volume=32x32x24cm; resolution=1.25mm isotropic; flip=6˚; scan time=11 min; TR/TE=6.5ms/2.4ms; no contrast; with retrospective ECG and respiratory gating. Data were acquired with and without fat saturation pulses, which were played out every 15 TRs. Two offline cine reconstructions (20 time frames) were performed on the acquired data: (1) gridding with temporal view sharing [4] and PILS [5] and (2) conjugate gradient iterative SENSE (Fig. 2). First scan was acquired without fat suppression (height=1.66±0.01 m, weight=131.5±0.5 kg, BMI=47.7), followed by a fat suppressed scan 150 days later (height=1.65±0.01 m, weight=111.4±0.5 kg, BMI=40.9).

Fig 1: Planes evaluated in 4D Flow analysis. *Blue-bifurcation, orange-confluence*

Data analysis: Standard corrections for Maxwell terms and gradient non-linearity were included in the reconstruction. Third-order polynomial background phase correction [6] was conducted using a custom MATLAB (Mathworks, Natick, MA) tool. Following phase correction, 4D Flow streamline visualizations and measurements were obtained using EnSight software (ANSYS, Canonsburg, PA). Volumetric flow rates were measured in the portal venous system with 6 cross sections of interest: right portal vein (RPV), left portal vein (LPV), cranial portal vein (PV2), caudal portal vein (PV1), superior mesenteric vein (SMV), and splenic vein (SV) (Fig.1). Measurements of the net flow (ml/s) in these 6 regions were used to evaluate mass conservation at confluence and bifurcation.

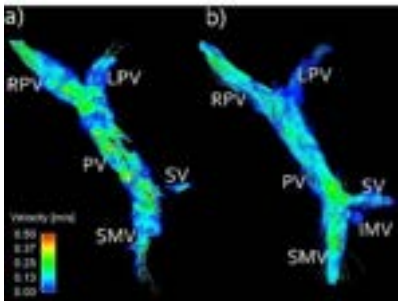

Fig 3: 4D Flow streamlines of the portal venous system from acquisitions a) without fat suppression, b) with fat suppression. *Right portal vein (RPV), left portal vein (LPV), main portal vein (PV), superior mesenteric vein (SMV), inferior mesenteric vein (IMV) and splenic vein (SV).*

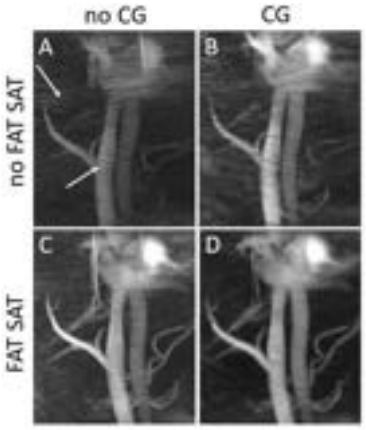

Fig 2: Representative image reconstruction results (maximum intensity projection images) for subject 1 at visit 1 without fat sat. (A,B) and visit 2 with fat sat. (C,D). (A). Applying the conjugate gradient ('CG – panel B) or fat suppression (C) reconstruction reduces the artefacts and simultaneous use of CG and fat suppression provides the visually best artefact suppression (D). Slight blurring is noticeable when using CG reconstruction.

Results and Discussion:

Abdominal 4D Flow scans in a severely obese patient showed strong streak artefacts from signal outside the imaging volume (arms) and subcutaneous abdominal fat and errors from imperfect background phase corrections (Fig 2). Image quality was significantly improved when combining fat suppression and conjugate gradient reconstruction. Fig. 3 shows a streamline visualization of the portal venous system with increased homogeneity, more likely to reflect the actual flow field. The consistency of flow measures also improved with fat suppression. Confluence percent errors in mass conservation reduced from 19.98% (without fat suppression) to 8.47% (with fat suppression). Similarly, bifurcation mass conservation error reduced from 14.8% (without fat suppression) to 5.20% (with fat suppression).

In summary, combined fat suppression and CG reconstruction in the abdominal MR vascular scans of a severely obese patient (BMI>40) significantly improved image quality and consistency of vascular flow measurements in the portal venous system. While additional subjects are needed in controlled studies, these results suggest benefits of fat saturation observed in other applications may extend to 4D Flow acquisitions.

The authors wish to acknowledge the NIH (R01 DK088925) and Pfizer Healthcare for supporting this study, as well as GE Healthcare who provides research support to the University of Wisconsin.

References:[1] Middione, M.J., Ennis, D.B. MRM. 2013; 69, 391-401 [2] Johnson, K. M. et al. MRM. 2010; 63, 1564-1574. [3] Johnson, K. M. et al. MRM. 2008; 60(6), 1329-1336. [4] Liu J et al. IEEE TMI. 2006; 25(2):148-57 [5] Griswold MA et al. MRM. 2000; 44(4), 602-9 [6] Walker, P.G., et al. JMI. 1993; 3, 521-530.

Abstract ID: 65

Neurovascular 4D-Flow using Motion Correction and Deep Learning Denoising

Kevin M. Johnson[1,2], Leonardo Rivera-Rivera[1,3], Steve Kecskemeti[1], Mu-Lan Jen[1], Zach Miller[1], Laura B. Eisenmenger[2]
University of Wisconsin – Madison, WI, USA, Departments of [1]Medical Physics, [2]Radiology, and [3]Medicine

Purpose: Neurovascular 4D-Flow has emerged as a powerful tool to understand vascular contributions to dementia, image flow within aneurysms and arterial venous malformations, and quantify flow features related to atherosclerosis. Further, emerging paradigms are being developed to provide unique measures of low frequency flow oscillations (LFOs), pulse wave velocity measures of arterial stiffness, and flow turbulence and disorder. However, these new 4D-Flow applications and the need to characterize flow in small vessels require high spatial and temporal resolution, leading to long scan times and hence higher sensitivity to motion and noise. In this work, we develop a neurovascular 4D-Flow imaging paradigm which provides motion correction capabilities and acceleration using deep learning denoising. Initial results are demonstrated in retrospectively re-analysis of previously acquired data.

Methods: The proposed methodology (Figure 1) combines 3D radial sampling, 3D self-navigation[1], and deep learning denoising using noise-to-noise learning. Data is collected with 3D radial sampling using pseudorandom ordering such that the data can be binned temporally and with respect to the cardiac cycle. Images are first reconstructed temporally using the Extreme MRI[2] framework, providing 3D images with a ~1s frame rate. These images are rigidly registered to provide estimates of translation and rotation at each time point, which are utilized in a motion corrected iterative image reconstruction. This provides motion corrected but still noisy 4D-Flow data. To reduce the variance from noise and residual under sampling artifacts, the data is further refined using a post-reconstruction deep learning based denoiser. ***Initial Testing:*** All methods were implemented in GPU accelerated python (SigPy and PyTorch). The deep learning denoiser was trained using a noise-to-noise training approach[3] in which time averaged 4D-Flow datasets were randomly split in k-space by subsampling the projections and reconstructing a highly sampled image (7/8^{ths} of the data) and a low sampled image (1/8th of the data). A block-wise 3D UNet was used to estimate the highly sampled complex images from the low sampled images. Training data was from 120 quality controlled neurovascular 4D-Flow scans acquired with a similar protocol (0.7mm isotropic resolution, whole brain coverage, TE/TR=2.7/7.8ms, 426s scan time, V_{enc}=80cm/s). A training/validation/test split of 100/10/10 was used with standard geometric augmentations performed, with care to avoid rotations that would alter dipole kernel symmetries.

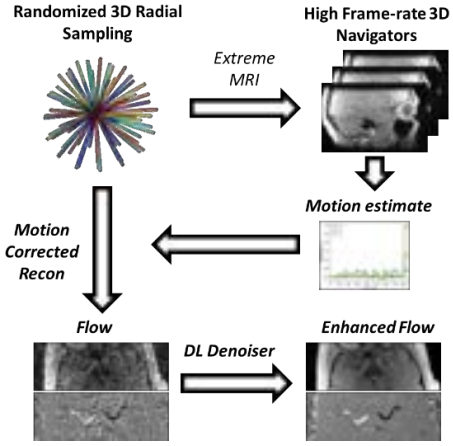

***Figure 1**. Framework for motion corrected and deep learning enhanced 4D-Flow.*

Results and Discussion: Figure 2 shows initial results using this framework in a patient with apparent motion artifact. Motion estimates demonstrate motion on multiple scales including large bulk motion as well as smaller motions. The incorporation of motion correction into the framework substantially improves image quality in subjects where motion is present. Deep learning enhancement visually improves image quality and also resulted in an improvement in correlation between velocities measured with high and low fractions of the data. The proposed framework represents a promising method to reduce variance from motion, noise, and undersampling in 4D-Flow MRI. Ongoing work is needed to validate and quantify these improvements, and evaluate their potential to enable imaging in challenging populations (e.g. children).

References: [1] Kecskemeti et al. doi:10.1148/radiol.2018180180 [2] Ong et al. doi:10.1002/mrm.28235 [3] Lehtinenn et al. arxiv:1803.04189

Acknowledgement: Research support from GE Healthcare, NIH R01NS066982/P30AG062715, AARFD-20-678095

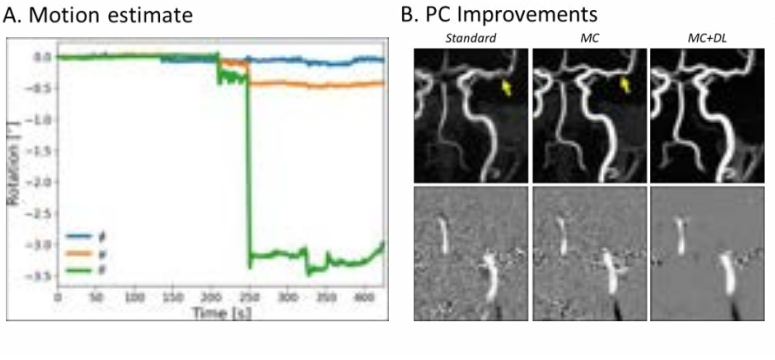

***Figure 2**. Initial results showing (A) motion estimates, (B) improved image quality in angiograms and flow fields using motion correction (MC) and deep learning (DL), and (C) reduced variance and higher correlation between the data using deep learning enhancement (bottom) in the 10 test datasets.*